UNIVERSIDAD PABLO DE OLAVIDE
DEPARTAMENTO DE SISTEMAS FÍSICOS, QUÍMICOS Y NATURALES.

ESTUDIO MESOSCÓPICO DE LA ADSORCIÓN DE FLUIDOS SIMPLES SOBRE SUSTRATOS MICROESTRUCTURADOS

Memoria que presenta

Álvaro Rodríguez Rivas
para optar al grado de Doctor

Director de la Tesis:	Tutor de la Tesis:
Dr. José Manuel Romero Enrique Profesor Titular de Universidad Departamento de Física Atómica, Molecular y Nuclear Universidad de Sevilla	**Dr. Juan Antonio Anta Montalvo** Profesor Titular de Universidad Departamento de Sistemas Físicos, Químicos y Naturales Universidad Pablo de Olavide

Sevilla, Noviembre 2015

A Inma, a mis hijos y a mis padres

Agradecimientos

Durante todo estos años de aprendizaje, investigación y de desarrollo de esta Tesis doctoral, he tenido la gran oportunidad de conocer a muchas magníficas personas y sobre todo amigos. La extensión total de páginas de esta Tesis me resulta escasa para expresar a cada una de ellas mi gratitud por compartir un poco de su tiempo conmigo (en mayor o menor medida). No sólo son unas personas excelentes en lo que a su trabajo se refiere, sino que sobre todo en lo personal. Me han mostrando lo mejor de ellos mismos.

Quisiera expresar mi gratitud a cada uno de vosotros, y en primer lugar quiero expresar mi más sincero agradecimiento José Manuel Romero Enrique, por guiarme todo estos años de aprendizaje, por su paciencia, por sus consejos, su rigor en la investigación y por enseñarme lo mejor de la Física. Lo considero un amigo al que le estaré siempre agradecido. Sin su ayuda nunca hubiera realizado esta Tesis.

También quisiera expresar mi gratitud a prof. Luis F. Rull por darme la oportunidad de entrar y por acogerme en su grupo de Física Estadística de Líquidos, por guiarme y aconsejarme como lo hubiera hecho un padre, así como presentarme y conocer a maravillosas personas de la comunidad científica, tanto a nivel científico como personal.

A mis dos compañeros de grupo Óscar Alan Rojas y José Antonio Galván que me han acompañado en los largos viajes por España a congresos y cursos (aguantando la música que les ponía), así como en las largas horas de trabajo diario en nuestro despacho de la quinta planta de la Facultad de Física de La Universidad de Sevilla.

Después de asistir a 3 congresos internacionales, otros tantos nacionales, así como estancias breves en centros de investigación, cuatro *workshop*, 4 escuelas y cursos, reuniones de trabajo, y una infinidad de seminarios, he podido conocer y volver a ver a amigos y conocidos, pero también, echar de menos a la familia, y valorar mucho los momentos en los que estamos juntos. Por eso, quisiera recordaros y daros las gracias a todos vosotros, independientemente de donde estéis, y comenzando por los profesores y compañeros del departamento de Física Atómica, Molecular y Nuclear (área de Física

Teórica) Javier Brey, María Jose Ruiz, Naghi Khalil, Alvaro Domínguez, Pablo Maynar, Maribel García de Soria, Antonio Prados, Antonio Lasanta y Vicente Buzón, a los que he podido conocer poco a poco durante todos estos años. Y también a Adrián Ayala por esas largas charlas sobre Física.

Quisiera dar las gracias a los compañeros y profesores de la Universidad Pable de Olavide, Juan Antonio Anta, tutor de esta Tesis, a Alejando Cuetos al que quiero dar las gracias por sus consejos y que me ha encantado conocer durante las veces que hemos coincidido, a Sofía Calero que fue miembro del tribunal de mi diploma DEA junto con Juan Antonio, a Bruno, por compartir el cluster, así como a los compañeros Jesús Idígoras, Ana Martín, a Paula Gómez, Julio Pérez y Rocío Bueno.

De mis estancias en otros centros de investigación y escuelas quiero primero agradecer a Ed Tucker, un buen amigo y gran jugador de fútbol, y a los demás compañeros del Imperial College por su acogida en el tiempo que estuve allí. Pero sobre todo al Prof. Andrew O. Parry, una persona excepcional, que hizo todo lo posible por que durante mi estancia me sintiera como en casa, gracias. Al que considero un amigo y que da una charlas increíbles. También a los profesores George Jackson, Eric Müller, y Fernando Bresme, a los que he conocido en mi estancia y visitas.

En la Johannes Gutenberg-Universität de Mainz, a los compañeros de despacho, unas magníficas personas, Benjamin Trefz, Antonia Statt, y Debabrata Deb, sin olvidar a los demás compañeros Gang Huang, Santosh Kumar Meena, así como a los profesores Peter Virnau, Marialore Sulpizi, Friederike Schmid y Giovanni Settanni. Gracias a Ezequiel Albano por ayudarme a verificar el cálculo de errores, por las agradables charlas en los almuerzos y por ser una magnífica persona. También estoy muy agradecido a Andrey Milchev y Kurt Binder quienes me aconsejaron, escucharon y ayudaron muy amablemente en los avances con el modelo de Ising que hemos estudiado, y que siendo unas personas muy ocupadas así como eminencias mundiales en sus campos de investigación.

En la Universidad Carlos III de Madrid a las compañeras del despacho de profesores visitantes, Yamilet Quintana y Nikta Shayanfar, a quienes les deseo todo lo mejor. También a los profesores Rodolfo Cuerno, Yuri Martínez Ratón, Jose A. Cuesta y Esteban Moro por su acogida en el departamento e interesantes seminarios. Pero sobre todo al prof. Carlos Rascón, del que sólo puedo expresarle gratitud por toda la ayuda que me prestó en el modelo de doble parábola, por toda la Física y Matemática que aprendí allí, y ser un amigo.

En la Universidad de Lisboa, agradecerle a Margarida Telo Da Gama, Pedro Patrício, José María tavares, Nelson Bernardino, Nuno M. Silvestre, Daniel de las Heras, y a Paulo I.C. Teixeira, por ser unas personas fantásticas sobre todo en lo personal.

A los profesores de la Escuela de Simulación de la Rábida, a Felipe Jiménez Blas, a Noe G. Almarza, Eva G. Noya, Enrique Lomba, , Manuel Martínez Piñeiro y Carlos Vega, por todo lo que he aprendido de vosotros y no sólo en simulación por ordenador, y a los compañeros del curso.

A los compañeros del Departamento de Matemática Aplicada II en la Politécnica de la Universidad de Sevilla, Nieves, Mónica, Inmaculada, Francisco Rodrigo, Paco Torres, Julio, Elisabeth, Javier Ros e Inés, y en especial a Mirta Castro, Ana Beatriz Ramos y José Manuel Gallardo, por ayudarme y hacerme partícipe de vuestra vida diaria.

También agradecer a Bob Evans el conocerle, así como por sus divertidas y amenas charlas, tan llenas de una profunda e interesante física de líquidos, y con quien coincidí en bastantes lugares de Europa.

Quiero expresar un agradecimiento especial a mis amigos Armando Fernández Prieto, Isidro Lorenzo Geada, Emilio González Galindo, y Alessio Squarcini a quienes he conocido estos años en diferentes circunstancias a lo largo de la carrera o después, y con los que he pasado muy buenos momentos y que espero sean muchos más.

Quiero darle las gracias a mis padres Fernando y M^a del Carmen por quererme y preocuparse por mis niños, por mi mujer y por mí, por poner todo de su parte a lo largo de mi vida hasta llegar a este momento. Gracias, os quiero muchísimo.

A mi familia de Osuna, Constantina y Sevilla, y en especial a mis hermanos Fernando y Miguel Ángel, por estar ahí siempre.

Por último, pero que en mis pensamientos está en primer lugar, quiero darle las gracias a mi mujer Inma, primero por ser la madre de mis dos preciosos hijos Álvaro y Luis, vosotros tres sois mis alegrías diarias. Por aguantar las largas estancias que estuve fuera de casa y viajes, durante todos estos años. Por quererme tanto, esperarme tanto, y tener conmigo esta familia. Te quiero.

Resumen

En esta Memoria se han estudiado modelos mesoscópicos de adsorción en fluidos simples sobre sustratos microestructurados, tanto analíticamente, numéricamente y mediante simulación por ordenador. Hemos considerado dos tipos prototípicos de sustratos microestructurados: la hendidura en cuña y el sustrato sinusoidal. El primer caso se ha estudiado por simulación por ordenador para el modelo de Ising, centrándonos en las transiciones de rellenado crítica y tricrítica. Estos resultados se han analizado usando resultados analíticos de un modelo fenomenológico que tiene en cuenta las fluctuaciones interfaciales del tipo modo de respiración. Hemos usado como parámetro de control una interacción modificada espín-sustrato en una región alrededor del fondo de la hendidura, que favorece la adhesión de la interfase a dicha región. Si esta interacción no es lo suficientemente intensa para inducir dicha adhesión, hemos visto que nuestros resultados de simulación tienen un buen acuerdo con las predicciones teóricas del modelo fenomenológico para la transición crítica. Si se aumenta su intensidad, se observa un cambio en el comportamiento interfacial consistente con una transición de rellenado de primer orden. Ajustando el valor de la interacción, se observa un cierto valor que es consistente con la predicción de la teoría fenomenológica para la transición tricrítica.

Para el sustrato sinusoidal, hemos obtenido el diagrama de fases de adsorción en la aproximación de campo medio tanto en condiciones de coexistencia en volumen como fuera de ella, centrándonos en la transición de rellenado y mojado. Para ello hemos usado distintos modelos microscópicos de grano grueso: el modelo de Landau-Ginzburg y el modelo de doble parábola. En el primer caso, hemos obtenido el diagrama de fases usando técnicas de elementos finitos cuando el sustrato presenta una transición de mojado de primer orden o una transición de mojado crítica. Dependiendo del orden de la transición, y para una rugosidad dada, la temperatura de transición de mojado se reduce al disminuir el periodo del sustrato para el caso de mojado de primer orden, mientras que permanece inalterada para el caso de mojado crítico. Por otro lado, cuando la amplitud de la corrugación es del orden de la longitud de correlación del líquido, la transición de rellenado desaparece y sólo se

observa la de mojado. El límite entre ambos escenarios es un punto triple en el caso de primer orden, y un punto crítico de rellenado para mojado crítico. Finalmente, tanto la transición de rellenado como el mojado de primer orden se extienden a las transiciones de rellenado y de premojado fuera de la coexistencia en volumen, que terminan en sendos puntos críticos. El segundo modelo considerado es el modelo de doble parábola, que por un lado puede considerarse como una aproximación al modelo de Landau-Ginzburg, pero por otro puede relacionarse formalmente con modelos de Hamiltoniano interfacial, permitiendo establecer un nexo entre las descripciones microscópica y mesoscópica de los fenómenos interfaciales. Hemos estudiado el diagrama de fases usando el método de los elementos de contorno para el caso de mojado crítico, obteniendo un buen acuerdo con los resultados del modelo de Landau-Ginzburg en términos del ángulo de contacto y la curvatura interfacial.

UNIVERSIDAD PABLO DE OLAVIDE
DEPARTAMENTO DE SISTEMAS FÍSICOS, QUÍMICOS Y NATURALES.

MESOSCOPIC STUDY OF SIMPLE FLUIDS ADSORPTION ON MICROSTRUCTURED SUBSTRATES

Author

Álvaro Rodríguez Rivas

A thesis submitted in fulfiment of the requirements for the degree of Doctor of Philosophy in the Universidad Pablo de Olavide

Supervisor:	Internal supervisor:
Dr. José Manuel Romero Enrique Profesor Titular de Universidad Departamento de Física Atómica, Molecular y Nuclear Universidad de Sevilla	**Dr. Juan Antonio Anta Montalvo** Profesor Titular de Universidad Departamento de Sistemas Físicos, Químicos y Naturales Universidad Pablo de Olavide

Seville, November 2015

Preface

The work in this Thesis was conducted in the Statistical Physics of Liquids group in the Departamento de Física Atómica, Molecular y Nuclear of the Universidad de Sevilla. It is part of two funded Projects in this group, namely "Teoría y simulación de modelos mesoscópicos de adsorción de fluidos simples y complejos sobre sustratos microestructurados" (FIS2009-09326, funded by Spanish Ministerio de Ciencia e Innovación, 2009-2013) and "Transiciones de Fase y Fluctuaciones en la Adsorción de Fluidos Simples y Complejos sobre Sustratos Microestructurados" (FIS2012-32455, funded by Spanish Ministerio de Economía y Competitividad, 2013-2015). Moreover, my research was funded by the FPI scholarship BES-2010-029922 (2010-2014) funded by the Ministerio de Ciencia e Innovación/Economía y Competitividad.

The work presented in the Thesis was partially published in the following peer-review articles:

1. J. M. Romero-Enrique, A. Rodríguez-Rivas, L. F. Rull and A. O. Parry, *A finite-size scaling study of wedge filling transitions in the 3D Ising model*, Soft Matter **9**, 7069-7075 (2013) (Chapter 2).

2. A. Rodríguez-Rivas, J. M. Romero-Enrique, L. F. Rull and A. Milchev, *Observation of a tricritical wedge filling transition in the 3D Ising model*, EPL **108**, 26003 (2014) (Chapter 2).

3. A. Rodríguez-Rivas, J. Galván and J. M. Romero-Enrique, *Filling and wetting transitions on sinusoidal substrates: a mean-field study of the Landau-Ginzburg model*, Journal of Physics: Condensed Matter **27**, 035101 (2015) (Chapter 3)

Contents

1 Introduction 3

2 Critical and tricritical wedge filling transitions 11

2.1 Introduction . . . 11
2.2 Phenomenological theory of filling on a double wedge . . . 21
2.3 Double wedge Ising model simulations . . . 32
2.4 Summary . . . 40

3 Filling and wetting transitions on sinusoidal substrates: a mean-field study of the Landau-Ginzburg model 43

3.1 Introduction . . . 43
3.2 Macroscopic theory . . . 45
3.3 Methodology . . . 53
3.4 Numerical results . . . 55
  3.4.1 Results for $c = 0$, $h = 0$ . . . 56
  3.4.2 Results for $c = +\infty$, $h = 0$ . . . 62
  3.4.3 Results for $c = 0$, $h < 0$ . . . 70
  3.4.4 Results for $c = \infty$, $h < 0$ . . . 77
3.5 Open questions . . . 79

4 Filling and wetting transitions on sinusoidal substrates: a mean-field study of the double parabola model 83

4.1 Introduction . . . 83
4.2 Theoretical background . . . 84
4.3 Methodology . . . 91
4.4 Numerical results . . . 95
  4.4.1 Results for $h = 0$ . . . 96
  4.4.2 Results for $h < 0$ . . . 101
  4.4.3 Summary . . . 102

5 Conclusions 107

A The Landau-Ginzburg theory of wetting of flat substrates 111

B The Conjugate Gradient Method. 121

List of Figures

1.1 (a) Optical micrograph of the central area of the chemical reactor circuit used in the production of 2-deoxy-2-fluoro-D-glucose (FDG) (from Ref. [67]). (b) An integrated microfluidic chip for genomics that analyses short tandem repeats (from Ref. [145]) 4

1.2 (a) Sandia Digital Microfluidic Hub, a droplet-handling router (picture taken of Sandia National Labs). (b) Microfluidic chip houses bioreactors, where bacteria can be cultured and observed (picture taken of Frederick Balagadde (Stanford Researchers)) 5

1.3 (a) Picture of a drop on a lotus leaf (picture taken of Wikimedia Commons). (b) Laser micro and nano-structuring (picture taken of Fraunhofer Institute for laser Technology). (c) Schematic illustration of a droplet on a superhydrophobic stripes (from Ref. [34]) 5

1.4 (a) Schematic illustration of the wetting transition (picture taken from the Low Temperature Physics group website in Konstanz Universität). (b) Schematic illustration of the Cassie-Baxter and Wenzel models (picture taken of Carl Clegg, Rame-hart Instrument Co.). 6

1.5 Micro and nanostructured surfaces of wedges and sawtooth patterns: (a) Surface patterned by photolithography (from Ref. [28]), (b) Cross section and top view of a silicon patterned surface (from Ref. [17]), (c) Sawtooth microfeatures on a belt mold electroformed nickel alloy sheets (from Ref. [44]) 7

1.6 Sinusoidal micro and nano-structured surfaces: (a) and (b) 1740 lines/mm ion milled fused silica substrate (picture taken of James Oliver -MSC- 2004). (c) Manufactured sinusoidal RP resin formers and the resulting electrospun PLGA scaffolds (from Ref. [124]) 9

2.1 Schematic illustration of a typical interfacial configuration in the wedge geometry showing the relevant diverging length scales at the filling transition (from Ref. [97]) 12

2.2 Schematic illustration of a typical interfacial configuration for fluid adsorption in a 3D double wedge. 22

2.3 Schematic illustration of the regularization procedure. We introduce a square well-like contact potential (a) with constant strength $-U$ with a width ξ_0. On the other hand, the effective potential $\tilde{V}_W(\ell) = -3\tan\alpha/(16\Sigma\ell^3)$ vanishes for $\ell < \xi_0$ (b). Finally, the position-dependent stiffness is modified to be a constant for $\ell < \xi_0$ (c). 26

2.4 Graphical solution of the Eq. (2.60) for the critical (a) and tricritical (b) cases. The continuous line corresponds to the function $\mathrm{Ai}'(x)/\mathrm{Bi}'(x)+C$, and the dashed line one to $\mathrm{Ai}(x)/\mathrm{Bi}(x)+C$. The values of x_i are the zeroes of these functions. 29

2.5 Magnetization PDFs at the critical (a) and tricritical (b) filling transition obtained from the phenomenological theory. The parameters considered are $\alpha = \pi/4$, $\Sigma = 0.0981$ and $m_b = 0.75$ to mimic the existing Ising model studies [80, 81]. The continuous curve corresponds to $L_y/L^3 = 0.0046$, and the dashed line to $L_y/L^3 \to \infty$. 31

2.6 Schematic picture of the modified antisymmetric double wedge geometry of size $L\times L\times L_y$ and characterized by a tilt angle α. Filled and empty symbols refer to the spins associated with the surfaces which define the W_1 (filled) and W_2 (empty) wedges. Circles represent the sites subject to the surface fields H_s (W_1') and $-H_s$ (W_2'). Squares represent the wedge sites where act the line field h_l ($W_1 - W_1'$) and $-h_l$ ($W_2 - W_2'$). 34

2.7 Plot of the magnetization PDFs for $h_l = H_S$ and: $H_s = 0.7345$, $19\times19\times16$ (squares); $H_s = 0.7284$, $24\times24\times37$ (circles); $H_s = 0.7230$, $34\times34\times124$ (diamonds); and $H_s = 0.7211$, $44\times44\times294$ (triangles). Under these conditions an optimal match with the theoretical prediction (wide line) is obtained. The magnetization PDF was scaled by factors 1.05, 1.02, 1.01 and 1.00, respectively. 36

2.8 Magnetization PDFs for $L = 24$, $L_y = 37$ and different values of (H_s, h_l): (a) $(0.7084, 0.7284)$, (b) $(0.7284, 0.7284)$, (c) $(0.7484, 0.7284)$, (d) $(0.7084, 0)$, (e) $(0.7284, 0)$, (f) $(0.7484, 0)$, (g) $(0.7084, -0.5)$, (h) $(0.7284, -0.5)$, and (i) $(0.7484, -0.5)$. . 37

2.9 Plot of the magnetization PDFs for $h_l = 0$ and: $H_s = 0.7345$, $19 \times 19 \times 16$ (squares); $H_s = 0.7284$, $24 \times 24 \times 37$ (circles); $H_s = 0.7230$, $34 \times 34 \times 124$ (diamonds); and $H_s = 0.7211$, $44 \times 44 \times 294$ (triangles). The continuous line corresponds to the breather-mode model predicted tricritical filling PDF, and the dashed line to the predicted critical filling PDF. 38

2.10 Plot of the magnetization PDFs for a double wedge $24 \times 24 \times 37$ at critical situation H_{SC}, weakening the exchange coupling between first neighbours at the bottom and top of the double wedge, at values $j_l/K_bT = 0.0$ (squares), $j_l/K_bT = 0.5$ (circles), and $j_l/K_bT = -2.0$ (diamonds), without factor scaling. Weaker values of j_l lead to a non-ergodic behaviour. 39

3.1 Schematic representation of interfacial states. For bulk coexistence, (i) represents the dry (D) state, (ii) represents the partially filled (F) state and (iii) corresponds to the completely wet state. In (iv) we represent the typical interfacial profile of the partially filled state out of bulk coexistence. The substrate is labelled by w, l stands for the liquid and v for the vapor. . . 45

3.2 Behaviour of $\mathcal{F}^F(x)$ as a function of qx for $qA = 1$ and contact angles: $\theta = \theta^*$ (dotted line), $\theta_f < \theta < \theta^*$ (dashed line), $\theta = \theta_f$ (solid line), $\theta < \theta_f$ (dot-dashed line), and $\theta = 0$ (double dot-dashed line). 50

3.3 Top panel: plot of the cosine of the contact angle at the filling transition θ^F for $h = 0$ as a function of A/L. The dashed line corresponds to the asymptotic expression (3.25). Inset, representation of $qA \cos \theta^F$ as a function of A/L, being the dashed line the limiting value from the asympotic analysis for rough substrates. Bottom panel: plot of qx_c^F as a function of A/L. The dashed line is the limiting value from the asympotic analysis. Inset: plot of the midpoint interfacial height above the substrate of the F state at the filling transition, l^F, in units of the substrate amplitude A, as a function of A/L. The dashed line corresponds to the asymptotic value for $A/L \to \infty$. 51

3.4 Example of linear node shape functions on a 2D domain . . . 53

3.5 Finite-size geometry considered in our numerical study of the sinusoidal substrate. See text for explanation. 55

3.6 Plot of the free energy densities of the different branches of interfacial states for $c = 0$ at $h = 0$, as a function of the surface field h_1, for a sinusoidal substrate with $A/L = 0.5, 1, 1.5$ and 2, and $L = 10$ (crosses), $L = 50$ (open squares) and $L = 100$ (filled circles). The D states branch corresponds to the green (lighter grey) symbols, the W states branch to the blue (dark grey) symbols and the F states branch to the red (light grey) symbols. For comparison, the theoretical prediction from (3.32), (3.33) and (3.34) are also represented as continuous lines (the colour code is the same as for the numerical results). 58

3.7 Magnetization profiles corresponding to the coexistence states at the filling transition (a and b) and the wetting transition (c and d) for $c = 0$, $h = 0$, $A/L = 0.5$ and $L = 20$. 59

3.8 Plot of the wetting transition shift $h_1^{w,\pi} - h_1$ with respect to the flat substrate as a function of the curvature of the substrate at its top $\zeta = 2\pi\sqrt{A/L}$ for $L = 10 - 100$ and $A/L = 0.5$ (circles), $A/L = 1$ (squares), $A/L = 1.5$ (diamonds) and $A/L = 2$ (crosses). The dashed line indicates a linear dependence of the wetting transition shift with ζ. 60

3.9 Adsorption phase diagram on a sinusoidal substrate with $c = 0$ and $h = 0$. The phase boundaries between D, F and W states are plotted for $A/L = 0.5$ (black circles), $A/L = 1$ (red squares), $A/L = 1.5$ (blue diamonds) and $A/L = 2$ (green crosses). Lines serve only as guides for the eyes. The dashed line shows the wetting transition value from Wenzel law prediction (3.13) for $A/L = 0.5$. 61

3.10 Plot of the free energy densities of the different branches of interfacial states for $c = \infty$ at $h = 0$, as a function of the surface magnetization m_s, for a sinusoidal substrate with $A/L = 0.5, 1, 1.5$ and 2, and $L = 10$ (crosses), $L = 50$ (open squares) and $L = 100$ (filled circles). The D states branch corresponds to the green (lighter grey) symbols, the W states branch to the blue (dark grey) symbols and the F states branch to the red (light grey) symbols. For comparison, the theoretical prediction from (3.35), (3.36) and (3.37) are also represented as continuous lines (the colour code is the same as for the numerical results). 63

3.11 Adsorption phase diagram on a sinusoidal substrate with $c = \infty$ and $h = 0$. The phase boundaries between D and F states are plotted for $A/L = 0.5$ (black circles), $A/L = 1$ (red squares), $A/L = 1.5$ (blue diamonds) and $A/L = 2$ (green crosses) (the lines serve only as guides for the eyes). The arrows correspond to the filling transition values of m_s predicted by the macroscopic theory, and the big symbols to the filling transition critical points. Finally the wetting transition is represented by the thick continuous line for $m_s = 1$. Insets: plot of $\Delta\tilde{T} = \sqrt{3}L(1 - m_s)/(2\pi)$ (left) and $(A/L)\Delta\tilde{T}$ (right) as functions of the substrate amplitude A along the filling transition line. The meaning of the symbols is the same as in the main plot. 64

3.12 Magnetization profile along the vertical axis at $x = 0$ corresponding to: (a) the D state and (b) the F state at coexistence in the filling transition for $c = \infty$, $A/L = 0.5$ and $L = 100$. Inset: plot of the complete magnetization order parameter profiles of the coexisting D and F states. 65

3.13 Plot of the filling transition shift $m_s^{macro} - m_s$ as a function of $1/A$, for $A/L = 0.5$ (circles), $A/L = 1$ (squares), $A/L = 1.5$ (diamonds) and $A/L = 2.0$ (crosses). Dashed lines correspond to the linear fits for the transition values for large A and $A/L = 0.5$ and $A/L = 2$. For comparison, a continuous line of slope 1 is also shown. 68

3.14 Plot of the mid-point interfacial height l of the coexisting D and F states at the filling transition for $h = 0$ as a function of L (top) and A (bottom) close to its critical point, for $A/L = 0.5$ (circles), $A/L = 0.75$ (triangles), $A/L = 1$ (squares), $A/L = 1.5$ (diamonds) and $A/L = 2.0$ (crosses). The star in the bottom panel corresponds to the location of the filling critical point predicted for shallow substrates from the interfacial Hamiltonian approach [117], and the dashed and dotted lines in the bottom panel are the mid-point interfacial height of the F state predicted from the macroscopic theory for large A/L at the filling transition and the spinodal line of the F states, respectively. Inset: plot of the deviations of the mid-point interfacial height of the D and F states at the filling transition for $h = 0$ with respect to their average value (the meaning of the symbols is the same as in the main panel). 69

3.15 Magnetization profiles corresponding to the coexistence states at the filling transition (a and b) for $h = -0.025$ and the wetting transition (c and d) for $h = -0.0105$ for $c = 0$, $A/L = 0.5$ and $L = 20$. 71

3.16 Off-coexistence $c = 0$ interfacial phase diagram. The phase boundaries between D and F (filling transition lines) and between F and F^* (prewetting transition lines) are represented by continuous lines/filled symbols for $L = 20$ and dashed lines/open symbols for $L = 50$. Circles correspond to the phase boundaries for $A/L = 0.5$, squares correspond to $A/L = 1.0$, diamonds correspond to $A/L = 1.5$ and triangles correspond to $A/L = 2.0$. The continuous line without symbols represents the prewetting line for the planar wall. Big symbols indicate the position of the critical points. 74

3.17 Plot of the midpoint interfacial height, in units of A, of the D and F states at the filling transition, as a function of $-3hL/2\pi$, corresponding to $c = 0$ and $A/L = 0.5, 1, 1.5$ and 2, for $L = 20$ (squares) and $L = 50$ (circles). The dashed line corresponds to the macroscopic theory prediction for the midpoint interfacial height of the F state. The insets show a zoom of the D and F states midpoint interfacial heights, in units of the correlation length, as a function of $|h|$, close to the filling critical points (the meaning of the symbols is the same as in the main plots). 75

3.18 Plot of the midpoint interfacial height of the F and F^* states at the prewetting transition, as a function of h, corresponding to $c = 0$ and $A/L = 0.5$ (circles), $A/L = 1.0$ (squares), $A/L = 1.5$ (diamonds) and $A/L = 2$ (triangles), and $L = 20$ (full symbols) and $L = 50$ (open symbols). The largest symbols correspond to the locations of the prewetting critical points. . 76

3.19 Plot of the midpoint interfacial height of the coexisting D and F states at filling transition (red squares), F and F^* states at the prewetting transition (green circles) and D and F^* states at the Wenzel prewetting transition (blue triangles) for $L = 5$ and $A/L = 0.5$. The full symbols correspond to the filling and prewetting critical points, and the dashed line indicates the location of the $D - F - F^*$ triple point. Inset: off-coexistence interfacial phase diagram for $L = 5$ and $A/L = 0.5$. The meaning of the symbols is the same as in the main panel. The dashed line indicates the location of the wetting transition at bulk coexistence. 78

3.20 Off-coexistence $c = \infty$ interfacial phase diagram for $L = 20$ (continuous lines/filled symbols) and $L = 50$ (dashed lines/open symbols), corresponding to $A/L = 0.5$ (circles), $A/L = 0.75$ (triangles down), $A/L = 1.0$ (squares), $A/L = 1.5$ (diamonds) and $A/L = 2.0$ (triangles up). The big symbols indicate the position of the critical points. 80

3.21 Plot of the midpoint interfacial height, in units of A, of the D and F states at the filling transition, as a function of $-3hL/2\pi$, corresponding to $c = \infty$ and $A/L = 0.5, 1, 1.5$ and 2, for $L = 20$ (squares) and $L = 50$ (circles). The dashed line corresponds to the macroscopic theory prediction for the midpoint interfacial height of the F state. The insets show a zoom of the D and F states midpoint interfacial heights, in units of the correlation length, as a function of $|h|$, close to the filling critical points (the meaning of the symbols is the same as in the main plots). 81

4.1 The dashed blue line represent the double parabola potential, where m_0 is the bulk magnetization. The Landau-Ginzburg potential is represented by a solid red line to compare. 86

4.2 Schematic illustration of a typical interfacial configuration. Inset: the double-parabola approximation to $\Delta\phi(m)$. 88

4.3 Plot of the free energy densities of the different branches of interfacial states for $c = \infty$ at $h = 0$, as a function of the surface magnetization m_s, for a sinusoidal substrate with $A/L = 0.5$, and $L = 10$ (diamonds), $L = 20$ (open circles) and $L = 50$ (open squares). The D states branch corresponds to the green (lighter grey) symbols, the W states branch to the blue (dark grey) symbols and the F states branch to the red (light grey) symbols. For comparison, the theoretical prediction from (4.49), (4.50) and (4.51) are also represented as dashed lines (the colour code is the same as for the numerical results). 96

4.4 Liquid-vapour interfacial profile for: (a) the D state and (b) the F state at coexistence ($h = 0$) in the filling transition for $c = \infty$, $A/L = 0.5$ and $L = 20$, with $N_\ell = N_\psi = 200$. 97

4.5 Adsorption phase diagram on a sinusoidal substrate with $c = \infty$ and $h = 0$. The phase boundaries between D and F states (DP model) are plotted for $A/L = 0.5$ (green circles), $A/L = 1$ (orange squares), $A/L = 1.5$ (red diamonds), LG model (grey lines and symbols) (the lines serve only as guides for the eyes), and the big symbols to the filling transition critical points. Finally the wetting transition is represented by the thick continuous line for $m_s = 1$. Inset: plot of $\Delta\tilde{T} = \sqrt{3}L(1 - m_s)/(2\pi)$ as a function of the substrate amplitude A along the filling transition line. The meaning of the symbols is the same as in the main plot. The black lines correspond to the predictions from interfacial Hamiltonian theories [114, 117, 118]. 99

4.6 Plot of the filling transition shift $m_s^{macro} - m_s$ as a function of $1/A$, for $A/L = 0.5$ (circles), $A/L = 1$ (squares), $A/L = 1.5$ (diamonds) and LG model curves (grey). The dotted-dashed line correspond a linear fit for the transition values with slope 3. 100

4.7 Plot of the mid-point interfacial height l of the coexisting D and F states at the filling transition for $h = 0$ as a function of L (top) and A (bottom) close to its critical point, for $A/L = 0.5$ (circles), $A/L = 1$ (squares), $A/L = 1.5$ (diamonds) and curves of the LG model (grey). The star in the bottom panel corresponds to the location of the filling critical point predicted for shallow substrates from the interfacial Hamiltonian approach [117], and the dashed and dotted lines in the bottom panel are the mid-point interfacial height of the F state predicted from the macroscopic theory for large A/L at the filling transition and the spinodal line of the F states, respectively. Inset: plot of the deviations of the mid-point interfacial height of the D and F states at the filling transition for $h = 0$ with respect to their average value (the meaning of the symbols is the same as in the main panel). 103

4.8 Liquid-vapour interfacial profiles corresponding to the coexisting D and F states at the filling transition ((a) and (b), respectively) for $h = -0.03$ for $c = 0$, $A/L = 0.5$ and $L = 20$, with $N_\ell = N_\psi = 100$. 104

4.9 Off-coexistence $c = \infty$ interfacial phase diagram for $L = 20$ (dashed lines/filled symbols) and $L = 50$ (continuous lines/open symbols), corresponding to $A/L = 0.5$ (circles), $A/L = 1.0$ (squares), curves of the LG model (grey). The big symbols indicate the position of the critical points. 104

4.10 Plot of the midpoint interfacial height, in units of A, of the D and F states at the filling transition, as a function of $-L/(\pi R)$, corresponding to $c = \infty$, $A/L = 0.5, 1$, for $L = 20$ (squares) and $L = 50$ (circles), and DP model (green) and LG model (red). The dashed line corresponds to the macroscopic theory prediction for the midpoint interfacial height of the F state. The insets show a zoom of the D and F states midpoint interfacial heights, in units of the correlation length, as a function of $|h|$, close to the filling critical points (the meaning of the symbols is the same as in the main plots). 105

A.1 Typical profiles of order parameter theory Landau-Ginzburg for the phenomenon of wetting on a flat substrate. The profiles corresponding to $m(0) = -0.462$ (dashed curve), $m(0) = 0.762$ (curve of dots and dashes) and $m(0) = 2.164$. The latter case corresponds to complete wetting, so the width of the layer of $+1$ phase becomes infinite. 115

A.2 Graphical construction to obtain $m(0)$ for: (a) $c > 1$, (b) $c < 1$. The dashed lines correspond to partial wetting situations, the dot-dashed lines to complete wetting situations, and the continuous lines to the wetting transition. 118

A.3 Plot of the interfacial height z_0 of the coexisting interfacial states along the prewetting line for $c = 0$ as a function of $|h|$. The dot corresponds to the location of the prewetting critical point, and negative values of z_0 means that the magnetization at the wall is negative. Inset: Plot of the prewetting line for $c = 0$ on the $|h| - h_1$ plane. 120

List of Tables

2.1 First solutions of Eq. (2.60). 30

Chapter 1

Introduction

The study of fluid adsorption on microstructured substrates is currently an area of great interest, especially because of the amazing technological advances that allowed the manufacture and design of solid microstructured surfaces at scales ranging from the micrometer to nanometer [53,135]. For example, using elastomer seals, vapor deposition, photolithography or dewetting of polymer thin film hydrophobic and hydrophilic domains of well-characterized geometry on plane substrate may be generated [150]. Likewise it is possible to sculpt grooves on a homogeneous substrate of controlled section such as linear wedges or conical geometry on the micro- and nano-scales [149], which has allowed experimental studies of the influence of the geometry on fluid adsorption [16–19, 27, 45, 54, 57].

These advances are critical to the emerging microfluidics industry [148, 149] that involves the handling and manipulation of very small fluid volumes, which can lead to miniaturization of chemical synthesis reactors [67] (see Figure 1.1(a)), optimizing syntetic efficiency preparing sensitive compounds on automated multistep synthesis. Moreover, these technologies have challenging applications to life science [106], specially for biological analysis equipment [55, 78] (see Fig. 1.1(b)). These microfluidic devices can be integrated like a silicon chip [65], with an analogous role to that of the silicon chip in the electronic revolution. This analogy is based on that while microelectronics focuses on the flow of electrons on an engraved surfaces, microfluidic is about adsorption and flow of a microscopic amounts of fluid along channels or chemically sculpted prints. These lab-on-chip (LOC) devices represent an emerging technology with potential applications like in medical diagnosis [145] and biomedical research [133], bubble-driven bioengineering [77], or programmable motion and pattering of molecules on solid surfaces [138] (see Fig. 1.2(a)). Furthermore, fluid absorbed on microstructured substrates has attracted much attention in a wide variety of engineering fields [60] different

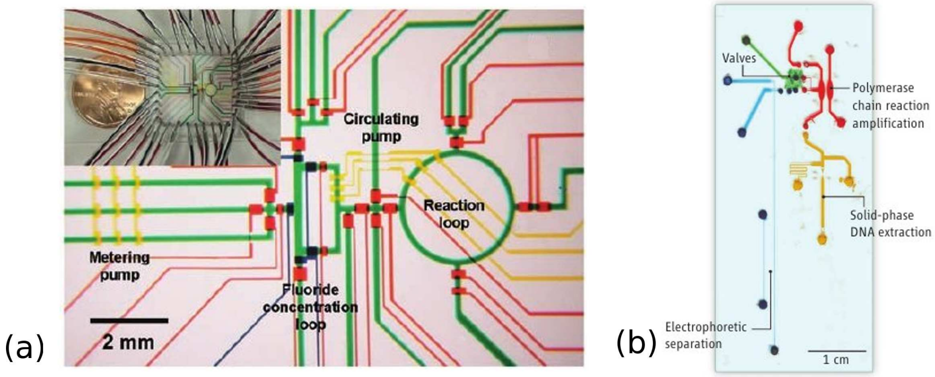
(a)
Circulating pump
Reaction loop
Metering pump
Fluoride concentration loop
2 mm
(b)
Valves
Polymerase chain reaction amplification
Solid-phase DNA extraction
Electrophoretic separation
1 cm

Figure 1.1: (a) Optical micrograph of the central area of the chemical reactor circuit used in the production of 2-deoxy-2-fluoro-D-glucose (FDG) (from Ref. [67]). (b) An integrated microfluidic chip for genomics that analyses short tandem repeats (from Ref. [145])

from the microfluidics industry, such as self-cleaning surface coatings for solar cells, anti-icing agents, buildings materials, and the oil and gas industry.

Almost all our current knowledge about fluids on surfaces is based on macroscopic arguments, but at the microscale the fluid behaviour can very different [106]. In the micrometer scale the effects of the thermical fluctuations are vital in the statistical-mechanic treatment of the problem, playing a role analogous to the quantum effects in electronic. The structure of the substrate leads to a dramatic increase in interfacial fluctuations that must be considered in the design of microfluidic devices, since ultimately it limits the quality of controlled flow and therefore the degree of miniaturization that is good for the applications. Microfluidics is obviously related to the development of nanotechnology, which are estimated moves of investment values of the order of billions of euros worldwide.

Different phenomenological laws for fluid adsorption on rough substrates have been proposed, such as the Wenzel law [146, 147] and the Cassie-Baxter law [22] (see Fig. 1.4(b)). Wenzel's law assumes that, as roughness increases the surface in contact with the fluid, there is a change in the total surface energy, which is proportional to the area of this surface. This simple fact modifies the wetting characteristics of the solid through Young's equation, so the contact angle θ_r of a droplet on a rough substrate is related to the corresponding one for an ideally planar surface θ_π as $\cos\theta_r = r\cos\theta_\pi$, where the *roughness factor* r is the ratio between the surface area and its projection on the reference plane. Cassie-Baxter's law is applied to porous hydrophobic surfaces (see Fig. 1.3), and assumes that gas pockets are trapped between the

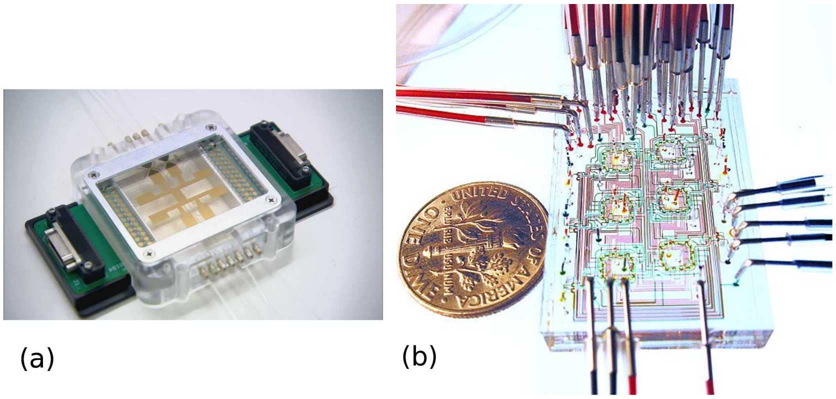

Figure 1.2: (a) Sandia Digital Microfluidic Hub, a droplet-handling router (picture taken of Sandia National Labs). (b) Microfluidic chip houses bioreactors, where bacteria can be cultured and observed (picture taken of Frederick Balagadde (Stanford Researchers))

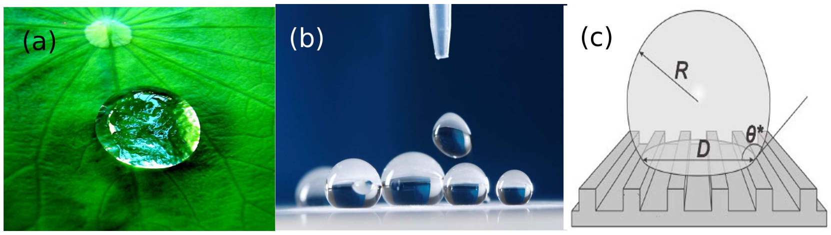

Figure 1.3: (a) Picture of a drop on a lotus leaf (picture taken of Wikimedia Commons). (b) Laser micro and nano-structuring (picture taken of Fraunhofer Institute for laser Technology). (c) Schematic illustration of a droplet on a superhydrophobic stripes (from Ref. [34])

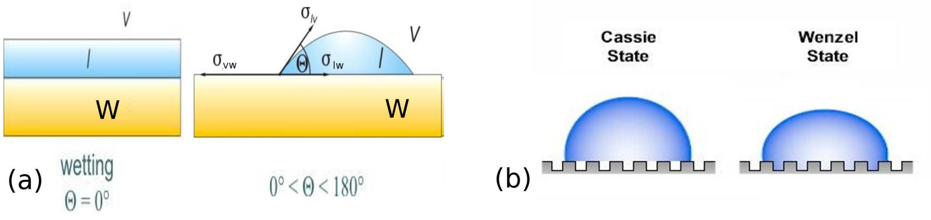

Figure 1.4: (a) Schematic illustration of the wetting transition (picture taken from the Low Temperature Physics group website in Konstanz Universität). (b) Schematic illustration of the Cassie-Baxter and Wenzel models (picture taken of Carl Clegg, Rame-hart Instrument Co.).

liquid droplet and the surface. So, the contact angle for the rough substrate is described by the equation $\cos\theta_r = f_1 \cos\theta_\pi - f_2$, where f_1 is the total area of solid-liquid interface and f_2 the total area of liquid-trapped air interface When $f_2 \to 0$ the Wenzel law is recovered. Cassie-Baxter's law works well for the large contact angle regime, i.e. superhydrophobicity, and the Wenzel's law for intermediate values.

From a statistical-mechanic point of view, the adsorption phenomenon of fluid onto a substrate is understood as the formation of a mesoscopic thickness layer of liquid phase at the interface substrate-vapor under saturation conditions (liquid-vapor coexistence). There are numerous phase transitions related to this phenomenon. For example, in a planar substrate without structure, a macroscopic layer of liquid can be interposed completely between the substrate and the vapor volume. This phenomenon is the wetting transition [21, 33, 35, 43, 134, 137] (see Fig. 1.4(a)), that from a macroscopic viewpoint is observed as a decrease in contact angle θ to zero of the macroscopic drop of liquid formed on the substrate. In addition, sculpted [112] or chemically structured [46, 63] substrates undergo other related interfacial transitions such as the filling transition [30, 48, 107], where the morphology of the liquid layer on the substrate is modified by changing the thermodynamic conditions of the system.

The study of fluid adsorption on rough substrates is addressed in the literature from two perspectives. First, the study from the microscopic point of view, in which explicitly takes into account the interactions between the constituents of the fluid and substrate. This makes possible to obtain macroscopic properties such as surface tensions from the microscopic parameters. This approach has been treated both at the analytical level, by considering simple models such the Ising model, or more recently, by density-functional theories, which go from simple square-gradient functionals, to more sofisticated functionals such as Fundamental Measure Theory [70–73, 75], as well

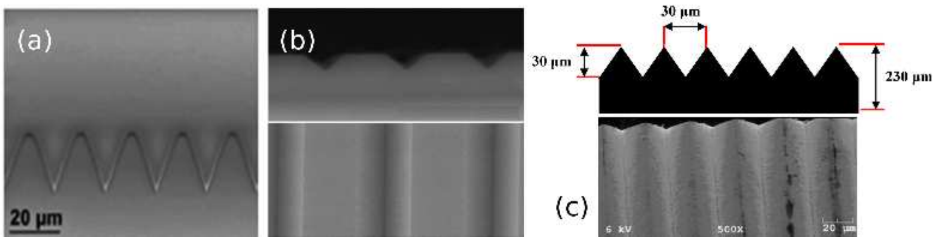

Figure 1.5: Micro and nanostructured surfaces of wedges and sawtooth patterns: (a) Surface patterned by photolithography (from Ref. [28]), (b) Cross section and top view of a silicon patterned surface (from Ref. [17]), (c) Sawtooth microfeatures on a belt mold electroformed nickel alloy sheets (from Ref. [44])

as by computer simulation. However, the relevant spatial scales in the adsorption phenomenon of fluids on microstructures are often much larger than those of the microscopic interactions, making it difficult to make a proper study of phenomenology that appears in these scales. The alternative to this approach is a mesoscopic description of the problem, where the irrelevant degrees of freedom are integrated out and the problem is reduced to the analysis of the behavior of the liquid-vapor interface near the substrate. In this approach, the interfacial free energy of the system is usually described by an interfacial Hamiltonian which accounts for the excess free energy for a constrained interfacial configuration. On this scale the effect of interfacial fluctuation (known as capillary waves) is evident. Their main effect is the blurring of the position of the interface (roughness) and the appearance of powerful correlations in directions parallel to interface. The spectrum of the fluctuations may be altered by structuring the substrate. So, for example, for wedge-shaped substrates, it is observed that the relevant fluctuations are quasi-one-dimensional along the channel direction (so called breathing modes) [97, 101].

The connection between the two ways of treating the problem is not obvious. In most cases, the effective Hamiltonian in the mesoscopic description is introduced in a plausible way, from the accepted expression for flat substrates [119], but in any case in an *ad hoc* manner. However, some proposals for the interfacial Hamiltonian that could be reasonable at first glance, show inconsistencies with microscopic descriptions when applied to the problem of adsorption on microstructured substrates [87]. It is therefore essential to find the connection between the interfacial Hamiltonians with the underlying microscopic description to advance in the theoretical study of this problem. For short-range interactions, the first attempts to establish a connection was made by Fisher and Jin [41, 42, 58, 59]. In these works, starting from the Landau-Ginzburg-Wilson model, they obtained formally an interfacial Hamiltonian associated to the problem, and solved it perturbatively for shallow interfaces. This problem was revisited by Parry *et al.* [91, 92, 99]. They showed that in the general case (rough substrates and/or interfaces) the interfacial Hamiltonian has still the structure proposed previously in the literature, but the binding potential between the liquid-vapour interface and the substrate is no longer a function, but a non-local functional of the interfacial and substrate profiles, which can be expressed diagrammatically in terms of the Ornstein-Zernike correlation function. More recently it has been shown that this new effective Hamiltonian reproduces the behavior of the correlations between two points at midfield level, identifying a new length ξ_{NL} that effectively defines a wavelength cutoff below which the interfacial fluctuations are damped, and certain rules of exact sums for the complete wetting transition [93, 94, 98]. The effect of interfacial fluctuations has been characterized and tested using renormalization group techniques and Monte Carlo computer simulations [91,98]. The results are consistent with each other, and contradict earlier results of Fisher and Jin, who predicted that the continuous (second order) wetting transition in the mean-field approximation, could become first order due to the interfacial fluctuations [41,42,58,59]. Moreover, the existence of the length ξ_{NL}, helps to explain the apparent reduction in the effect of fluctuations on the critical wetting transition observed in computer simulations of the Ising model [10, 11, 86].

We should mention that there are alternatives forms to obtain the interfacial behavior in mesoscale systems, from a microscopic description. For example, Chacon and Tarazona recently have developed a method for a liquid-vapor free interface that defines the intrinsic interface from computer simulation results, from which analyze the effect of capillary fluctuations [13, 14, 23–25, 32].

The purpose of this thesis is to deepen into the statistical-mechanical description in the adsorbed layers of simple fluids in the mesoscale. We will revisit the study of fluid adsorption on rough substrates, paying special attention to filling and wetting transitions on prototypical cases like the wedge and sinusoidal geometries, which can be produced experimentally (see Figs. 1.5 and Fig. 1.6). However, we note that other substrate geometries have been also studied recently in the literature, such as capped capillaries [31, 69, 76, 95, 116, 131, 151], crenellated substrates [70, 141, 142] and parabolic pits [27, 62, 141, 142].

In Chapter 2 we will consider the effect of interfacial fluctuations on the filling transition in a wedge. This transition has been studied extensively in last years [1, 2, 5, 6, 8, 12, 47, 50–52, 73, 74, 80, 81, 87, 90, 96, 97, 101, 115, 119,

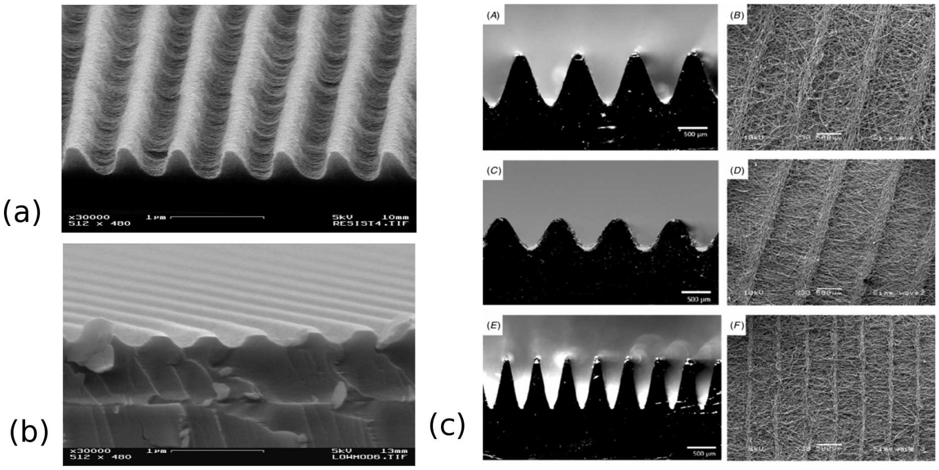

Figure 1.6: Sinusoidal micro and nano-structured surfaces: (a) and (b) 1740 lines/mm ion milled fused silica substrate (picture taken of James Oliver - MSC- 2004). (c) Manufactured sinusoidal RP resin formers and the resulting electrospun PLGA scaffolds (from Ref. [124])

125–128, 130]. We focus on the effect that a modification of the substrate-fluid interactions in a small region close to the wedge bottom has on the filling transition. Previous studies based on the beather-mode theory for the 3D infinite wedge geometry indicate that, for short-ranged forces, the filling transition may be driven first-order by the introduction of this term, with a tricritical point as borderline [125–127]. We have explored this possibility by Monte Carlo simulations. For comparison, we modified the breather-mode theory to the finite geometry considered in the simulations, and we got an analytical solution in the critical and tricritical regime to compare with the Monte Carlo results. We find strong evidences of the existence of a tricritical point at wedge filling by tuning the linear tension associated to the wedge bottom. Close to it, there is a good agreement between theory and simulation results. So, we conclude that this line tension is a relevant field in the renormalization-group sense.

In Chapters 3 and 4 we will study the mean-field interfacial phase diagram of fluids on sinusoidal substrates. This geometry has also been studied extensively [26, 114, 117, 118, 140]. Unlike previous interfacial Hamiltonian studies [114, 117, 118], which were restricted to shallow substrates, we consider intermediate and large values of the roughness. We will consider two coarse-grained microscopic models: the Landau-Ginzburg model in Chapter 3 and the double parabola model in Chapter 4. The latter is interesting because can be regarded as an approximation to the Landau-Giznburg model, and also because in some limit generates the non-local interfacial Hamiltonian model [91]. So, this study may help to bridge the gap between the microscopic and mesoscopic descriptions of adsorption phenomenology in the mesoscale. Our results are analyzed and compared with previous approaches, in particular the macroscopic theory and interfacial Hamiltonian model studies. While the techniques used to obtain the mean-field phase diagram for the Landau-Ginzburg model were standard (finite-element method with a conjugate gradient minimization procedure), we have developed a minimization procedure for the double parabola model which links it to the non-local interfacial Hamiltonian model.

Chapter 2

Critical and tricritical wedge filling transitions

2.1 Introduction

Experimental and theoretical studies have shown that fluids in contact with a non-planar substrate show new interfacial phenomena [33], and the wedge filling transition is an example. The filling transition can be viewed as the unbinding of liquid-vapour interface from the wedge bottom. The origin of this transition can be rationalized from (macroscopic) thermodynamic arguments [48, 119]. Let us consider a 3D wedge characterized by a tilt angle α (see Fig. 2.1). The substrate is chemically homogeneous and favours the condensation of liquid close to it. If the wedge is in contact with a near-saturated bulk gas, it will be filled with liquid up to a height ℓ above the wedge midpoint. If translational symmetry along the wedge axis is assumed, the liquid-vapour interface is given by a cylindrical section with a curvature radius R given by the Laplace equation [64]

$$R = \frac{\sigma_{lv}}{|\Delta p|} \tag{2.1}$$

Here $\Delta p = p - p_l$, where p is the gas pressure and p_l the pressure of the metastable liquid phase at chemical equilibrium with the bulk gas. On the other hand, σ_{lv} is the liquid-vapour interfacial tension. From Eq. (3.26), the liquid-vapour interface must be flat at saturation conditions, as $p_l = p$. Under these circumstances, and assuming a mirror symmetry respect to the $x = 0$ plane, the interfacial free energy f_w (substracting the bulk contribution $-pV$) must contain a thermodynamic contribution

$$f_w = \sigma_{lv}\mathcal{S}_{lv} + \sigma_{wl}\mathcal{S}_{wl} + \sigma_{wv}\mathcal{S}_{wv} \tag{2.2}$$

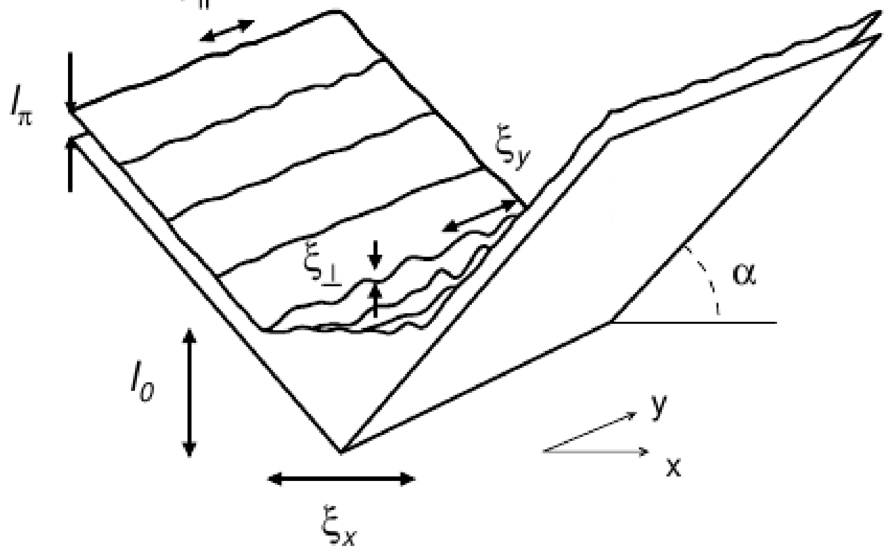

$\xi_{\parallel}$
l_{π}
ξ_y
$\xi_{\perp}$
α
l_0
y
x
ξ_x

Figure 2.1: Schematic illustration of a typical interfacial configuration in the wedge geometry showing the relevant diverging length scales at the filling transition (from Ref. [97])

where σ_{wv}, σ_{wl} are the wall-vapor and wall-liquid surface tensions, respectively, and $\mathcal{S}_{lv}$, $\mathcal{S}_{wl}$ and $\mathcal{S}_{wv}$ are the areas of the liquid-vapour, wall-liquid and wall-vapour interfaces, respectively. In order to characterize the wedge filling transition, we will compare the filled state free energy with the corresponding to the completely dry state, i.e.

$$f_w^0 = \sigma_{wv}\mathcal{S}_{wv}^0 \tag{2.3}$$

where $\mathcal{S}_{wv}^0$ is the substrate area. Note that $\mathcal{S}_{lv} + \mathcal{S}_{wl} = \mathcal{S}_{wv}^0$. So, the excess interfacial free energy with respect to the dry state, $\Delta f_w \equiv f_w - f_w^0$, is given by:

$$\Delta f_w = \sigma_{lv}\mathcal{S}_{lv} + (\sigma_{wl} - \sigma_{wv})\mathcal{S}_{wl} \tag{2.4}$$

If we take into account Young's equation [152]

$$\cos\theta = \frac{\sigma_{wv} - \sigma_{wl}}{\sigma_{lv}} \tag{2.5}$$

where θ is the contact angle of a sessile drop on a *flat* substrate of the same composition, Eq. (2.4) can be rewritten as

$$\Delta f_w = \frac{2\sigma_{lv}L_y(\cos\alpha - \cos\theta)\ell}{\sin\alpha} \tag{2.6}$$

where we took into account that $\mathcal{S}_{lv} = 2L_y\ell/\tan\alpha$ and $\mathcal{S}_{wl} = 2L_y\ell/\sin\alpha$, with L_y being the length along the wedge axis. Thus, Eq. (2.6) shows two possible situations [30, 48, 107]. If the contact angle is $\theta > \alpha$, the wedge is partially filled with a value of ℓ which depends on the intermolecular forces and fluctuations. On the other hand, if $\theta < \alpha$, the wedge is completelly filled with liquid. The border case $\theta = \alpha$ corresponds to the filling transition. Note that the contact angle is a function of the temperature, so this condition defines a transition temperature T_f. On the other hand, as usually θ decreases with the temperature, the filling transition occurs before the wetting transition for the flat substrate, which occurs at a temperature T_w where $\theta(T_w) = 0$. From a macroscopic point of view, at the filling transition the interface can be found at any height ℓ, without any change of the excess interfacial free energy Δf_w. This means that higher-order contributions can play a role to determine the interfacial behaviour at filling, and the transition order. In particular, filling transitions, as the wetting transitions, may be either first-order, with a sudden jump of the equilibrium liquid adsorption as the filling transition is reached, or critical, where the amount of adsorbed liquid diverges as the filling transition is approached. The wedge case offers two new examples of critical transitions: *the critical filling transition*, in which the interfacial height ℓ at the mid-point of the wedge diverges when $T \to T_f^-$ along the coexistence line, and *the complete filling transition*, when the chemical potential $\mu \to \mu_{sat}$ for $T > T_f$. Critical transitions are characterized by critical exponents that determine the divergent behavior of the characteristic lenghtscales of the system (see Fig. 2.1). So, the average mid-point interfacial height $\ell_w \equiv \langle \ell \rangle$, the correlation length ξ_y along the wedge axis, the correlation length ξ_x across the wedge, and the roughness $\xi_\perp$ display the following power-law singularities [101]

$$\ell_w \sim t^{-\beta_s} \qquad \xi_\perp \sim t^{-\nu_\perp} \qquad \xi_x \sim t^{-\nu_x} \qquad \xi_y \sim t^{-\nu_y} \tag{2.7}$$

for $t \to 0$, where t is defined as $(T_f - T)/T_f$ for the critical filling, or replaced by $h = \mu_{sat} - \mu$ for complete filling. For the former, note that as θ is well-behaved as a function of the temperature close to the filling transition, $t \propto \theta - \alpha$.

From a statistical mechanical perspective, the wedge filling phenomenon has been studied at different levels: in microscopic models such as the Ising model [1,2,5,12,80,81], density-functional theories [8,47,73–75] and interfacial Hamiltonian models [6,12,47,50–52,87,90,96,97,101,115,119,125–128,130]. In the latter approach, the bulk degrees of freedom are traced out, so the contribution to the free energy of an interfacial configuration depends only on the interfacial height field relative to the horizontal $\{\ell(\mathbf{r})\}$, and it has two contributions: the energy cost of increasing the liquid-vapour interfacial area, and a binding potential term which accounts for the direct influence of the molecular forces and wetting properties of the wall. So, the interfacial Hamiltonian of the so-called drumhead model is [119]

$$\mathcal{H}[\ell] \equiv \beta H[\ell] = \int d\mathbf{r} \left\{ \Sigma \sqrt{1 + (\boldsymbol{\nabla}\ell)^2} + W(\ell) \right\} \tag{2.8}$$

Here $H[\ell]$ is the free-energy contribution of an interfacial configuration, $\beta = 1/(k_B T)$, $\Sigma = \beta\sigma_{lv}$ and $W(\ell)$ is the binding potential between the liquid-vapour interface and the substrate. We assume that the binding term is local, but more sophisticated model replace this contribution by a non-local functional [7, 88, 91–94, 98, 99]. Although some work was carried out considering the drumhead model [3, 119], most of the studies in the literature consider the shallow wedge limit, in which α is small. Then Eq. (2.8) can be expanded in powers of $|\nabla\ell|$ up to an irrelevant constant as:

$$\mathcal{H}[\ell] = \int\int d\mathbf{r} \left\{ \frac{\Sigma}{2} (\nabla\ell)^2 + W_\pi(\ell - \alpha|x|) \right\} \tag{2.9}$$

where W_π is the binding potential associated to a flat substrate. The mean-field analysis can extract information about the order of the filling transition and the shape of the interface. At shallow wedge aproximation it is possible minimizate the functional (2.9) assuming translational symmetry along the wedge axis, yielding to the Euler-Lagrage equation for the equilibrium interfacial profile

$$\Sigma\ddot{\ell} = W'(\ell - \alpha|x|) \tag{2.10}$$

where the dot corresponds to the derivative with respect to the cross-direction coordinate x. By integrating we arrive to a condition for the mid-point height [97, 101, 119]

$$\Sigma\alpha^2/2 = W(\ell_w) - W(\ell_\pi) \tag{2.11}$$

being ℓ_π the planar wetting film thickness, ans ℓ_w the mid-point height. The planar binding potential have the usual form [33]

$$W_\pi(\ell) \;=\; \bar{h}\ell + \frac{a}{\ell^p} + \frac{b}{\ell^q} \qquad \ell > 0, \tag{2.12}$$

with $\bar{h} \propto (\mu_{sat} - \mu)$, a and b are effective Hamaker constants and $q > p > 0$ allow for general types of intermolecular potentials. For short-ranged forces:

$$W_\pi(\ell) \;=\; \bar{h}\ell + ae^{-\kappa\ell} + be^{-2\kappa\ell} \qquad \ell > 0, \tag{2.13}$$

So at bulk coexistence Young's equation implies $W(\ell_\pi) = -\Sigma\theta^2/2$ and at filling transition temperature, where $l_w \to \infty$ the macroscopic result $\theta = \alpha$ is recovered. The filling transition can be first or second (critical) order like wetting. For critical filling, Eq. (2.12) leads to the condition $\ell_w \sim (\theta - \alpha)^{1/p}$ (or $\log(\theta - \alpha)$ for short-ranged forces). These interfacial Hamiltonian models show that critical filling is less restrictive than for the critical wetting, and it can be critical even though the wetting transition corresponding to the flat substrate is first order, while remains second-order for flat substrates which present critical wetting [97, 101]. However, this prediction has been questioned from the results obtained from mean-field density functional theories, where filling transition can become first order for acute wedges even when the wetting transition of the flat substrate is critical [8]. On the other hand, the filling transition becomes critical in presence of fluid-wall long-ranged forces (first-order wetting), but the mechanism of this change seems to be different from the the proposed for interfacial Hamiltonian models [73–75]. Finally, for short-ranged forces, an unexpected connection between critical wetting and filling is observed, as the midpoint interfacial height in the wedge is related to the interfacial height of a planar wall via the relation [47]:

$$\ell_w(\theta, \alpha) \;=\; \ell_\pi(\theta - \alpha) \tag{2.14}$$

This condition is called the (mean-field) wedge covariance, and it is also fulfilled by density-functional theories [8, 47]. However, in general wedge covariance is not satisfied for long-ranged forces, unless $q = 2p$ in Eq. (2.12) [47].

Interfacial fluctuations are essential to characterize critical filling. In general, their role will depend on the dimensionality of the system and the spacial range of the interaction potentials. The filling transition on a 2D wedge have been studied by effective interfacial Hamiltonian, with exact results for some quantities like the interfacial free energy and the midpoint interfacial height probability distribution function (PDF) [96]. In particular, for most physically meaning binding potentials, both complete filling and critical filling are characterized by universal critical exponents but while the first has a geometrical and thermodynamic origin, the second is a consequence of strong fluctuation effects [96]. Heuristic scaling theory predicts that 2D wedge critical filling can fall into a mean-field (FMF), where the critical exponents are the same as in the mean-field theory, or fluctuation-dominated (FFL) regime [100], depending on whether the value of p of the binding potential (2.12) is less or greater than the marginal value $p^* = 1$. This is in contrast with the scaling regimes of critical wetting, where strong, intermediate and mean-field regimes can be identified depending on the values of both p and q. The values of the critical exponents are [96, 100]

$$\begin{aligned} &\beta_s = \nu_x = \frac{1}{p} \qquad && \nu_\perp = \tfrac{1}{2} + \tfrac{1}{2p} \qquad && FMF \\ &\beta_s = \nu_x = \nu_\perp = 1 && && FFL \end{aligned} \tag{2.15}$$

Note that the FFL regime includes most physically meaning situations, such as short-ranged potentials ($p = \infty$) and van der Waals dispersion forces ($p = 2$)

These predictions have been confirmed by exact solutions of interfacial Hamiltonian models by using transfer-matrix methods [96,128]. In particular, for short-ranged forces, the interfacial free energy F_{wedge} and the average midpoint interfacial height $\ell_w = \langle \ell_0 \rangle$ satisfy [96]

$$F_{wedge} \sim \ln(T_f - T) \qquad \ell_w \sim \xi_\perp \sim \frac{1}{T_f - T} \tag{2.16}$$

As in the mean-field case, a connection between apparently unrelated phenomena is observed: in the FFL regime the filling critical exponents $\beta_s = \nu_\perp = 1$ are identical to the SFL regime for critical wetting [96]. Moreover, this connection extends to the interfacial height PDF for each transition. Specifically, for short-ranged forces and in the scaling limit, the midpoint interfacial height PDF $P_w(\ell; \theta, \alpha)$ is identical to the interfacial height PDF for critical wetting $P_\pi(\ell; \theta)$, but for a shifted contact angle $\theta - \alpha$

$$P_w(\ell; \theta, \alpha) = P_\pi(\ell; \theta - \alpha) \tag{2.17}$$

where $P_\pi(\ell) = e^{-\ell/\ell_\pi}/\ell_\pi$. This condition automatically ensures that the critical exponents β_s and $\nu_\perp$ are the same for both critical phenomena. Wedge covariance is also observed for the marginal case $p = 1$ [128].

Analysis of the interfacial structure and height-height correlation functions [128] identify the breather modes [97, 101] as the most relevant interfacial fluctuations in 2D wedge critical filling. In this picture the interface is effectively infinitely stiff in the filled region and is driven by fluctuations of the midpoint interfacial position, i.e. critical effects at 2D wedge filling arise simply from local translations in the height of the flat, filled interfacial region. As a consequence, ξ_x is related geometrically with ℓ_w as $\xi_x = \ell_w/\tan\alpha \approx \ell_w/\alpha$.

Most of these studies consider the shallow wedge limit, so their conclusions may be affected by this approximation. However, the most important predictions have been confirmed for studies which consider acute wedges. For example, Abraham *et al.* studied the drumhead model for the 2D wedge with short-ranged forces by transfer-matrix techniques [3], demonstrating that the covariance relations are the same as in the shallow wedge limit. Furthermore, exact theoretical analysis of the Ising model for $\alpha = \pi/4$ [1, 2], as well as Monte Carlo simulations of this model [5] also confirm the validity for acute wedges of the previous predictions.

We now turn to the three-dimensional case. In order to characterize the fluctuation effects in 3D critical wedge filling, Parry *et al.* studied the Gaussian fluctuations around the mean-field solution [97, 101]. In particular, they evaluated the height-height correlation function $\mathcal{G}$, and the structure factor S (its Fourier transform)

$$\mathcal{G}(x, x'; \tilde{y}) \equiv \langle \delta\ell(x, y)\delta\ell(x', y')\rangle \tag{2.18}$$

$$S(x, x'; \mathcal{Q}) = \int d\tilde{y}\, e^{i\mathcal{Q}\tilde{y}}\mathcal{G}(x, x'; \tilde{y}) \tag{2.19}$$

with $\tilde{y} \equiv y' - y$ and $\delta\ell \equiv \ell(x, y) - \langle \ell(x, y)\rangle$ Assuming that the fluctuations about the mean-field solution are small, a Gaussian expansion of $\mathcal{G}[\ell]$ leads to the Ornstein-Zernike equation

$$\left(-\Sigma\frac{\partial^2}{\partial x^2} + \Sigma\mathcal{Q}^2 + W''_\pi(\ell(x) - \alpha|x|)\right)S = \delta(x - x') \tag{2.20}$$

If we assume that S can be expanded in powers of Q^2, it follows that in the scaling regime:

$$S(x, x'; \mathcal{Q}) = \frac{S_0(x, x')}{1 + \xi_y^2 Q^2} \tag{2.21}$$

where S_0 is the zero-moment of S, given by:

$$S_0(x,x') = (|\dot{\ell}(x)| - \alpha)(|\dot{\ell}(x') - \alpha)\left\{\frac{1}{2\alpha W'_\pi(\ell_w)}\right.$$
$$\left. + \frac{\Theta(xx')}{\Sigma}\int_0^{\min(|x|,|x'|)} \frac{dx}{(\dot{\ell}(x)-\alpha)^2}\right\} \qquad (2.22)$$

where ℓ_w is the average (mean-field) midpoint interfacial height. On the other hand, $\xi_y = \sqrt{\Sigma\ell_w/W'_\pi(\ell_w)}$. In essence, the interface is flat, i.e. $\ell(x) \approx \ell_w$, for $x \lesssim \ell_w/\alpha$, while for $x \gtrsim \ell_w/\alpha$ the height decays exponentially fast to its planar limit. Consequently, $\xi_x \sim 2\ell_w/\alpha$. So, in addition to $\beta_s = 1/p$, it is found that $\nu_y = 1/p + 1/2$ and $\nu_x = 1/p$, so fluctuations are highly anisotropic and dominated by the modes along the wedge since $\xi_y \gg \xi_x$. Finally, the roughness satisfies $\xi_\perp \sim \sqrt{\xi_y/\Sigma\ell_w}$, so $\nu_\perp = 1/4$ [97, 101].

In order to go beyond mean-field, and taking into account the highly asymmetric nature of the interfacial fluctuations observed in the mean-field approach. Close to filling transition boundary, ξ_y becomes arbitrarily larger than ξ_x, impliying that the interfacial fluctuations become pseudo-one-dimensional. Consequently, assuming that interface is locally flat across the wedge for a given constrained configuration of the mid-point interfacial height $\ell_0(y)$ and the fluctuation effects are dominated by pseudo-one-dimensional local translations in the height of the filled region along it, Parry *et al.* [97, 101] reduced Eq. (2.9) to

$$\mathcal{H}_W[\ell_0] = \int dy \left\{\frac{\Sigma\ell_0}{\alpha}\left(\frac{d\ell}{dy}\right)^2 + V_W(\ell_0)\right\} \qquad (2.23)$$

where the coefficient of the gradient term is proportional to the local interfacial height describing the bending energy of long-wavelength fluctuations along the wedge, and V_W is the effective filling potential which has the general expansion

$$V_W(\ell) \;=\; \frac{\bar{h}\ell^2}{\alpha} + \frac{\Sigma(\theta^2-\alpha^2)\ell}{\alpha} + \frac{A_F}{(p-1)}\ell^{1-p} + \dots \qquad (2.24)$$

where exponent p is the same as in Eq. (2.12). The first two terms reflect the bulk and surface thermodynamic costs of forming a filled region [47]. The last contribution arises from the fluidsolid interactions so that A_F is the effective Hamaker constant associated with the attractive part of the wallfluid interface binding potential.

This model can be easily extended for acute wedges as [125–127]

$$\mathcal{H}_W[\ell] = \int dy \left\{\frac{\Lambda(\ell)}{2}\left(\frac{d\ell}{dy}\right)^2 + V_W(\ell)\right\} \qquad (2.25)$$

where

$$\Lambda(\ell) \approx \frac{2\Sigma\ell}{\tan\alpha} \tag{2.26}$$

and

$$V_W(\ell) \approx \frac{\bar{h}\ell^2}{\tan\alpha} + \frac{2\Sigma(\cos\alpha - \cos\theta)\ell}{\sin\alpha} + \frac{A_F}{(p-1)}\ell^{1-p} + \dots \tag{2.27}$$

Scaling arguments [97,101] show that there are again two different fluctuation regimes, as in the two-dimensional case: the FMF regime for $p < 4$, where the critical exponents are those obtained from the mean-field and Gaussian fluctuation analysis described above, and the FFL regime for $p > 4$, where the critical behaviour is dominated by the interfacial fluctuations, with critical exponents $\beta_s = \nu_x = \nu_\perp = 1/4$ and $\nu_y = 3/4$. These predictions have been confirmed by Monte Carlo simulations of the Ising model in a double wedge [9,80,81].

The quasi-one-dimensional character of the Hamiltonian (2.25) means that it is amenable to an analytic solution by path integral techniques [20,39] As a position-dependent stiffness coefficient is present, care is required in defining the partition function and its measure [6]. This issue is similar to the "factor-ordering" problem in solid-state quantum mechanics when there is an effective position-dependent mass [29,144]. Refs. [125–127] propose a prescription which provides a solution which is mathematically consistent and agrees with necessary thermodynamic requirements. In particular, the midpoint interfacial height PDF for critical filling shows a short distance expansion $\propto \ell^3$, consistent with scaling arguments [47]. This is the necessary dependence that ensures thermodynamic consistency with exact sum-rules for the filling fluctuation regime, which dictate that the local density at the wedge bottom $\rho_W(0)$ is non-singular, i.e. $\rho_W(0) - \rho_\ell \sim T - T_f$, where ρ_ℓ is the bulk liquid density, and T_f is the filling transition temperature [88].

For the case of short-ranged forces, there is an additional field relevant for the filling phenomenon. Note that, in absence of binding potential (i.e. contact binding potential), the interfacial phenomenology is determined by the line free energies associated with the three-phase liquid-vapour-substrate lines and to the wedge bottom when the interface is either pinned at the wedge or away from it [127]. These line free energies are associated with deviations of the density profiles with respect to the flat surface ones, induced by three-phase coexistence and enhanced packing effects or stronger interactions near the wedges. At a mean-field level, we expect that, if the line free energy associated with a wedge in contact with the vapour is smaller than the sum of the three-phase line free energies and the line free energy associated with a wedge in contact with the liquid, then the gas-liquid interface will be pinned at the wedge bottom. Otherwise, the interface will unbind from the wedge. In this sense, the difference of total line free energies for the different considered situations can be understood as a pinning contact potential of strength $-U$ for the gas-liquid interface [125–127]. Exact calculations on the breather mode model (2.25) show that along the filling transition boundary $h = 0$, $\theta = \alpha$, two different situations may arise depending on the value of U [125–127]. Above some value U_{tc}, the interface remains bound to the wedge bottom as $\theta \to \alpha^+$ implying that the filling transition is of first- order. Below U_{tc}, the interface is delocalized and the filling transition, occurring as $\theta \to \alpha^+$, is critical. The borderline situation $U = U_{tc}$ corresponds to a tricritical point [125–127]. As U_{tc} is non-zero, interfacial fluctuations shift the unbinding value for the pinning potential strength. For 3D wedge there is no wedge covariance relationships for short-ranged forces, since fluctuaction effects play a central role in the filling transition in contrast to the wetting, where the fluctuations effects are negligible and the critical exponents are mean-field-like for finite p (for short-ranged forces, they are marginal). However, exact calculations on the breather-mode theory and generalized random walk arguments show a connection between 3D critical filling and 2D random-bond complete wetting, as well as between 3D tricritical filling and 2D random-bond critical wetting [126].

To finish our introduction, we mention that the breather-mode Hamiltonian model can be improved by introducing as new degrees of freedom tilt and torsional modes [47]. In this approach, a small local tilt for the flat filled interfacial region is allowed, so $\ell(x,y) = \ell_0(y) + \phi(y)x$ provided that $\ell(x,y) < \alpha|x|$, and a tilt angle between $-\epsilon\alpha \leq \phi \leq \epsilon\alpha$ with $0 < \epsilon < 1$. The contribution to the free energy of an interfacial configuration is given by

$$\mathcal{H}_{BTT}[\ell_0, \phi] = \tag{2.28}$$

$$= \int dy \left\{ \frac{K_1}{2}\ell_0 \left(\frac{d\ell_0}{dy}\right)^2 + \; K_2 \ell_0^2 \phi \left(\frac{d\ell_0}{dy}\right)\left(\frac{d\phi}{dy}\right) + \frac{K_3}{2}\ell_0^3 \left(\frac{d\phi}{dy}\right)^2 + V(\ell_0,\phi) \right\}$$

where, $K_1 = \frac{2\Sigma}{\alpha}$ is the bending energy coefficient, $K_2 \propto \frac{\Sigma}{\alpha^2}$ and $K_3 \propto \frac{\Sigma}{\alpha^3}$ the coefficients of the torsional terms. The generalized wedge potential for short range interactions (at bulk coexistence) is:

$$\begin{aligned} V(\ell_0,\phi) &= \frac{\Sigma}{\alpha}\left(\theta^2 - \alpha^2 + \phi^2\right)\ell_0 + \Delta V_W(\ell_0) \; = \\ &= t\ell_0 + \frac{\Sigma}{\alpha}\phi^2 \ell_0 + \Delta V_W(\ell_0) \end{aligned} \tag{2.29}$$

where the temperature-like scaling field is $t \propto (T_f - T) \propto (\theta - \alpha)$, and $\Delta V_W(\ell_0)$ is the contact-like potential defined in Eq. (2.24) . Note that if we consider $\phi = 0$ the BBT model reduces to the original wedge Hamiltonian (2.25) which account only for the breather-modes excitations. Furthermore, under a renormalization group rescaling of coordinates and fields, the term of the generalized potential $\phi^2 \ell_0$ remains invariant, and the new renormalized tilt and bending energy coefficients $K_2 \to K_2' = b^{-4/3} K_2$ and $K_3 \to K_3' = b^{-4/3} K_3$ are irrelevant for all ranges of molecular forces. So the critical behaviour of the BTT model can be simplified to

$$\mathcal{H}_{BTT}[\ell_0, \phi] = \int dy \left\{ \frac{\Sigma \ell_0}{\alpha} \left(\frac{d\ell_0}{dy} \right)^2 + V(\ell_0, \phi) \right\} \tag{2.30}$$

Our goal in this chapter is to test the predictions of the phenomenological breather-mode theory of 3D wedge filling introduced by Romero-Enrique and Parry [125–127]. For the infinite wedge and short-ranged forces, where the binding potential is irrelevant, the interfacial phenomenology is determined by the free energies associated with the three-phase liquid-vapour-substrate lines and to the wedge bottom when the interface is either pinned at the wedge or away from it [127]. In order to test these predictions, we will resort to Ising model computer simulations. As in previous studies [9,80,81], we will consider an antisymmetric double wedge geometry with periodic boundary conditions along the wedge axis (Fig. 2.2). So, first we will generalize the analysis of the breather mode model to the double wedge geometry, obtaining an analytical expression for the magnetization PDF at *critical* and *tricritical* filling. After that, we will perform Ising model simulations to check our theoretical predictions.

2.2 Phenomenological theory of filling on a double wedge

We start with the effective pseudo-one-dimensional wedge Hamiltonian which accounts only for such breather-mode excitations in a double wedge geometry

$$\mathcal{H}_W[\ell] = \int dy \left\{ \frac{\Lambda(\ell)}{2} \left(\frac{d\ell}{dy} \right)^2 + V_W(\ell) \right\} \tag{2.31}$$

where $\ell(y) > 0$ is the local height of the interface above the wedge bottom. Because we have a finite value of L, the effective bending term $\Lambda(\ell)$ resisting fluctuations along the wedge can be described by different expressions depending if the interface cross the middle of the double wedge with different

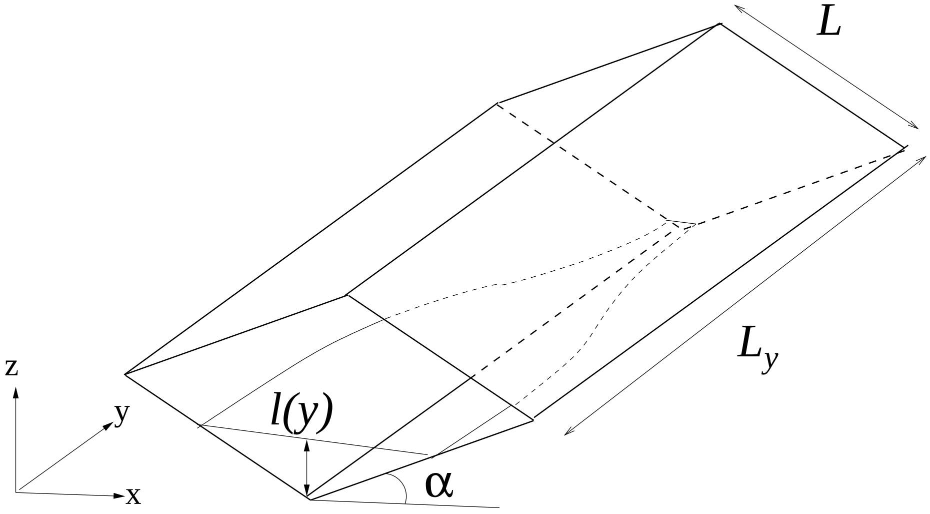

Figure 2.2: Schematic illustration of a typical interfacial configuration for fluid adsorption in a 3D double wedge.

surface fields applied in each wedge,

$$\Lambda(\ell) = \begin{cases} \frac{2\Sigma\ell}{\tan\alpha} & 0 < \ell < L\sin\alpha \\ \\ \frac{2\Sigma(2L\sin\alpha - \ell)}{\tan\alpha} & L\sin\alpha < \ell < 2L\sin\alpha \end{cases} \tag{2.32}$$

where Σ is the interfacial tension (more properly the stiffness for lattice models), $L\sin(\alpha)$ is the value of ℓ at the middle of the double wedge and $2L\sin\alpha$ the maximum height. Similarly the effective wedge binding potential $V_W(\ell)$ at the gas-liquid coexistence takes the two forms

$$V_W(\ell) = \begin{cases} \frac{2\Sigma(\cos\alpha - \cos\theta)\ell}{\sin\alpha} & 0 < \ell < L\sin\alpha \\ \\ \frac{2\Sigma(\cos\alpha - \cos\theta)(2L\sin\alpha - \ell)}{\sin\alpha} & L\sin\alpha < \ell < 2L\sin\alpha \end{cases} \tag{2.33}$$

where θ is the contact angle of a liquid drop at the planar wall-vapour interface. This potential takes into account the thermodynamic cost of forming a filled region. At the filling transition, $\theta = \alpha$ and V_W vanishes. The effect of the short-ranged forces, appropriated for the Ising model, can be modelled as contact potentials with equal strengths U at the wedge top $\ell = 2L\sin\alpha$ and bottom $\ell = 0$.

The partition function of the system can be expressed in terms of a path integral [20]:

$$Z(\ell_a, \ell_b, L_y) = \int \mathcal{D}\ell \ \exp(-\mathcal{H}_W[\ell]) \tag{2.34}$$

where we set $k_BT = 1$ for convenience and ℓ_a and ℓ_b are the (fixed) values of the interfacial height at the end points a and b, separated a distance L_y along the wedge axis. However, the presence of a position-dependent stiffness coefficient makes the definition of the partition function ambiguous, so some care must to be taken because it is of crucial importance for the evaluation of the exponents at filling transition. This problem was already pointed out, but not satisfactorily resolved, in Ref. [6] and it is intimately related to issues associated with the canonical quantization of classical systems with a position-dependent mass [29, 144]. Borrowing from the methods used to overcome these difficulties and following the previous papers [125–127], we use the following definition:

$$Z(\ell_a, \ell_b, L_y) = \lim_{N\to\infty} \int d\ell_1 \dots d\ell_{N-1} \prod_{j=1}^{N} K(\ell_j, \ell_{j-1}, L_y/N) \tag{2.35}$$

where $\ell_0 \equiv \ell_a$ and $\ell_N \equiv \ell_b$, and $K(\ell, \ell', y)$ is defined as:

$$K(\ell, \ell', y) = \frac{(\Lambda(\ell)\Lambda(\ell'))^{1/4}}{\sqrt{2\pi y}} \exp\left(-\frac{\sqrt{\Lambda(\ell)\Lambda(\ell')}}{2y} (\ell - \ell')^2 - yV_W(\ell') \right) \tag{2.36}$$

We will show that the partition function $Z(\ell_a, \ell_b, L_y)$ verifies the differential equation:

$$H_W Z(\ell_a, \ell_b, L_y) = -\frac{\partial Z(\ell_a, \ell_b, L_y)}{\partial L_y} \tag{2.37}$$

with the initial condition $Z(\ell_a, \ell_b, L_y) \to \delta(\ell_b - \ell_a)$ as $L_y \to 0$. To derive this equation we can make use of the definition of the derivative and the propagator relation [20, 29, 39]:

$$\begin{aligned} Z(\ell_a, \ell_b, L_y + \epsilon) &= \int_{-\infty}^{\infty} d\ell_c \, Z(\ell_a, \ell_c, L_y) \, K(\ell_c, \ell_b, \epsilon) \\ &\approx Z(\ell_a, \ell_b, L_y) + \epsilon \frac{\partial Z(\ell_a, \ell_b, L_y)}{\partial L_y} \end{aligned} \tag{2.38}$$

To compare the two expressions, we have to obtain the value of the integral in terms of Z and its ℓ-derivatives for small ϵ. From Eq. (2.36) we see that the kernel $K(l_c, l_b, \epsilon)$ displays non-negligible values if $(l_b - l_c)^2/\epsilon$ is of order of unity (see the exponential term). So, we can assume that $|l_b - l_c| \sim \sqrt{\epsilon}$.

Since ϵ is small we can expand the kernel in powers of ϵ and $\ell_c - \ell_b$ as:

$$\begin{aligned} K(\ell_c, \ell_b, \epsilon) &= \sqrt{\frac{\Lambda(\ell_b)}{2\pi\epsilon}} \exp\left(-\frac{\Lambda(\ell_b)}{2\epsilon}(\ell_c-\ell_b)^2\right)\Bigg[1 + \frac{\Lambda'(\ell_b)}{4\Lambda(\ell_b)}(\ell_c-\ell_b) \\ &- \frac{\Lambda'(\ell_b)}{4\epsilon}(\ell_c-\ell_b)^3 - \epsilon V_W(\ell_b) \\ &+ \frac{1}{8}\left[\frac{\Lambda''(\ell_b)}{\Lambda(\ell_b)} - \frac{3}{4}\left(\frac{\Lambda'(\ell_b)}{\Lambda(\ell_b)}\right)^2\right](\ell_c-\ell_b)^2 \\ &- \frac{\Lambda''(\ell_b)}{8\epsilon}(\ell_c-\ell_b)^4 + \frac{(\Lambda'(\ell_b))^2}{32\epsilon^2}(\ell_c-\ell_b)^6\Bigg] + \mathcal{O}(\epsilon^{3/2}) \end{aligned} \tag{2.39}$$

where the prime denotes the derivative with respect to its argument. Finally, since $|\ell_c - \ell_b|$ is small, we can expand Z as

$$\begin{aligned} Z(\ell_a, \ell_c, L_y) &\approx Z(\ell_a, \ell_b, L_y) + \frac{\partial Z(\ell_a, \ell_b, L_y)}{\partial \ell_b}(\ell_c-\ell_b) \\ &+ \frac{1}{2}\frac{\partial^2 Z(\ell_a, \ell_b, L_y)}{\partial \ell_b^2}(\ell_c-\ell_b)^2 \end{aligned} \tag{2.40}$$

By substituting Eqs. (2.39) and (2.40) into Eq. (2.38), integration is reduced to evaluate the moments of a Gaussian distribution on ℓ_c, with mean value ℓ_b and standard deviation $\sqrt{\epsilon/\Lambda(\ell_b)}$. So, up to order ϵ, the integral will have the expression

$$\begin{aligned} Z(\ell_a, \ell_b, L_y+\epsilon) &= Z(\ell_a, \ell_c, L_y)\left\{1 - \left(V_W(\ell_b) + \frac{1}{4}\frac{\Lambda''(\ell_b)}{\Lambda(\ell_b)^2} - \frac{3}{8}\frac{\Lambda'(\ell_b)^2}{\Lambda(\ell_b)^3}\right)\epsilon\right\} \\ &- \frac{\partial Z}{\partial \ell_b}\frac{\Lambda'(\ell_b)}{2\Lambda(\ell_b)^2}\epsilon + \frac{1}{2}\frac{\partial^2 Z}{\partial \ell_b^2}\frac{1}{\Lambda(\ell_b)}\epsilon \end{aligned} \tag{2.41}$$

Comparing the two expressions of $Z(\ell_a, \ell_b, L_y + \epsilon)$ in equation (2.38), we can identify the operator H_W as

$$H_W \equiv -\frac{1}{2}\frac{\partial}{\partial \ell_b}\left[\frac{1}{\Lambda(\ell_b)}\frac{\partial}{\partial \ell_b}\right] + V_W(\ell_b) + \tilde{V}_W(\ell_b) \tag{2.42}$$

where $\tilde{V}_W(\ell)$ is given by

$$\tilde{V}_W(\ell_b) = -\frac{1}{2\Lambda(\ell_b)}\left[\frac{3}{4}\left(\frac{\Lambda'(\ell_b)}{\Lambda(\ell_b)}\right)^2 - \frac{\Lambda''(\ell_b)}{2\Lambda(\ell_b)}\right] \tag{2.43}$$

verifying the differential equation (2.37). The partition function $Z(\ell_a, \ell_b, L_y)$ corresponds to fixed boundary conditions at $y = 0$ and $y = L_y$. However, the partition function for periodic boundary conditions $Z_{periodic}$ can be obtained from Z as:

$$Z_{periodic}(L, L_y) = \int_0^{2L\sin\alpha} Z(\ell, \ell, L_y) d\ell \tag{2.44}$$

As in the case of the infinite wedge, the partition function $Z_{periodic}$ may be expressed in terms of the eigenvalues E_α and eigenfunctions ψ_α of the Schrödinger-like operator H_W as:

$$Z_{periodic} = \sum_\alpha \int_0^{2L\sin\alpha} |\psi_\alpha(\ell)|^2 d\ell e^{-E_\alpha L_y} = \sum_\alpha e^{-E_\alpha L_y} \tag{2.45}$$

where the normalization condition on ψ_α was taken into account. On the other hand, the interfacial height PDF can be obtained as:

$$P_W(\ell, L, L_y) = \frac{Z(\ell, \ell, L_y)}{Z_{periodic}(L, L_y)} = \frac{\sum_\alpha |\psi_\alpha(\ell)|^2 e^{-E_\alpha L_y}}{\sum_\alpha e^{-E_\alpha L_y}} \tag{2.46}$$

In order to proceed, we now need to solve the eigenvalue problem $H_W \psi(\ell) = E\psi(\ell)$ and determine the spectrum. As the operator H_W is symmetric with respect to $\ell = L\sin\alpha$, the corresponding eigenfunctions will be either symmetric or antisymmetric. Consequently we only need to solve the eigenvalue problem in the interval $0 < \ell < L\sin\alpha$ and impose the appropriate symmetry at the mid-point.

In order to solve the eigenvalue problem, we have to introduce the appropriate boundary conditions at $\ell = 0$ and $\ell = L\sin\alpha$. For the boundary condition at the origin, we note that analysis of the Schrödinger-like operator H_W shows that the short-distance behaviour of the eigenfunctions is determined by the effective potential $\tilde{V}_W(\ell) = -3\tan\alpha/(16\Sigma\ell^3)$. So, we will first consider the infinite wedge case and $\theta = \alpha$ in order to get the boundary condition. Following previous studies about the eigenfunctions on the infinite wedge, the solutions of the eingenvalue problem have the following form [125, 127, 130]:

$$\psi(\ell) = \ell K_{1/3}\left(\sqrt{2\,E\,A}\,\frac{\ell^{3/2}}{3/2}\right) = \sqrt{\ell}\,A_i\left((-2\,E\,A)^{1/3}\,\ell\right) \tag{2.47}$$

where $K_\nu(x)$ is the modified Bessel function, $\mathrm{Ai}(x)$ is Airy function and $A = 2\Sigma/\tan\alpha$. The behaviour at $\ell = 0$ can be characterized by regularization procedure introducing a square well contact potential, with constant strength $-U$ and width ξ_0 and a constant value of the effective bending term $\Lambda_0 =$

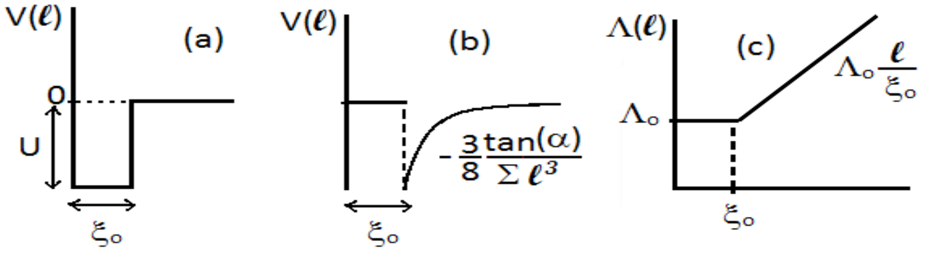

Figure 2.3: Schematic illustration of the regularization procedure. We introduce a square well-like contact potential (a) with constant strength $-U$ with a width ξ_0. On the other hand, the effective potential $\tilde{V}_W(\ell) = -3\tan\alpha/(16\Sigma\ell^3)$ vanishes for $\ell < \xi_0$ (b). Finally, the position-dependent stiffness is modified to be a constant for $\ell < \xi_0$ (c).

$2\Sigma\cot\alpha\xi_0$ for $\ell < \xi_0$ (see Fig. 2.3). The boundary condition at $\ell = 0$ is $\psi(0) = 0$. So, the eigenfunctions of the regularized problem are

$$\psi(\ell) = \begin{cases} \mathcal{A}\sin\left(\sqrt{2\Lambda_0\left(U - |E|\right)}\,\ell\right) & \ell < \xi_0 \\ \\ \mathcal{B}\sqrt{\ell}\,A_i\Big(\left(-2\,E\,A\right)^{1/3}\ell\Big) & \ell > \xi_0 \end{cases} \tag{2.48}$$

Continuity of $\tilde{V}_W(\ell)$ and $\Lambda(\ell)$ implies the continuity of $\psi(\ell)$ at ξ_0:

$$\psi(\xi_0^-) \;=\; \psi(\xi_0^+) \tag{2.49}$$

On the other hand, integration of the Schrödinger-like equation between $\xi_0 - \eta$ and $\xi_0 + \eta$ for small η shows that the eigenfunctions display a discontinuity on their derivatives due to the Dirac-delta singularity of the regularized position-dependent stiffness[1]

$$\left.\frac{d\psi(\ell)}{d\ell}\right|_{\ell=\xi_0^+} = \left.\frac{d\psi(\ell)}{d\ell}\right|_{\ell=\xi_0^-} - \frac{\psi(\xi_0)}{2\xi_0} \tag{2.50}$$

Combining Eqs. (2.49) and (2.50), we get the boundary condition:

$$\sqrt{u-\epsilon}\ \cot\left(\sqrt{u-\epsilon}\right) = \epsilon^{1/3}\frac{\mathrm{Ai}'\left(\epsilon^{1/3}\right)}{\mathrm{Ai}\left(\epsilon^{1/3}\right)} \tag{2.51}$$

where $u = 2\Lambda_0 U\xi_0^2$ and $\epsilon = 2\Lambda_0|E|\xi_0^2$. If u is small, there are no solutions to Eq. (2.51). The first solution occurs for $\epsilon = 0$, so we can identify u_{tc} as the first-zero of the function $\sqrt{u}\cot\sqrt{u}$, i.e. $u_{tc} = (\pi/2)^2 \approx 2.467$. We expand Eq. (2.51) for small ϵ and $u - u_{tc}$, leading to the following expression:

$$-\frac{1}{2}(u-u_{tc}) = \frac{\Gamma[-1/3]3^{-2/3}}{\Gamma[1/3]}\epsilon^{1/3} \tag{2.52}$$

We define the characteristic length x_u as

$$\xi_u = 2\xi_0\frac{\Gamma[-1/3]3^{-2/3}}{\Gamma[1/3]}|u-u_{tc}|^{-1} \tag{2.53}$$

which diverges as $u \to u_{tc}$. So, for $u < u_{tc}$, $-\epsilon = (\xi_0/\xi_u)^3 \sim \xi_y^{-1}$, and consequently there is a divergence of the wedge correlation length as $u \to u_{tc}$. This indicates that u is a relevant operator in the renormalization-group sense, and that $u = u_{tc}$ corresponds to a tricritical point [125, 127]. For finite L, we still can use this regularization technique, but the eigenfunction for $\ell > \xi_0$ is no longer given by Eq. (2.47), although $\psi \sim \sqrt{\ell}$ for small ℓ. Nevertheless, we can proceed in an analogous way, so Eq. (2.51) is generalized by

$$\lim_{\ell\to 0^+}\frac{\sqrt{\ell}}{\psi(\ell)}\frac{d(\psi(\ell)/\sqrt{\ell})}{d\ell} = \pm\frac{\Gamma[-1/3]3^{-2/3}}{\Gamma[1/3]}\xi_u^{-1} \tag{2.54}$$

where the positive and negative signs corresponds to $U > U_{tc}$ (first-order filling) and $U < U_{tc}$ (critical filling), respectively [127]. The situation $U = U_{tc}$ corresponds to the tricritical point. So, owing to this boundary condition, the eigenfunctions exhibit the next short-distance expansion [127]:

---

[1] This condition differs from the considered in Refs. [125,127,130], where the singularity at $\ell = \xi_0$ of the regularized effective bending term was not taken into account. We will see, however, that this missing factor only changes the tricritical value of u and the proportionality constant between ξ_u and ΔU. Once the correct values of these quantities is taken into account, the analysis of the problem reported in these references is still correct.

$$\psi(\ell) \sim \sqrt{\ell} \pm \frac{\Gamma[-1/3]3^{-2/3}}{\Gamma[1/3]}\frac{\ell^{3/2}}{\xi_u} \tag{2.55}$$

For critical filling, $\xi_u \to 0$, so $\psi(\ell) \sim \ell^{3/2}$ and consequently $P_W(\ell) \sim \ell^3$, which dictate that the local density at the wedge is non-singular. On the other hand, for tricritical filling, $\xi_u \to \infty$, so $\psi(\ell) \sim \ell^{1/2}$, and $P_W(\ell) \sim \ell$.

At the mid-point height $\ell = L\sin\alpha$, we have to take into account that $\Lambda(\ell)$ given by Eq. (2.32) has a cusp singularity so that $\Lambda'(\ell) = \mp 2\Sigma/\sin\alpha$ as $\ell \to (L\sin\alpha)^{\pm}$. Equivalently there is Dirac delta contribution to $\Lambda''(\ell)$. Consequently, we can integrate the eigenvalue equation between $\ell = (L\sin\alpha)^-$ and $\ell = (L\sin\alpha)^+$, and obtain

$$\left.\frac{\partial\psi}{\partial\ell}\right|_{\ell=(L\sin\alpha)^+} - \left.\frac{\partial\psi}{\partial\ell}\right|_{\ell=(L\sin\alpha)^-} + \frac{\psi(L\sin\alpha)}{L\sin\alpha} = 0 \tag{2.56}$$

We are now in a position to use the symmetry properties of the eigenfunctions. For odd eigenfunctions, $(\partial\psi/\partial\ell)$ at $\ell = (L\sin\alpha)^+$ is equal to $(\partial\psi/\partial\ell)$ at $\ell = (L\sin\alpha)^-$. Consequently (2.56) reduces to $\psi(L\sin\alpha) = 0$. On the other hand, for even eigenfunctions, $(\partial\psi/\partial\ell)$ at $\ell = (L\sin\alpha)^+$ is equal to $-(\partial\psi/\partial\ell)$ at $\ell = (L\sin\alpha)^-$, in which case the boundary condition at $\ell = L\sin\alpha$ simplifies to:

$$\left.\frac{\partial\psi}{\partial\ell}\right|_{\ell=(L\sin\alpha)^-} = \frac{\psi(L\sin\alpha)}{2L\sin\alpha} \tag{2.57}$$

Exactly at the filling transition, $\theta = \alpha$, for $\ell < L\sin\alpha$ the eigenfunctions take the form

$$\psi(\ell) \propto \sqrt{\ell}\left[\mathrm{Ai}\left(\epsilon^{1/3}\ell\right) + C\ \mathrm{Bi}\left(\epsilon^{1/3}\ell\right)\right] \tag{2.58}$$

where $\mathrm{Ai}(x)$ and $\mathrm{Bi}(x)$ are Airy functions, and the reduced eigenvalue $\epsilon = -4\Sigma E/\tan\alpha$. The constant C and the reduced eigenvalues are obtained from the boundary conditions Eqs. (2.54) and (2.56). In particular, the boundary condition Eq. (2.54) reduces to:

$$\pm\xi_u^{-1} = \epsilon^{1/3}\frac{\frac{1}{\sqrt{3}} - C}{\frac{1}{\sqrt{3}} + C} \tag{2.59}$$

For the critical situation, this condition reduces to $C = -1/\sqrt{3}$, and $C = 1/\sqrt{3}$ for the tricritical point. Application of the boundary condition Eq.

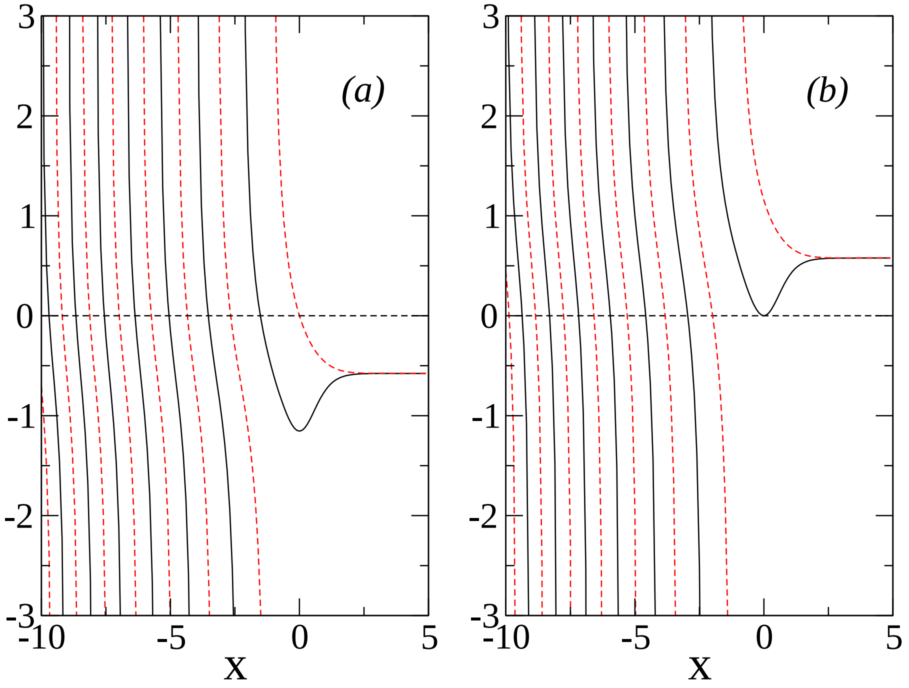

Figure 2.4: Graphical solution of the Eq. (2.60) for the critical (a) and tricritical (b) cases. The continuous line corresponds to the function $\mathrm{Ai}'(x)/\mathrm{Bi}'(x)+C$, and the dashed line one to $\mathrm{Ai}(x)/\mathrm{Bi}(x)+C$. The values of x_i are the zeroes of these functions.

(2.56) then leads to the following relationships for the values of $x \equiv \epsilon^{1/3} L \sin\alpha$:

$$-C \;=\begin{cases} \frac{\mathrm{Ai}'(x)}{\mathrm{Bi}'(x)} & \psi(\ell) \text{ even} \\ \\ \frac{\mathrm{Ai}(x)}{\mathrm{Bi}(x)} & \psi(\ell) \text{ odd} \end{cases} \tag{2.60}$$

These equations can be solved numerically or graphically (see Fig. 2.4), leading to an infinite series of solutions at x_i, with $i = 0, 1, 2, \ldots$. Table 2.1 shows the values corresponding to the first few solutions. The corresponding eigenvalues E_i can be expressed as $E_i = -\tan\alpha x_i^3/4\Sigma(L\sin\alpha)^3$. We see that the ground state corresponds to an even eigenfunction, and that the parity of the eigenfunctions, ordered by the eigenvalue, is alternating even and odd. It follows that the PDF for the interfacial height in the region $0 < \ell < L\sin\alpha$

Table 2.1: First solutions of Eq. (2.60).

i	$x_i(critical)$	$x_i(tricritical)$	Eigenfunction parity
0	-1.5149	0.0000	Even
1	-2.6664	-1.9864	Odd
2	-3.5341	-2.9488	Even
3	-4.3425	-3.8253	Odd
4	-5.0562	-4.5781	Even
5	-5.7410	-5.2956	Odd
6	-6.3726	-5.9503	Even
7	-6.9861	-6.5843	Odd
8	-7.5639	-7.1779	Even

is given by

$$P_W(\ell, L, L_y) = \frac{\displaystyle\sum_{i=0}^{\infty} N_i \ell \left[\text{Ai}\left(\frac{-x_i \ell}{L\sin\alpha}\right) + C\ \text{Bi}\left(\frac{-x_i \ell}{L\sin\alpha}\right)\right]^2 e^{\kappa x_i^3}}{\displaystyle\sum_{i=0}^{\infty} e^{\kappa x_i^3}} \tag{2.61}$$

where N_i are the normalization factors of the eigenfunctions and the factor $\kappa = (\tan\alpha / 4\Sigma \sin^3\alpha)(L_y/L^3)$. Note that the PDF exactly at critical filling (as well as at tricritical filling) does not depend on L and L_y independently, but via the scaling combination L_y/L^3, i.e. $P_W(\ell, L, L_y) = P_W(\ell, L_y/L^3)$, in agreement with the assumptions of previous scaling arguments [9, 80, 81].

In order to compare these predictions with the existing Ising model computer simulation results, we must convert the dependence on the interfacial height into an appropriate microscopic observable. For Ising model this is the local magnetization density m in the vertical plane at position y along the wedge. In the breather-mode picture this change of variables is straightforward [5]. In the case of the double wedge we can write

$$\frac{m}{m_b} = \begin{cases} \left(\frac{\ell}{L\sin\alpha}\right)^2 - 1 & ; 0 < \ell < L\sin\alpha \\ \\ 1 - \left(\frac{2L\sin\alpha - \ell}{L\sin\alpha}\right)^2 & ; L\sin\alpha < \ell < 2L\sin\alpha \end{cases} \tag{2.62}$$

where $m_b > 0$ is the bulk magnetization. That is, in standard lattice-gas language, the bulk "liquid" phase has an associated magnetization density $+m_b$, while for the bulk "gas" the magnetization density is $-m_b$. The magnetization PDF is then related to the interfacial height PDF via $P_W(m) =$

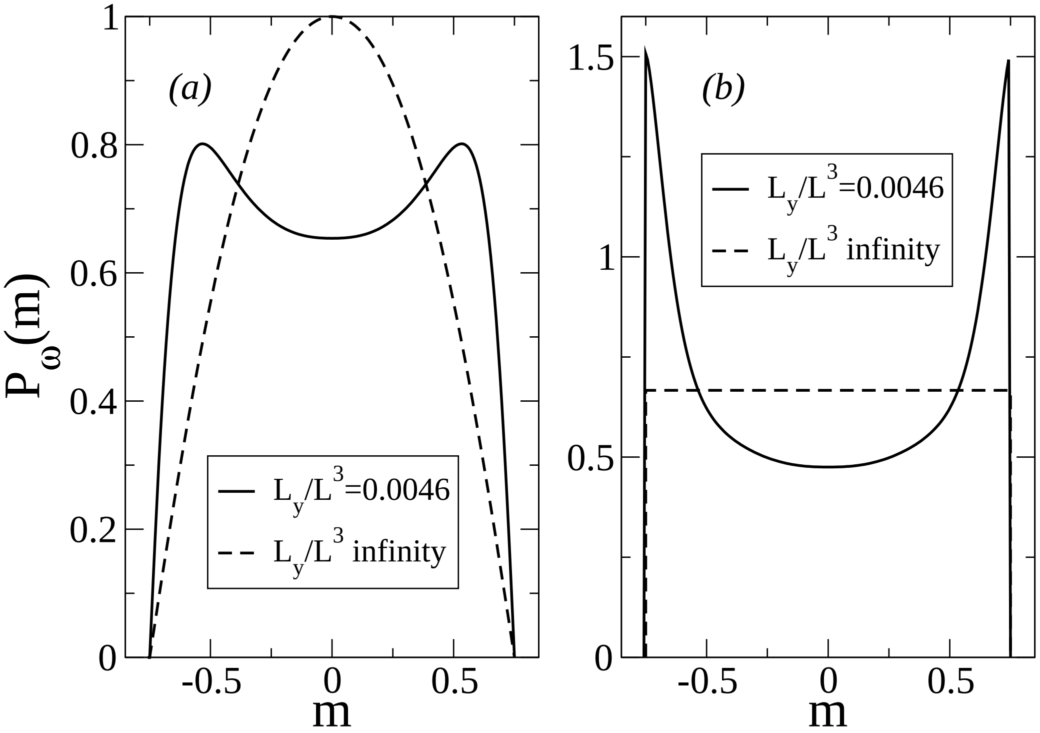

Figure 2.5: Magnetization PDFs at the critical (a) and tricritical (b) filling transition obtained from the phenomenological theory. The parameters considered are $\alpha = \pi/4$, $\Sigma = 0.0981$ and $m_b = 0.75$ to mimic the existing Ising model studies [80,81]. The continuous curve corresponds to $L_y/L^3 = 0.0046$, and the dashed line to $L_y/L^3 \to \infty$.

$P_W(\ell(m))|d\ell/dm|$. Thus the magnetization PDF exactly at critical and tricritical filling transitions is given by

$$P_w(m, L_y/L^3) = \frac{\displaystyle\sum_{i=0}^{\infty} \frac{\tilde{\psi}^2(m)}{\int_{-m_b}^{+m_b} dm \tilde{\psi}^2(m)} e^{\kappa x_i^3}}{\displaystyle\sum_{i=0}^{\infty} e^{\kappa x_i^3}} \qquad (2.63)$$

where κ and x_i are defined as above, and the functions $\tilde{\psi}_i(m)$ are given by:

$$\tilde{\psi}_i(m) = \mathrm{Ai}\left(-x_i\sqrt{1 - \frac{|m|}{m_b}}\right) + C\ \mathrm{Bi}\left(-x_i\sqrt{1 - \frac{|m|}{m_b}}\right) \qquad (2.64)$$

Fig. 2.5 shows the magnetization PDF predicted by this phenomenological theory. For critical filling, when $L_y \to \infty$, the PDF es unimodal, corresponding to the situation $P_w(m) = \tilde{\psi}^2(m)$. As L_y decreases, the magnetization PDF becomes bimodal, where the most probable magnetization density in each section depends on the value of the scaling variable L_y/L^3, but the absolute value is always smaller than m_b. However, for tricritical filling when $L_y/L^3 = 0$, the magnetization PDF over the interval $[-m_b, m_b]$ is flat, and as L_y/L^3 increases, the magnetization PDF becomes bimodal like critical filling, but the most probable magnetization density in each section correspond exactly to $m = \pm m_b$.

2.3 Double wedge Ising model simulations

In order to check de the prediction of the phenomenological theory of the double wedge and to confirm the predicted existence of a tricritical filling transition, we performed Monte Carlo simulations of the Ising model. In particular, we revisit the Ising model simulations in the double-wedge geometry considered by Milchev *et al.* [9, 80, 81] with some modifications.

The study of critical phenomena by computer simulations is a challenging task, as they show large fluctuations close to the transitions, while simulations always involve finite systems. So, while standard techniques usually work well for large enough systems (i.e. when the simulation box sizes are larger than the relevant correlation length), they fail close to critical phenomena since the correlation length can be arbitrarily large. As a consequence, the behaviour of the different measured quantities will present a finite-size dependence. The finite-size techniques [110] take advantange of this dependence, so information on the phase transition onset and critical exponents can be found. Two assumptions are usually taken into account: that scaling is obeyed close to the critical transition, and that the dependence on the correlation length is substituted by the box simulation size when the former exceeds the latter.

We consider Monte Carlo simulations for a nearest neighbor Ising model (isomorphic to a lattice gas) on a simple cubic lattice with linear dimensions $L \times L \times L_y$ in lattice spacing units. Periodic boundary conditions are applied along the y direction, and in the remaining boundaries free boundary conditions are applied. We set similar bulk conditions as those previously considered for the critical filling characterization. So, the Hamiltonian of the Ising model is given by Eq. (2.65). As in earlier works, we choose $\beta J \equiv J/k_B T = 1/4$ and the surface exchange constant $J_s = J/2$. Under these conditions, the simulation box is a double wedge characterized by a tilt angle $\alpha = \pi/4$, the bulk magnetization is $m_b \approx 0.75$, and $\Sigma = \beta\sigma a^2 \approx 0.0981$, with σ being the interfacial tension of the Ising model and a the lattice spacing [81]. We define W_1 and W_2 as the two neighbouring $L \times L_y$ free surfaces which meet at each wedge (see Fig. 2.6). Focussing on W_1, the surface field H_s is applied in a set of sites W_1' of W_1 which are away from the wedge, and a line field h_l on the remaining sites. For the antisymmetric setup, opposite fields $-H_s$ and $-h_l$ are applied on W_2' and $W_2 - W_2'$, respectively, where the set W_2' is the mirror image of W_1' with respect to the diagonal symmetry plane of the simulation box. We have some freedom to define the set of sites where the line field h_l is applied. We impose as a condition that the sites must be at or very close to the wedge, so H_s is applied on most of the sites of the free surfaces. Thus the stripped regions of microscopic width where h_l acts reduce to the wedge axes for large L. The value of H_s determines the contact angle, and for a flat substrate the wetting transition is critical [12]. On the other hand, the introduction of h_l alters the value of the pinning potential in such a way that, if h_l and H_s are of opposite sign, opposite magnetizations on sites close to the wedge are favoured, and this fact may eventually induce the interfacial pinning at the wedges. In the present work, we consider that the line field h_l acts on the sites which are along the wedge and their nearest-neighbours (Fig.2.6).

$$\begin{aligned}\beta H &= -\frac{1}{4}\sum_{\langle i,j\rangle_{bulk}} S_i S_j - \frac{1}{8}\sum_{\langle i,j\rangle \in W_1 \cup W_2} S_i S_j - \beta H_s \sum_{i\in W_1'} S_i + \beta H_s \sum_{i \in W_2'} S_i \\ &- \beta h_l \sum_{i \in W_1 - W_1'} S_i + \beta h_l \sum_{i\in W_2 - W_2'} S_i \qquad (2.65)\end{aligned}$$

These Monte Carlo simulations were performed by using the standard Metropolis algorithm [79]. The quantities we are interested in equilibrate quite slowly, so we considered runs of order of 10^8 sweeps, where a sweep is $L^2 \times L_y$ attempted updates of a spin chosen at random.

In addition to the usual quantities such as the energy or total magnetization, during the simulation we also evaluated the magnetization PDF. The magnetization associated with the L^2 spins in each slice perpendicular to the y direction, which we will denote as $\tilde{R}_j$, where $j = 1, \cdots, L_y$. In order to minimize the effect of the enhanced order of the magnetization close to the boundaries, we excluded the spins on sites which are nearest or next-to-nearest neighbours to the walls. The set of $(L-4)^2$ sites which are in $\tilde{R}_j$, but are not either nearest ot next-to-nearest neighbours to the walls will be denoted as R_j. the magnetization in each slice R_j is defined as $M(j) = \sum_{i\in R_j} S_i$, with $j = 1, \cdots, L_y$, and the corresponding magnetization density $m(j) = M(J)/(L-4)^2$. We also evaluated the surface magnetization at each slice, *i.e.* $M_S(j) = \sum_{i \in \tilde{R}_j \cap W_1} S_i - \sum_{i\in \tilde{R}_j \cap W_2} S_i$.

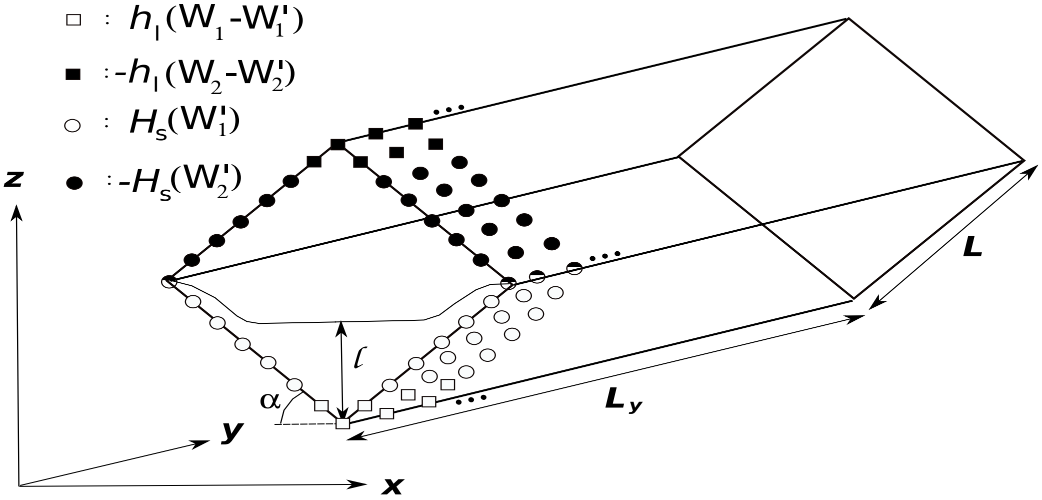

Figure 2.6: Schematic picture of the modified antisymmetric double wedge geometry of size $L \times L \times L_y$ and characterized by a tilt angle α. Filled and empty symbols refer to the spins associated with the surfaces which define the W_1 (filled) and W_2 (empty) wedges. Circles represent the sites subject to the surface fields H_s (W_1') and $-H_s$ (W_2'). Squares represent the wedge sites where act the line field h_l ($W_1 - W_1'$) and $-h_l$ ($W_2 - W_2'$).

The magnetization PDF can be obtained from the computer simulation as

$$P_W(m) = \frac{(L-4)^2}{2L_y}\left\langle \sum_{j=1}^{L_y} \delta_{M(j),(L-4)^2 m} \right\rangle \tag{2.66}$$

where $\delta_{i,j}$ is the Kronecker symbol, we have taken advantage of the translational symmetry along the y axis due to the periodic boundary conditions, and $\langle \ldots \rangle$ corresponds to the average. This quantity can be compared with the theoretical prediction from the phenomenological theory.

We also considered the joint PDF for m and M_S, which can be obtained as:

$$P_W(m, \bar{M}_s) = \frac{(L-4)^2}{4L_y}\left\langle \sum_{j=1}^{L_y} \delta_{M(j),(L-4)^2 m}\delta_{M_s(j),\bar{M}_s} \right\rangle \tag{2.67}$$

Note that $P_W(m) = 2\sum_{M_S} P_W(m, M_S) \approx \int dM_S P_W(m, M_S)$. This quantity is paticularly useful as it is possible to predict the magnetization PDF at a value of H_S which is different from the value used in the simulation by using reweighting techniques. [37, 38] If $\bar{H}_S$ is the simulation value of the surface magnetic field (the conjugate field to M_S), the joint PDF $P_W(m, M_S; \bar{H}_S)$

obtained from the simulation can be written as:

$$P_W(m, M_S; \bar{H}_S, h_l) = \frac{1}{\Xi(H_s, h_l)} \Omega(m, M_s, h_l) \exp(\beta \bar{H}_s M_s) \tag{2.68}$$

where $\Omega(m, M_s, h_l)$ is the number of microstates with slice magnetization density m and surface magnetization M_s, and $\Xi(\bar{H}_s, h_l)$ is the canonical partition function given by

$$\Xi(\bar{H}_s, h_l) = \sum_{m, M_s} \Omega(m, M_s) \exp(\beta \bar{H}_s M_s) \tag{2.69}$$

This expression is valid for any value of H_s. As $\Omega \propto P_W(\bar{H}_s) \exp(-\beta \bar{H}_s M_s)$, it is possible to estimate the joint PDF at a different surface field H_S from Eq. (2.68) in the following way:

$$P_W(m, M_s; H_s, h_l) \approx \frac{P_W(m, M_s; \bar{H}_s, h_l) e^{\beta(H_s - \bar{H}_s) M_s}}{\int dm dM_s P_W(m, M_s; \bar{H}_s, h_l) e^{\beta(H_s - \bar{H}_s) M_s}} \tag{2.70}$$

This is practical only if H_S does not differ too much from the simulation value. Note that the value of h_l remains unchanged. The values of H_s are taken to be the apparent critical filling values for each box size and $h_l = H_s$ [80, 81] (in all cases $H_s \approx 0.72$). Note that the filling transition always occurs for $\theta = \alpha$ and the value of H_s determines the value of the contact angle θ, regardless of the value of h_l. However, we have used single-histogram reweighting techniques to tune the dependence on H_s close to the filling transition of the magnetization PDF at a given value of h_l. In order to characterize finite-size effects, we perform the simulations for different system sizes, in such a way that the ratio $L_y/(L-4)^3$ is approximately constant: $19 \times 19 \times 16$, $24 \times 24 \times 37$, $34 \times 34 \times 124$ and $44 \times 44 \times 294$ (the ratio $L_y/(L-4)^3$ is approximately equal to 0.0046). Recall that the predicted critical and tricritical magnetization PDFs depend only on this size ratio. Idealy, at exactly the critical filling transition, the simulated magnetization PDF should be independent of the size, and the matching with the theoretical value would lead to the same set of magnetization moments (in particular, the Binder cumulant).

The results are shown in Fig. 2.7, confirming that under these conditions there is an excelent match with the predicted critical filling magnetization PDF from the phenomenological theory. We see that the simulated magnetization PDFs show tails for $|m| > m_b$. So, in order to achieve the aforementioned, we have to multiply the simulated PDFs by a constant factor (always around unity) in order to get good agreement. This factor will not affect the evaluation of quantities such as the Binder cumulant. In any

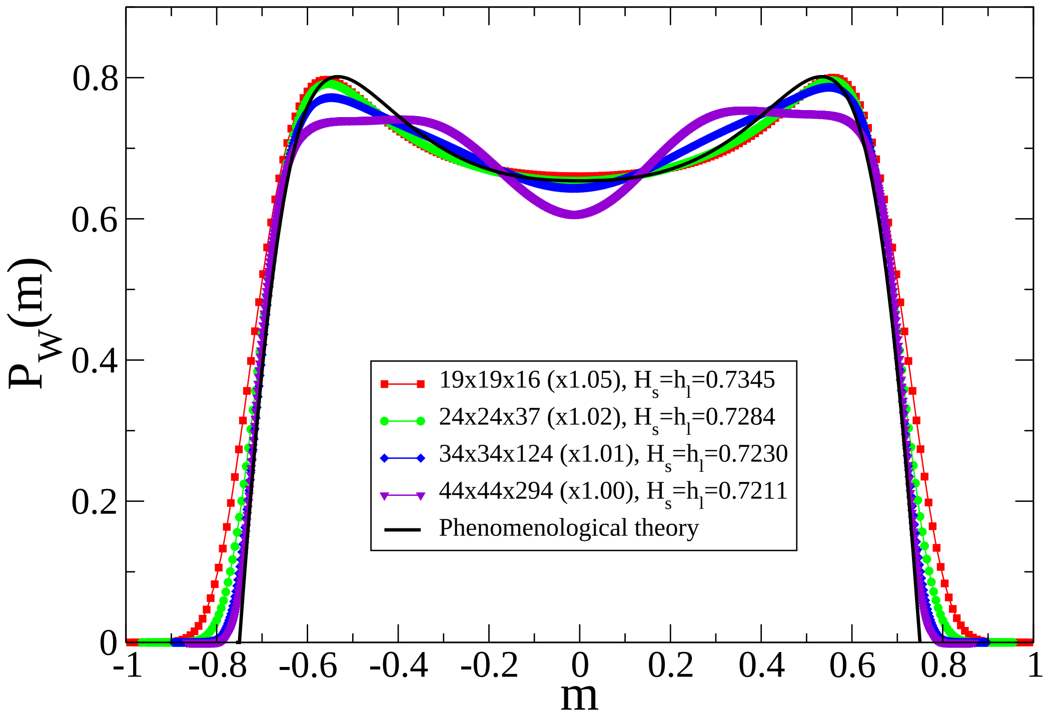

Figure 2.7: Plot of the magnetization PDFs for $h_l = H_S$ and: $H_s = 0.7345$, $19 \times 19 \times 16$ (squares); $H_s = 0.7284$, $24 \times 24 \times 37$ (circles); $H_s = 0.7230$, $34 \times 34 \times 124$ (diamonds); and $H_s = 0.7211$, $44 \times 44 \times 294$ (triangles). Under these conditions an optimal match with the theoretical prediction (wide line) is obtained. The magnetization PDF was scaled by factors 1.05, 1.02, 1.01 and 1.00, respectively.

case, the matching is reasonable for the most-probable magnetizations in the range of sizes considered. The aparent values or H_S at the transition are not exactly the same ($H_S = 0.7345$ for $L = 19$, $H_S = 0.7284$ for $L = 24$ and $H_S = 0.7230$ for $L = 34$), indicating that corrections to scaling still play a role in the location of the critical filling value of H_S.

Figure 2.8 shows typical magnetization PDFs for different values of H_s and h_l. For all values of h_l, the PDF is bimodal for values of H_s well below the filling transition value, with maxima localized approximately at $\pm m_b$. On the other hand, if H_s is well above the filling transition value, the PDF becomes unimodal with a single maximum at $m = 0$. Differences are observed when H_s is around the filling transition value. For $h_l = H_s$, we reproduce the results already presented, under these conditions, the filling transition is critical. If we set $h_l = -0.5$, a different scenario is observed. The magnetization PDFs for different box sizes do not match the theoretical critical

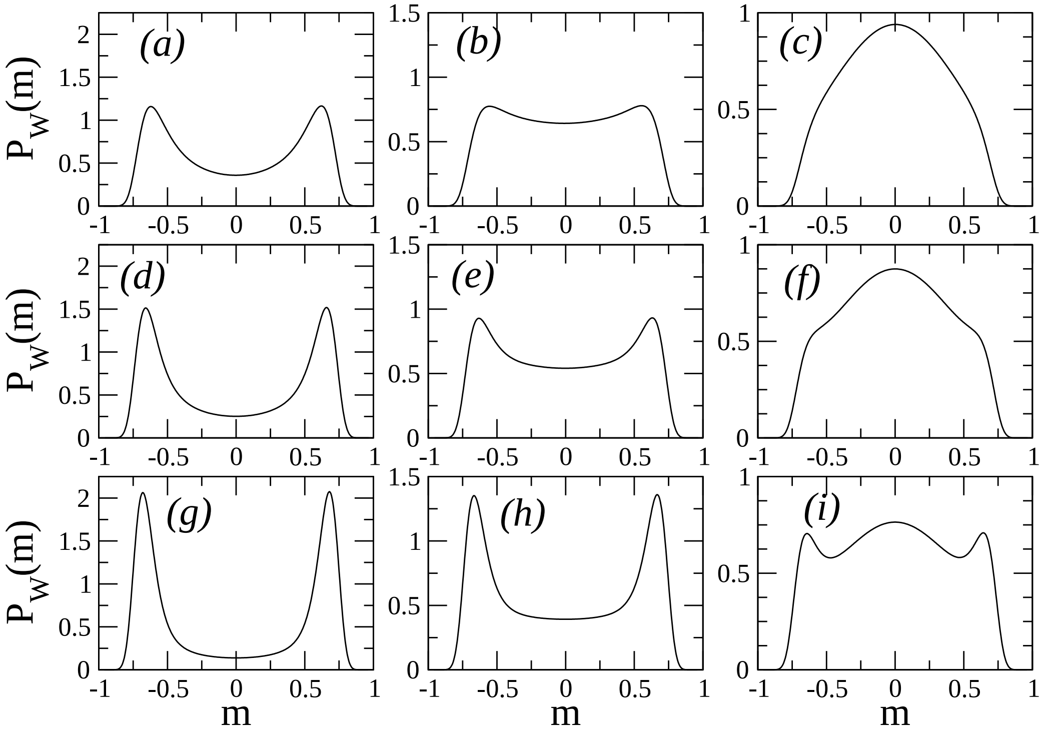

Figure 2.8: Magnetization PDFs for $L = 24$, $L_y = 37$ and different values of (H_s, h_l): (a) $(0.7084, 0.7284)$, (b) $(0.7284, 0.7284)$, (c) $(0.7484, 0.7284)$, (d) $(0.7084, 0)$, (e) $(0.7284, 0)$, (f) $(0.7484, 0)$, (g) $(0.7084, -0.5)$, (h) $(0.7284, -0.5)$, and (i) $(0.7484, -0.5)$.

filling magnetization PDF. Actually, the location of the maxima is quite insensitive to the value of H_s, and for large H_s we observe a trimodal PDF with an additional maximum at $m = 0$. By increasing H_s, the relative PDF height of the maxima at $m \approx \pm m_b$ with respect to the PDF value at $m = 0$ decreases, until the former disappear. These observations are an indication that the filling transition may be first-order for $h_l = -0.5$. The coexisting phases would be a pinned interfacial state, characterized by the bimodal PDF similar to the observed one for small H_s, and the unbound interfacial state, characterized by the unimodal PDF observed for large H_s. Near the first order transition, the magnetization PDF will be a linear superposition between the coexisting phases PDFs, where their relative weights are related to the deviation of H_s with respect to the transition value. However, our simulations show the rounding of this transition for the considered system sizes, since the PDFs of the coexisting phases overlap considerably. We explored the values of h_l between $h_l = -0.5$ and $h_l = 0.72$ to locate the borderline

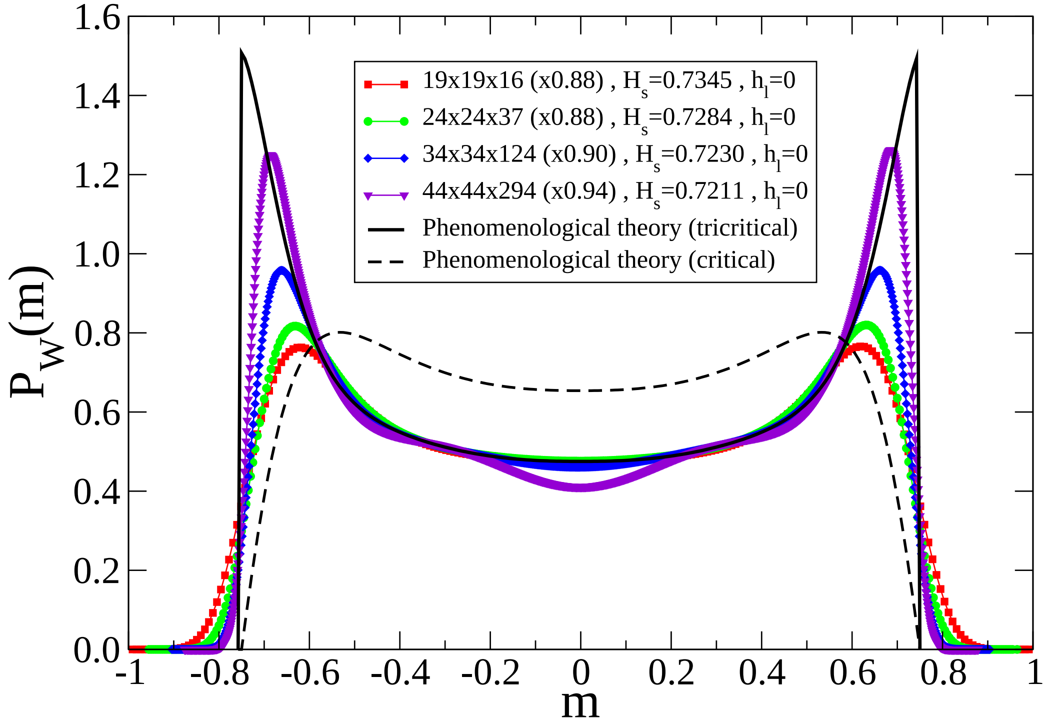

Figure 2.9: Plot of the magnetization PDFs for $h_l = 0$ and: $H_s = 0.7345$, $19 \times 19 \times 16$ (squares); $H_s = 0.7284$, $24 \times 24 \times 37$ (circles); $H_s = 0.7230$, $34 \times 34 \times 124$ (diamonds); and $H_s = 0.7211$, $44 \times 44 \times 294$ (triangles). The continuous line corresponds to the breather-mode model predicted tricritical filling PDF, and the dashed line to the predicted critical filling PDF.

between these two scenarios, that we expect to be a tricritical point from our theoretical analysis. As same as we explained before for the critical transition case,the procedure to locate the tricritical point is as follows. As the simulation PDFs show tails for large $|m|$ (due to capillary fluctuations or other irrelevant fluctuations), we match unnormalized PDFs (i.e. multiplied by an unknown factor to be determined in the matching procedure) to the theoretical expression Eq.(2.63) in a magnetization window $|m| < m_{cut}$. For our simulations, we choose $m_{cut} = 0.5$, finding the tricritical filling transition at $h_l \approx 0$. Fig. 2.9 shows the best matching magnetization PDFs for different simulation box sizes and $h_l = 0$. The values of H_s correspond approximately to the transition values for critical filling, indicating that the filling transition boundary is unaffected by the field h_l. On the other hand, the PDFs are clearly different from the critical filling PDF, and as L increases the two maxima converge to the theoretical tricritical PDF. This is the main result of this section, being a clear indication of the existence of a tricritical filling

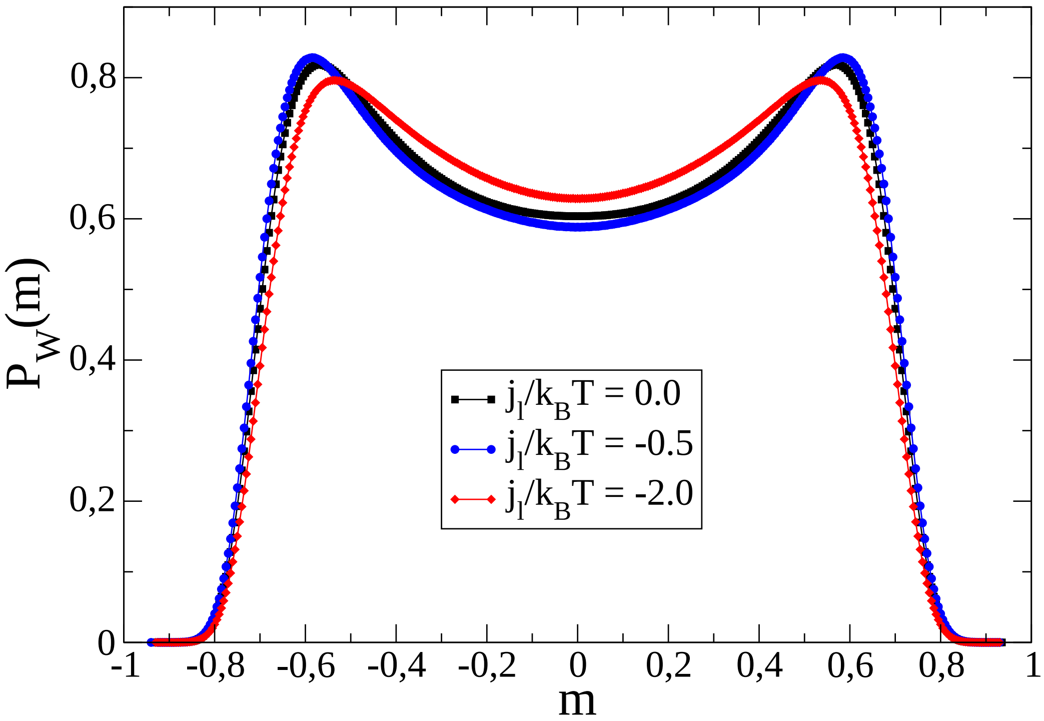

Figure 2.10: Plot of the magnetization PDFs for a double wedge 24×24×37 at critical situation H_{SC}, weakening the exchange coupling between first neighbours at the bottom and top of the double wedge, at values $j_l/K_bT = 0.0$ (squares), $j_l/K_bT = 0.5$ (circles), and $j_l/K_bT = -2.0$ (diamonds), without factor scaling. Weaker values of j_l lead to a non-ergodic behaviour.

transition.

So, h_l will contribute to the pinning contact potential, but we cannot simply identify it with the pinning potential strength, as the other coupling parameters contribute to it. The connection with the phenomenological model is now apparent. However, we do not observe tricriticality for every choice of W_1' and W_2'. For example, if h_l is applied solely on the sites along the wedge, only critical filling is observed [132]. Analogously, if we try to favour the interfacial pinning by weakening the exchange coupling of the wedge sites on the surface, the $|m|$ value of the higher peaks in the PDF shifts towards slightly higher values with respect to the critical PDF when j_l decreases (see Fig. 2.10). However, a further decrease of j_l leads to non-ergodic behaviour before the filling transition may become tricritical. In fact, the spins associated to the involved sites involved are trapped and the PDF peaks shift toward lower values of $|m|$, contrary to the phenomenological tricritical PDF.

However, returning to Fig. 2.9, it is worth noting that the magnetization PDF for the largest system seems to deviate from the theoretical prediction for small values of $|m|$. This is also observed for critical filling and we explain these discrepancies by the breakdown of the breather-mode picture for small values of $|m|$ and large L. In fact, the analysis of typical snapshots shows tilted configurations when $\ell \approx L/\sqrt{2}$, indicating that tilt and torsional modes [47] effects, of the intrinsic capillary fluctuations around the constrained profile, may be important under these conditions, specially for the critical filling. This hypothesis should be checked by considering the BTT model Eq. (2.28) with tricritical boundary condition, but a correct definition and discretization of the partition function and the infinitesimal propagator are necessary to ensure as the local density at the wedge bottom is non-singular [125–127]. We expect that the predictions may be confirmed in the future.

2.4 Summary

In this Chapter we have studied by Monte Carlo simulations the 3D wedge filling transition for the Ising model. As in previous simulation studies [9, 80, 81], we have considered a double wedge geometry with applied antisymmetric surface fields on each wedge. Our goal is to confirm earlier predictions that the filling transition may be driven first-order by the potential which binds the interface to the wedge bottom [125, 127]. In order to mimic this effect, the spin-substrate interactions are modified by introducing an additional field acting along the wedges which localizes the interface. We have found strong evidences that the filling transition can be driven first-order and the existence of the tricritical by tuning this local field. To demonstrate this, we solved exactly the breather mode model for the double wedge geometry, and we obtain the magnetization PDFs corresponding to critical and tricritical filling. A finite-size analysis of our simulations, based on the matching between the simulated magnetization PDFs and their theoretical predictions, show that two different critical behaviours for the filling transition are observed by tuning the wedge field strength. Furthermore, the simulation results show a good agreement with the predictions of the breather-mode model for the critical filling, and they converge to the theoretical values for the tricritical filling as the simulation box size increases. Finally, for very large sizes we observe some discrepancies between the theoretical and simulation results which can be a signature of other interfacial fluctuation modes such as tilt and torsional modes [47]. Although our study is restricted to the case of short-ranged forces, it may be relevant for the case of dispersive forces, since the breather-mode model predicts that the filling transition may also be driven first-order, with a critical end point as the borderline with the critical filling regime. We expect that the predictions for the latter case may be confirmed experimentally.

Chapter 3

Filling and wetting transitions on sinusoidal substrates: a mean-field study of the Landau-Ginzburg model

3.1 Introduction

Corrugation of substrates play an important role on wetting and related phenomena [120]. For example, the wetting transition temperate may be shifted or not with respect to the planar situation. On the other hand, interfacial transitions such as filling, studied for the wedge geometry in the previous Chapter, may also occur on periodically corrugated substrates with general cross section. We will study in this chapter the interfacial phenomenology of a fluid in contact with a one-dimensional array of infinitely long grooves of sinusoidal section, characterized by the periodicity length L and amplitude A. This system has been previously studied within the interfacial Hamiltonian approach for shallow substrates [114, 117, 118]. Under this approach, the free energy (in units of $k_B T$) associated to an interfacial configuration is given by:

$$\mathcal{H}[\ell] = \int dxdy \left[\frac{\Sigma}{2} \left\{ \left(\frac{\partial \ell}{\partial x} \right)^2 + \left(\frac{\partial \ell}{\partial y} \right)^2 \right\} + W_\pi(\ell - \psi(x)) \right] \tag{3.1}$$

where Σ is the interfacial stiffness, W_π is the binding potential associated to a flat substrate and $\psi(x) = A(1 - \cos qx)$. Within the mean-field approximation, we can assume that $\ell = \ell(x)$, so the Euler-Lagrange equation associated to the free energy functional is:

$$\Sigma\ddot{\ell} = W'_\pi(\ell - \psi) \tag{3.2}$$

where the dot represents the derivative with respect to x, and the prime the derivative with respect to its argument. Under this approach, both filling and wetting transitions are predicted. The filling transition is always first-order, and the wetting transition for the corrugated substrate is of the same order as for the flat substrate. When the wetting transition is first-order, the wetting transition temperature of the corrugated substrate is reduced with respect to the flat counterpart [62, 114, 120]. On the other hand, if the wetting transition is continuous, the corrugation does not shift the transition temperature [114, 117, 118]. For short-ranged forces, the binding potential reads

$$W_\pi = -\Delta T \exp(-\ell/\xi) + \exp(-2\ell/\xi) \tag{3.3}$$

where ΔT is the temperature shift with respect to the wetting transition. We will set the bulk correlation length ξ as the length unit. Then, the Euler-Lagrange equation (3.2) associated to this binding potential, after the change of variables $\eta \equiv \ell - \psi - \ell_\pi$ and $t = qx$, leads to the evolution equation of a forced inverted nonlinear oscillator

$$\frac{d^2\eta}{dt^2} = -\frac{(\Delta T)^2}{2\Sigma\beta q^2}\left(e^{-\eta} - e^{-2\eta}\right) - \frac{\bar{h}}{\Sigma q^2} + A\cos t \tag{3.4}$$

Due to the scaling properties of this equation, the filling transition occurs at a rescaled temperature $\Delta\tilde{T} \equiv \Delta T/q\sqrt{2\beta\Sigma}$ which is a function of A, but not of L [114, 117].

In this Chapter we will revisit this problem, and we will investigate the filling and wetting phenomena within the mean-field approximation (i.e. neglecting interfacial fluctuations). Unlike previous studies, the system is modelled by the Landau-Ginzburg (LG) functional (see Appendix A for a flat substrate), with fluid-substrate couplings which control the wettability of the substrate. This model has a more microscopic basis than the interfacial Hamiltonian theories, and will allow us to check the validity of the latter. Furthermore, we will be able to assess the approach to the macroscopic theory predictions, which should be valid for large L. Finally, the values of A and L we will consider in this Chapter span intermediate and large values of roughness. Minimization of the LG functional is performed by using a finite-element method which allows us to extract the order parameter profile (i.e. density in our case) and to locate the gas-liquid interface by imposing a crossing criterion on the order parameter profile. Different interfacial transitions

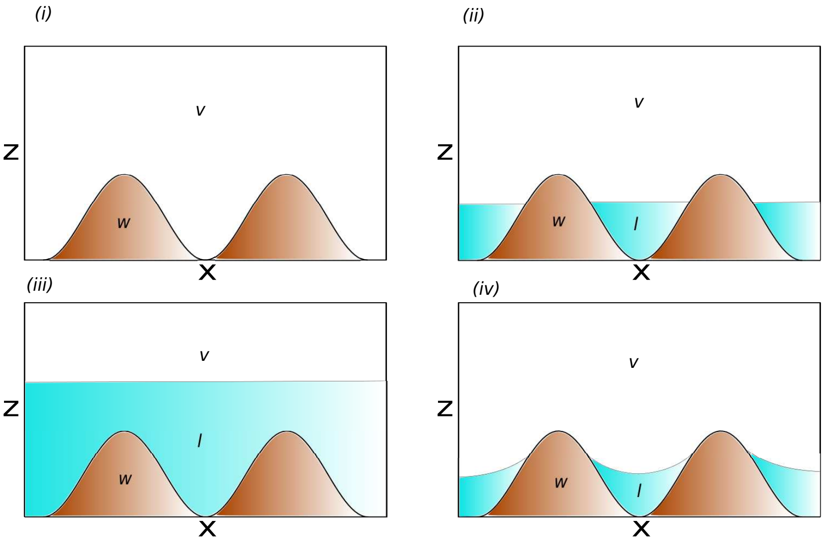

Figure 3.1: Schematic representation of interfacial states. For bulk coexistence, (i) represents the dry (D) state, (ii) represents the partially filled (F) state and (iii) corresponds to the completely wet state. In (iv) we represent the typical interfacial profile of the partially filled state out of bulk coexistence. The substrate is labelled by w, l stands for the liquid and v for the vapor.

are obtained by the crossing or merging of the free-energy branches associated to different interfacial states as the thermodynamic fields are changed. As different scenarios can be envisaged when there the wetting transition on a flat substrate is first-order or critical, two different cases have been considered to cover both choices. Finally, we also investigated the off-coexistence interfacial phenomenology.

3.2 Macroscopic theory

From a macroscopic point of view we can understand much of the phenomenology of fluid adsorption on rough substrates (a sinusoidal substrate as example). Consider a gas at saturation conditions (i.e. coexisting with a liquid) in the presence of a rough substrate, which we will consider translationally invariant along the y-direction (with a total length L_y) and periodic across the x-direction, with a period L much larger than the typical molecular lengthscales. We assume that the substrate favors nucleation of the liquid phase on its surface. The height of the substrate is given by a smooth function $\psi(x)$, which will be assumed to be an even function in its argument. There are three possible situations which the system may present [120]: the interfacial dry state (D), in which only a thin (microscopic) liquid layer is adsorbed on the substrate; the partially filled state (F), in which the substrate grooves are partially filled with liquid up to a height $h = \psi(x_c)$; and the complete wet state (W), in which a thick liquid macroscopic layer between the substrate and the vapor is formed (see figure 3.1).

To see the relative stability of these phases, we consider the excess surface free energy $\mathcal{F}$ with respect to the bulk for each state. In the macroscopic approach, we assume that interactions between the different interfaces is negligible, so the surface free energy can be obtained directly as the sum of the contributions of each surface/interface. We denote $\mathcal{S}$ as the total area of the substrate and $\mathcal{A}$ as its projection on the plane $x-y$ plane. The surface free energy of the D state, $\mathcal{F}^D$, can be obtained from the substrate surface tension between *flat* sustrate and a vapour in bulk, σ_{vw}, as:

$$\mathcal{F}^D = \mathcal{S}\sigma_{vw} \tag{3.5}$$

On the other hand, the surface free energy of the partially filled state $\mathcal{F}^F$ is given by the expression:

$$\mathcal{F}^F = S(x_c)\sigma_{lw} + (\mathcal{S} - S(x_c))\sigma_{vw} + 2\mathcal{A}\frac{x_c}{L}\sigma_{lv} \tag{3.6}$$

where σ_{lw} is the interfacial tension between the liquid and the flat substrate, σ_{lv} is the surface tension associated to the liquid-vapor interface, and $S(x_c)$ is the substrate area in contact with the liquid phase, which can be obtained from the value of $x = x_c$ at which the liquid-vapour interface is in contact with the substrate as

$$S(x_c) = \mathcal{S}\frac{\int_{-x_c}^{x_c}\sqrt{1+\psi_x^2}dx}{\int_{-L/2}^{L/2}\sqrt{1+\psi_x^2}dx} \tag{3.7}$$

where ψ_x represents the derivative of ψ with respect to x. Note that the free energy $\mathcal{F}^D$ given by (3.5) corresponds to the limit $x_c \to 0$ from (3.6). The value of x_c can be obtained from the minimization of free energy (3.6) with respect to that parameter. By Young's law, which relates the different surface tensions with the surface contact angle θ:

$$\sigma_{vw} - \sigma_{lw} = \sigma_{lv}\cos\theta \tag{3.8}$$

the free energy $\mathcal{F}^F$, (3.6) can be rewritten as:

$$\mathcal{F}^F = \mathcal{F}^D + \frac{2\mathcal{A}}{L}\sigma_{lv}\left(x_c - \cos\theta \int_0^{x_c} \sqrt{1+\psi_x^2(x)}dx\right) \tag{3.9}$$

Therefore, as the derivative of this function with respect to x must vanish at $x = x_c$, the following condition is satisfied [120]:

$$0 = (1 - \sqrt{1+\psi_x^2(x_c)}\cos\theta) = \left(1 - \frac{\cos\theta}{\cos\alpha}\right) \tag{3.10}$$

where α is the angle between the liquid-vapor interface and the substrate at the contact $x = x_c$. This result has a clear physical interpretation: the filled region by liquid should make contact with the substrate at the point where α is equal to the contact angle θ. However, this solution is only a local minimum if $(d\psi(x_c)/dx) \times (d^2\psi(x_c)/dx^2) < 0$ [120]. Finally, the interfacial free energy for the state of complete wet state $\mathcal{F}^W$ is given by:

$$\mathcal{F}^W = \mathcal{S}\sigma_{lw} + \mathcal{A}\sigma_{lv} \tag{3.11}$$

Notice that macroscopically this expression corresponds to the limit $x_c \to L/2$ of (3.6).

Several transitions between the different interfacial states may be observed. At low temperatures the most stable state is the dry state, whereas at high temperatures (i.e. above the wetting temperature of the flat substrate) the preferred state corresponds to complete wetting. Therefore, for intermediate temperatures must exist phase transitions between different interfacial states. For example, a wetting transition between D and W can occur when both states have the same free energy:

$$\mathcal{F}^W - \mathcal{F}^D = 0 = \mathcal{S}(\sigma_{lw} - \sigma_{vw}) + \mathcal{A}\sigma_{lv} \tag{3.12}$$

Using Young's law (3.8), we obtain the following condition for the wetting transition:

$$\frac{\mathcal{S}}{\mathcal{A}}\cos\theta = r\cos\theta = 1 \tag{3.13}$$

where the roughness parameter is defined as $r = \mathcal{S}/\mathcal{A}$. This is precisely the result obtained by Wenzel law [146, 147]: the contact angle of a liquid drop on a rough substrate, θ_r, is related to the contact angle of a flat substrate θ via the expression $\cos\theta_r = r\cos\theta$. Therefore, as the wetting transition occurs when $\theta_r \to 0$, we recover the expression (3.13).

It is also possible a transition from a dry state to a filled state. This transition is called in the literature either *filling* [120] or *unbending* [117] transition. The filling transition occurs when:

$$\mathcal{F}^F - \mathcal{F}^D = 0$$
$$= \frac{2\mathcal{A}}{L}\sigma_{lv}\left(x_c - \cos\theta\int_0^{x_c}\sqrt{1+\psi_x^2(x)}dx\right) \tag{3.14}$$

which leads to the expression:

$$\frac{\int_0^{x_c}\sqrt{1+\psi_x^2}dx}{x_c}\cos\theta \equiv r_c\cos\theta = 1 \tag{3.15}$$

where $r_c > 1$. If this transition occurs at temperatures below the predicted by (3.13), then Wenzel law is no longer valid. In fact, under these conditions the macroscopic theory predicts that the wetting transition will occur between an F and W state when:

$$\mathcal{F}^W - \mathcal{F}^F = 0$$
$$= (\mathcal{S} - S(x_c))(\sigma_{lw} - \sigma_{vw}) + \mathcal{A}\left(1 - \frac{2x_c}{L}\right)\sigma_{lv} \tag{3.16}$$

Now we will restrict ourselves to the sinusoidal substrate (see figure 3.1), which is characterized by an amplitude A, a wavenumber $q = 2\pi/L$, and a subtrate height $\psi(x)$ given by:

$$\psi(x) = A(1 - \cos qx) \tag{3.17}$$

For this substrate, $S(x)$ and $\mathcal{S}$ can be expressed in terms of incomplete elliptic integral of the second kind $E(qx| - (qA)^2)$ as:

$$\begin{aligned}\int_0^x \sqrt{1+\psi_u^2}du &= \int_0^x du\sqrt{1+(qA)^2\text{sen}^2 qu} \\ &= \frac{1}{q}E(qx| - (qA)^2)\end{aligned} \tag{3.18}$$

Therefore, the roughness parameters r and r_c from 3.13 and 3.15 can be expressed as:

$$r = \frac{2E(qL/2| - (qA)^2)}{qL} = \frac{2}{\pi}E(-(qA)^2) \tag{3.19}$$

$$r_c = \frac{E(qx_c| - (qA)^2)}{qx_c} \tag{3.20}$$

where $E(x)$ is the complete elliptic integral of the second kind, and where x_c can be obtained from (3.10) as:

$$x_c = x_c^1 \equiv \frac{\pi - \arcsin\left(\frac{\tan\theta}{qA}\right)}{q} \tag{3.21}$$

This solution only exists if $\tan\theta < qA$. Under these conditions, it is easy to see that there is another solution to (3.10):

$$x_c^2 \equiv \frac{\arcsin\left(\frac{\tan\theta}{qA}\right)}{q} \tag{3.22}$$

where $x_c^2 < x_c^1$. Figure 3.2 shows graphically the behaviour of $\mathcal{F}^F$ as a function of x_c in the range $[0, L/2]$. For $\theta > \theta^* = \arctan(qA)$ the free energy $\mathcal{F}^F$ can be shown to be an increasing function of x_c. Note that (3.9) implies that $\mathcal{F}^F(x) \approx \mathcal{F}^D + \mathcal{A}\sigma_{lv}(1-\cos\theta)qx/\pi$ near $x = 0$, and $\mathcal{F}^F(x) \approx \mathcal{F}^W + \mathcal{A}\sigma_{lv}(1-\cos\theta)(qx/\pi - 1)$ near $x = L/2$. Thus the global minimum corresponds to $x_c = 0$, i. e. to the D state. As θ decreases below θ^*, two local extrema emerge: a minimum at $x_c = x_c^1$ given by (3.21), which corresponds to a metastable F state, and a maximum at $x_c = x_c^2$ given by (3.22). So, θ^* corresponds to the F state spinodal. As θ is further decreased, i.e. the temperature increases, the value of $\mathcal{F}^F$ for the F state decreases until it reaches the value of $\mathcal{F}^D$ for $\theta = \theta_f$ at the filling transition. As the value of x_c^1 for the coexisting F state is non-zero, the filling transition within the macroscopic theory is first-order. In order to locate the wetting transition, we note that, within the macroscopic theory, the W state has the same free energy than the F state for $x_c = L/2$. This value is always higher than the free energy corresponding to the F state if $\theta > 0$. This observation has two consequences. First of all, the filling transition occurs at lower temperatures than the complete wetting temperature predicted by the Wenzel law, i.e. when $\mathcal{F}^D = \mathcal{F}^W$. So, the filling transition preempts Wenzel's complete wetting transition. On the other hand, the value of x_c^1 given by (3.21) increases as θ decreases, and it reaches the value of $x_c = L/2$ for $\theta = 0$. Therefore, the macroscopic theory predicts that the wetting transition on a sinusoidal substrate is *continuous* and occurs at the same temperature that for the the flat substrate, so the existence of first-order wetting transitions (and associated off-coexistence transitions such as prewetting) cannot be predicted within the macroscopic theory.

Figure 3.3 shows the dependence of the contact angle at filling transition, θ^F, and the value of x_c at the filling transition, x_c^F, as a function of A/L. We see that, for large A/L, $\cos\theta^F$ scales as L/A, while qx_c^F is quite

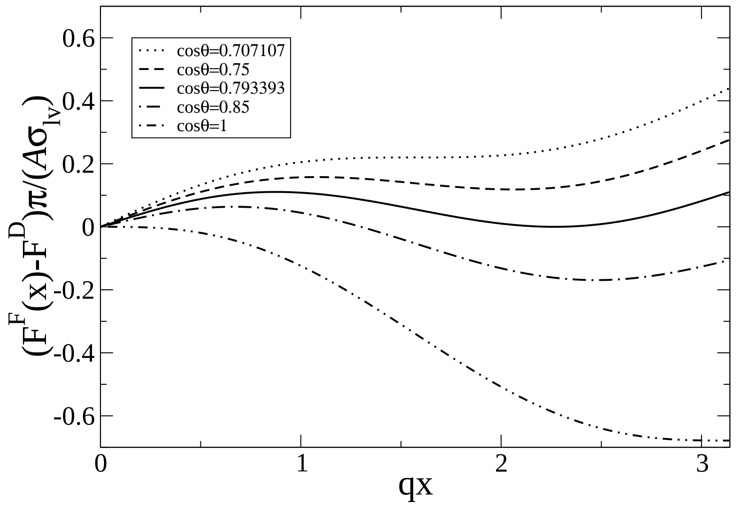

Figure 3.2: Behaviour of $\mathcal{F}^F(x)$ as a function of qx for $qA = 1$ and contact angles: $\theta = \theta^*$ (dotted line), $\theta_f < \theta < \theta^*$ (dashed line), $\theta = \theta_f$ (solid line), $\theta < \theta_f$ (dot-dashed line), and $\theta = 0$ (double dot-dashed line).

insensitive to the value of A/L and asymptotically tends to a constant as $A/L \to \infty$. To explain this behaviour, recall that the values of θ^F and x_c^F solve simultaneously (3.10) and (3.14). For large $(qA)^2$, we can approximate $\sqrt{1+\psi_x^2} \approx |\psi_x| = qA \sin qx$ for $x > 0$. Thus, (3.10) leads to the condition:

$$\sin qx_c^F = \frac{1}{qA \cos \theta^F} \tag{3.23}$$

which is compatible with (3.21) if $\theta \approx \pi/2$. Substituting this expression in (3.14), we reach to the following equation for x_c^F:

$$qx_c^F \sin qx_c^F + \cos qx_c^F = 1 \tag{3.24}$$

with a solution $qx_c^F \approx 2.33$. Consequently, the midpoint interfacial height for rough substrates is almost independent of L, and approximately equal to $A(1 - \cos qx_c^F) \approx 1.69A$. Substituting (3.24) into (3.23), we have the following asymptotic expression for θ^F:

$$\cos \theta^F \approx 0.22 \frac{L}{A} \tag{3.25}$$

We see from figure 3.3 that these asymptotic expressions are extremely accurate for values of $A/L > 1$.

To finish the description of the macroscopic theory, we note that both D and F states can also be obtained out of the two-phase coexistence. In

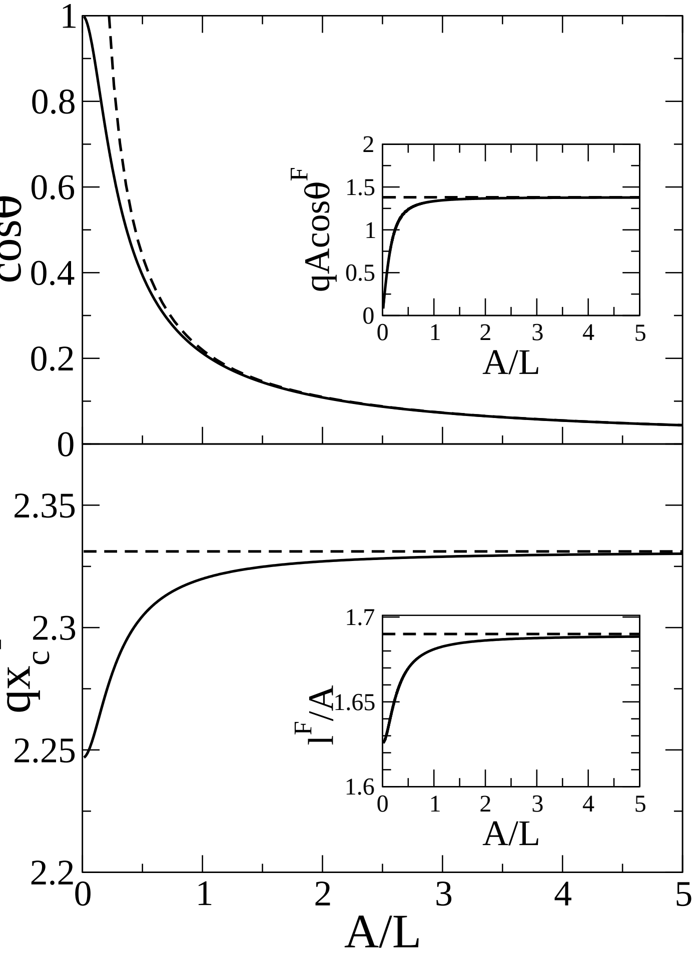

Figure 3.3: Top panel: plot of the cosine of the contact angle at the filling transition θ^F for $h = 0$ as a function of A/L. The dashed line corresponds to the asymptotic expression (3.25). Inset, representation of $qA\cos\theta^F$ as a function of A/L, being the dashed line the limiting value from the asympotic analysis for rough substrates. Bottom panel: plot of qx_c^F as a function of A/L. The dashed line is the limiting value from the asympotic analysis. Inset: plot of the midpoint interfacial height above the substrate of the F state at the filling transition, l^F, in units of the substrate amplitude A, as a function of A/L. The dashed line corresponds to the asymptotic value for $A/L \to \infty$.

the case of the F states, they can observed on a limited range of values of chemical potencial close to coexistence, where the liquid is still a metastable state. Their typical configurations are shown in figure 3.1(iv): the liquid-vapour interface is no longer flat but shows a cylindrical shape, with a radius given by the Young-Laplace equation:

$$R = \frac{\sigma_{lv}}{(\rho_l - \rho_g)|\Delta\mu|} \tag{3.26}$$

where ρ_l and ρ_g are the liquid and vapour densities at coexistence, and $\Delta\mu$ is the chemical potential shift with respect to the coexistence value. The free energy $\mathcal{F}^F$ is obtained by making a suitable modification of (3.9) as:

$$\begin{aligned} \mathcal{F}^F &= \mathcal{F}^D + \frac{2\mathcal{A}}{L}\sigma_{lv}\Bigg(\frac{R}{2}\arcsin\frac{x_c}{R} \\ &- \cos\theta\int_0^{x_c}\sqrt{1+\psi_x^2(x)}dx + \frac{x_c\psi(x_c)}{R} \\ &- \frac{1}{R}\int_0^{x_c} dx\psi(x) + \frac{x_c}{2}\sqrt{1-\left(\frac{x_c}{R}\right)^2}\Bigg) \end{aligned} \tag{3.27}$$

At the equilibrium configuration the liquid-vapour interface makes contact with the substrate at a value $x = x_c$ where the angle between the liquid-vapour interface and the substrate is equal to the contact angle for the flat substrate θ, so x_c is the solution of the following implicit equation:

$$\theta = \arctan\psi_x(x_c) - \arcsin\frac{x_c}{R} \tag{3.28}$$

For the sinusoidal substrate, this equation reads:

$$\theta = \arctan(qA\sin qx_c) - \arcsin\frac{x_c}{R} \tag{3.29}$$

which can be solved numerically or graphically, with a solution qx_c which is a function of θ, qA and qR.

The off-coexistence filling transition occurs when $\mathcal{F}^F = \mathcal{F}^D$. By using (3.27) and (3.28), it is possible to find numerically the characteristics of the F state which is at equilibrium with the D state. For the sinusoidal substrate, we find that qx_c is a function only of qA and qR. Our numerics show that, for fixed qA, the midpoint interfacial height l, defined as:

$$l = A(1-\cos qx_c) - R(1-\sqrt{1-(x_c/R)^2}) \tag{3.30}$$

decreases as qR decreases (i.e. $|\Delta\mu|$ increases), until vanishes for some critical value of qR. This state corresponds to the macroscopic theory prediction for the critical point of the filling transition.

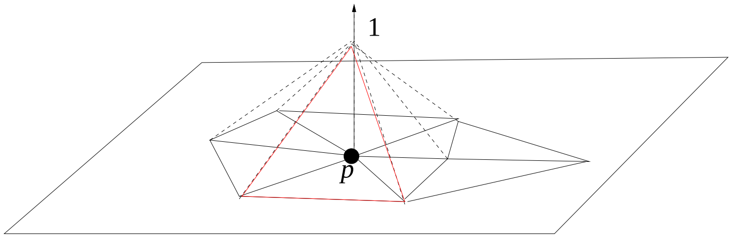

Figure 3.4: Example of linear node shape functions on a 2D domain

3.3 Methodology

Our starting point is the Landau-Ginzburg functional for subcritical temperatures:

$$\begin{aligned} \mathcal{F} &= \int_V d\mathbf{r} \left[\frac{1}{2}(\boldsymbol{\nabla} m)^2 - hm + \frac{1}{8}(m^2-1)^2 \right] \\ &+ \int_S d\mathbf{s} \frac{c}{2}(m-m_s)^2 \end{aligned} \tag{3.31}$$

based on a magnetization order-parameter $m(\mathbf{r})$. As explained in the Appendix A, with this choice the bulk magnetization at coexistence takes the value 1 or -1, and the bulk correlation length $\xi = 1$, which provides the unit of length for all length scales. Taking into account the continuous translational symmetry along the y-axis, and the periodicity across the x-axis, the minimization of the functional (3.31) is performed in the geometry depicted in figure 3.5. The bottom boundary is one period of the sinusoidal substrate shape (3.17). The values of the magnetization at this boundary are free, except in the case $c = \infty$, where the Dirichlet boundary condition $m(\mathbf{s}) = m_s$ is imposed. On the top boundary at $z = H_{cell}$, the magnetization is fixed to the bulk value (-1 if $h = 0$). The value of H_{cell} must be large enough in order to mimic the effect of an infinite domain. We take as value of $H_{cell} = 4A$, for which we did not find any size-effect. Finally, periodic boundary conditions are imposed at the vertical boundaries.

We have numerically minimized the free-energy functional (3.31) to determine the equilibrium magnetization profiles for different substrate geometries and surface couplings. The minimization was done with a finite element method, using a conjugate-gradient algorithm to perform the minimization (see Appendix ...). The finite element method was introduced by R. Courant, and it has become one of the most powerful tools to solve numerically partial differential equations (PDE), by using the Ritz-Rayleigh or Galerkin method [153]. In this approach, the solution of the PDE is written as a linear combination of a set of linear independent functions $\{N_i(\mathbf{r})\}$, for $i = 1, \ldots, n$. These functions are named shape functions. Substitution of this ansatz into the free-energy functional leads to a function on the expansion coefficients c_i, which are obtained by numerical minimization. Up to now, the shape functions are arbitrary. The finite element method uses a particular choice for this set. First, the spacial domain where the functional is defined is divided into disjoint regions called elements. In each element, some special points called nodes are identified, and different elements may share nodes. A typical construction is a triangulation, where the element mesh is constituted by triangles, where the nodes are their vertices. Now, the nodal shape functions are piecewise-defined polynomials in each element, with the following properties: (a) they are continuous everywhere (for 2nd order PDEs); and (b) they vanish in all the nodes of the domain but one where takes a value of 1. With these properties, the number of shape functions is equal to the number of nodes, and the coefficients c_i can be identified to the value of the shape function at its non-vanishing node. The order of the polynomial to define the shape function and the element geometry are connected, so, for example, in the triangulation mesh mentioned above only piecewise-defined linear functions satisfy all the properties we require to the shape functions. In our work we will consider linear shape functions defined on triangular meshes (see Fig. 3.4). The numerical discretization of the continuum problem was performed with adaptive triangulation coupled with the finite-element method in order to resolve different length scales [105]. This method was succesfully applied to the minimization of a Landau-de Gennes functional for the study of interfacial phenomena of nematic liquid crystals in presence of microstructured substrates [102–104, 129, 136]. For each substrate geometry and value of surface enhancement c, we obtain the different branches of interfacial states D, F and W on a wide range of values of the surface coupling for the bulk ordering field $h = 0$. Additionally, in order to locate the off-coexistence filling transition and, when the wetting transition is first-order, the prewetting line, we also explored the different free-energy branches out of coexistence, i. e. $h < 0$. In this case, the values of the surface coupling are restricted to be above the filling and wetting transitions at bulk coexistence, i.e. $h = 0$. The true equilibrium state will be the state that gives the least free energy at the same thermodynamic conditions, and the crossing between the different free-energy branches will correspond to the phase transitions. Finally, the interface will be localized by using a crossing criterion, i. e. at the points where the order parameter profile vanishes.

The initial state for each branch is obtained at a suitable value of the surface coupling by using as initial condition for the minimization procedure a state where the magnetization profile takes a constant value $+1$ for the mesh

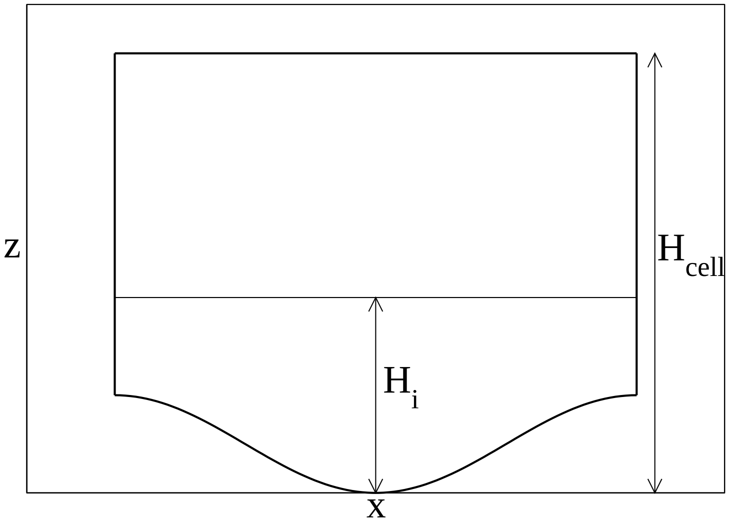

Figure 3.5: Finite-size geometry considered in our numerical study of the sinusoidal substrate. See text for explanation.

nodes with $z < H_i$ (see figure 3.5), and -1 otherwise. After minimization, the mesh is adapted and the functional is minimized again. We iterate this procedure a few times (typically 2-4 times). The value of H_i depends on the branch: $H_i = 0$ for the D branch (i.e. the initial magnetization profile is -1 everywhere), $H_i \sim A + H_{cell}/2$ for the W branch and $H_i \gtrsim A$ for the F branch. Once the first state is obtained, we may follow the branch slowly modifying the value of the surface coupling, using as initial condition for the next value of the surface coupling the outcome corresponding to the current minimization. Alternatively to the procedure outlined above, we may obtain the W free-energy branch for $h = 0$ by imposing a fixed value of the magnetization $+1$ on the top boundary, and using as initial magnetization profile $+1$ everywhere. In order to obtain the free energy of the W states, we add to the minimized free energies the contribution due to an interface between the two bulk coexisting phases, which is equal to $2L/3$ (see (A.19)), where L is the period of the sinusoidal substrate in the x-axis.

3.4 Numerical results

Following the methodology described in the previous section, we numerically studied the interfacial phenomenology that the system shows in presence of the sinusoidal substrate within the mean-field approximation. As interfacial Hamiltonian theories point out that the phenomenology will depend on the type of wetting transition when the system is in contact with a flat substrate [114,117,118], we consider two situations: $c = 0$ and $c = +\infty$, that correspond to first-order and critical wetting, respectively (see Appendix A). Theory predicts the ratio between the amplitude and roughness period A/L is a key parameter, so in general we consider the cases $A/L = 0.5, 1, 1.5$ and 2, although for some systems we have considered other values of A/L. To assess the dependence on L, for each value of A/L we consider different substrate periods in a range $L = 5 - 100$. Note that with this choice the typical lengscales which characterize the substrate geometry are larger than the bulk correlation length, so our approach based on the Landau-Ginzburg-Wilson is appropriate.

3.4.1 Results for $c = 0$, $h = 0$

Under this condition, the relevant surface coupling parameter is h_1, taken as the limit $c \to 0$, $m_s \to \infty$ and $cm_s \to h_1$. Furthermore, the surface coupling energy in (3.31), up to an irrelevant constant, has the expression $-\int_{\mathcal{S}} d\mathbf{s} h_1 m(\mathbf{s})$. As shown in the Appendix A, the reduced surface coupling h_1 plays the role of the temperature T, as $h_1 \sim (T_c - T)^{-1}$, where T_c is the bulk critical temperature. The first-order wetting transition for a flat substrate occurs for a surface field $h_1 = h_1^{w,\pi} \approx 0.34$. On the other hand, the prewetting critical point occurs at $(h_1, h) = (h_1^{cpw}, h^{cpw}) \approx (0.847, -0.1925)$. Therefore, we have explored the values of $h_1 \in [0, 1]$ and $h \in [-0.5, 0]$.

We start our study under bulk coexistence conditions, i.e. $h = 0$. In order to compare the minimization results for $h = 0$ with the macroscopic theory, we obtained analytical expressions for the free-energy densities $f \equiv \mathcal{F}/\mathcal{A}$, where $\mathcal{F}$ is the interfacial free energy and $\mathcal{A}$ is the projected area of the substrate in the $x - y$ plane. Substitution of the Landau-Ginzburg surface tensions (A.18), (A.19) and (A.20) into (3.5), (3.6) and (3.11) leads to the following expressions for the three free-energy branches at $h = 0$:

$$f^D = \frac{2}{3\pi}\left(1 - (1 - 2h_1)^{3/2}\right) E(-(qA)^2) \tag{3.32}$$

$$\begin{aligned} f^F &= \frac{2}{3} - \frac{2}{3\pi}\beta \\ &+\frac{2}{3\pi}(1 - (1 - 2h_1)^{3/2})E(-(qA)^2) \\ &-\frac{1}{3\pi}\Big((1 + 2h_1)^{3/2} - (1 - 2h_1)^{3/2}\Big)E\left(\pi - \beta | - (qA)^2\right) \\ &\text{with } \beta = \arcsin\frac{1}{qA}\sqrt{\frac{4}{\left((1 + 2h_1)^{3/2} - (1 - 2h_1)^{3/2}\right)^2} - 1} \end{aligned} \tag{3.33}$$

$$f^W = \frac{2}{3} + \frac{2}{3\pi}\left(1 - (1 + 2h_1)^{3/2}\right) E(-(qA)^2) \tag{3.34}$$

where $E(x)$ and $E(x|y)$ are the complete and incomplete elliptic integrals of the second kind, respectively, and $qA = 2\pi A/L$.

Figure 3.6 shows the free energy densities of the different branches as a function of h_1 at bulk coexistence. For a fixed value of A/L, the D and W branches are quite insensitive to the substrate periodicity L, and converge quickly to the macroscopic expressions (3.32) and (3.34). On the other hand, the F branch is more sensitive to L, although also converges to the macroscopic expression (3.33) for moderate values of L. Filling and the wetting transitions are located as the intersection between the D and F branches, and the F and W branches, respectively. Thus these transitions are both first-order. However, although the filling transition is clearly first-order in all the cases, the first-order character of the wetting transition weakens as L is increased. Note that the F and W branches approach almost tangentially each other for values of h_1 close to the wetting transition value, so the sensitivity to L of the F-branch leads to a strong L-dependence for the value of h_1 at the wetting transition. In general, the wetting transition values of h_1 are always smaller than the corresponding one to the flat substrate $h_1^{w,\pi} \approx 0.34$, in agreement with the predictions from interfacial Hamiltonian theory [62, 114, 120].

Figure 3.7 shows the typical magnetization profiles at the filling and wetting transition. We can see that the coexisting magnetization profiles at the filling transition are in good agreement with the schematic picture shown in figure 3.1, and the mid-point interfacial height follows accurately the macroscopic prediction. On the other hand, at the wetting transition (which for the macroscopic theory is continuous), we see that the mid-point interfacial height at the F state (c) is slightly below the substrate maximum height $2A$.

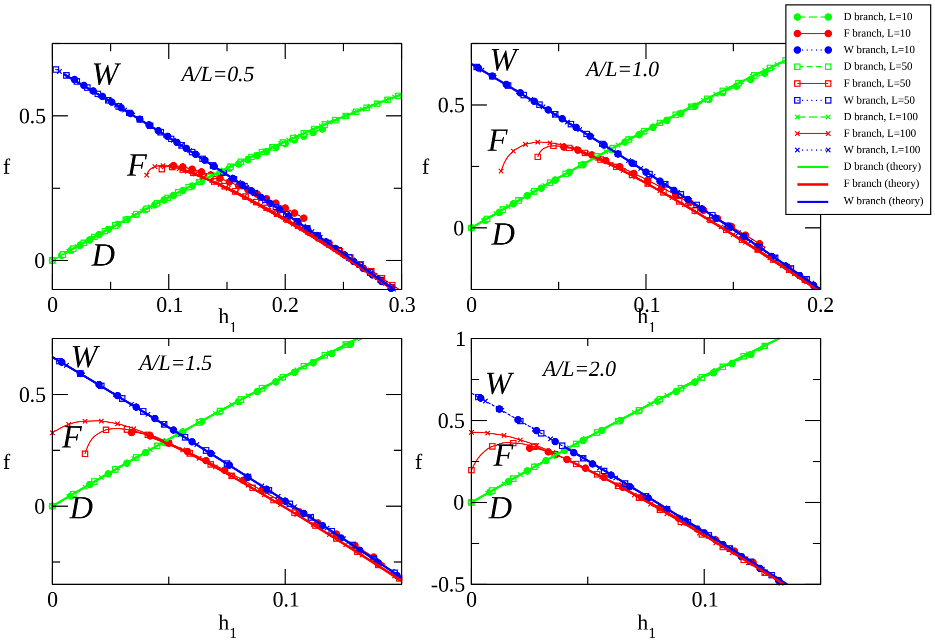

Figure 3.6: Plot of the free energy densities of the different branches of interfacial states for $c = 0$ at $h = 0$, as a function of the surface field h_1, for a sinusoidal substrate with $A/L = 0.5, 1, 1.5$ and 2, and $L = 10$ (crosses), $L = 50$ (open squares) and $L = 100$ (filled circles). The D states branch corresponds to the green (lighter grey) symbols, the W states branch to the blue (dark grey) symbols and the F states branch to the red (light grey) symbols. For comparison, the theoretical prediction from (3.32), (3.33) and (3.34) are also represented as continuous lines (the colour code is the same as for the numerical results).

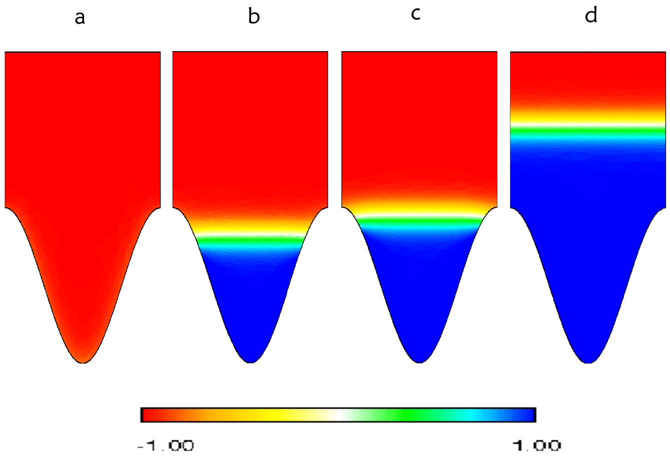

Figure 3.7: Magnetization profiles corresponding to the coexistence states at the filling transition (a and b) and the wetting transition (c and d) for $c = 0$, $h = 0$, $A/L = 0.5$ and $L = 20$.

This fact may indicate that the wetting transition of the rough substrate for large L is controlled by the wetting properties of the substrate at its top, with corrections associated to the substrate curvature there. Thus the wetting transition should remain first-order for all L and converge asymptotically to the wetting transition of the flat wall as $L \to \infty$. In order to check this hypothesis, we plot in figure 3.9 the wetting transition shift with respect to the flat value $h_1^{w,\pi} - h_1$ as a function of $\zeta = q\sqrt{A}$, which is the square root of the curvature at the substrate top. Our numerical data show a fairly good collapse in a master curve. For small ζ, this master curve seems to show an asympotically linear dependence with ζ. A simple argument may rationalize this result. Recall that close to the wetting transition the F state is characterized by an almost flat gas-liquid interface at a height slightly below the maximum substrate height $2A$. Consequently, the free-energy difference between the F and W states $\Delta\mathcal{F}$ comes from contribution of the region close to the substrate maximum. If ζ is small, we may approximate the shape of the substrate by the parabolic approximation $\psi(x) \sim 2A - \zeta^2(x - L/2)^2/2$. We can assume that the interfacial height with respect to the substrate maximum is close to the corresponding for the flat substrate for the partial wetting phase at the wetting transition. So, there will be a contribution to $\Delta\mathcal{F}$ which is proportional to the free-energy difference between the partial and complete wetting interfacial states at the wetting transition, which is proportional to

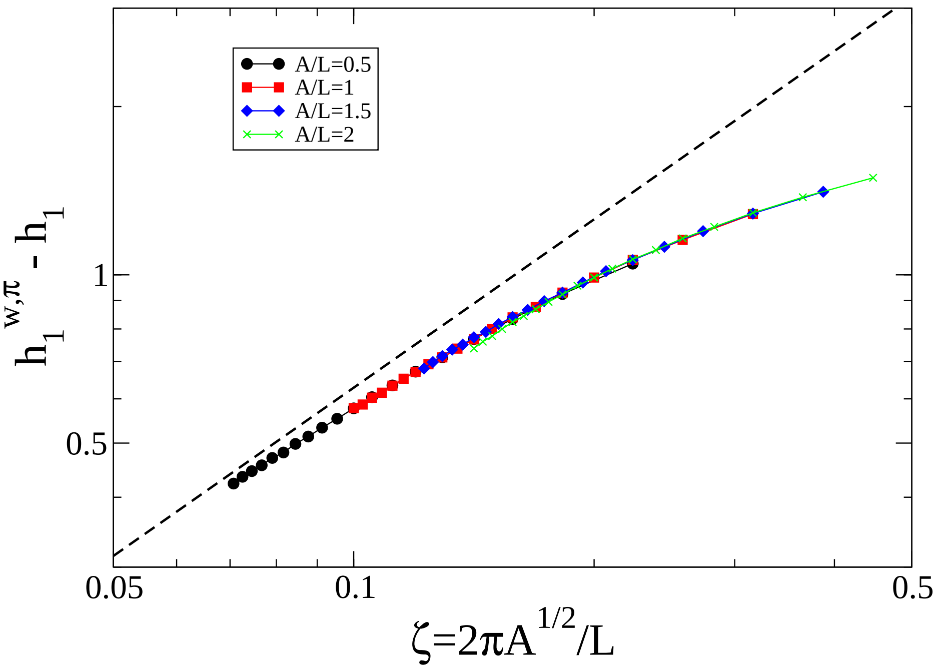

Figure 3.8: Plot of the wetting transition shift $h_1^{w,\pi} - h_1$ with respect to the flat substrate as a function of the curvature of the substrate at its top $\zeta = 2\pi\sqrt{A}/L$ for $L = 10 - 100$ and $A/L = 0.5$ (circles), $A/L = 1$ (squares), $A/L = 1.5$ (diamonds) and $A/L = 2$ (crosses). The dashed line indicates a linear dependence of the wetting transition shift with ζ.

$h_1 - h_1^{w,\pi}$ close to the transition, and to the length of the segment in the $x-$axis where there is no interface in the F state, which is inversely proportional to ζ. Obviously this contribution is always negative if $h_1 < h_1^{w,\pi}$. Thus, there must be another contribution to $\Delta\mathcal{F}$ which takes into account the distorsions in the magnetization profile with respect to the flat situation driven by the substrate curvature. This contribution should be positive, and we can assume that it is nearly constant for small ζ. At the wetting transition for the rough substrate, $\Delta\mathcal{F}$ should vanish. So, from the balance between these two terms of $\Delta\mathcal{F}$, we conclude that at the wetting transition $h_1 - h_1^{w,\pi} \sim \zeta$. Our observations seem to support this argument, but results for smaller values of A and/or larger values of L should be needed in order to establish its validity beyond any doubt.

Figure 3.9 represents the adsorption phase diagram at bulk coexistence. The phase boundaries correspond either to filling transitions between D and F phases, or wetting transitions between F and W states. We can see that the substrate roughness enhances the wettability of the substrate: as the

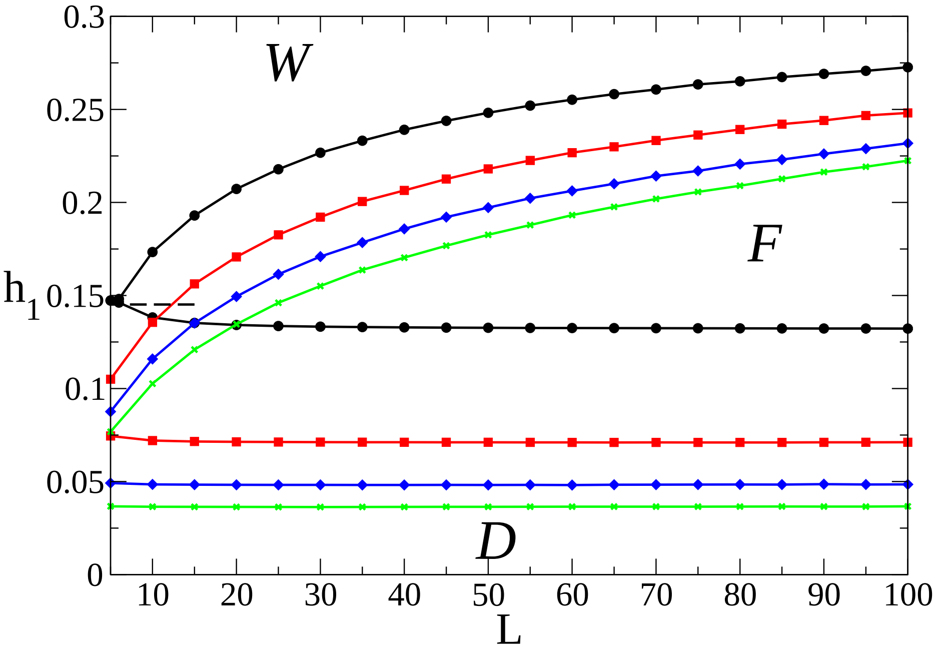

Figure 3.9: Adsorption phase diagram on a sinusoidal substrate with $c = 0$ and $h = 0$. The phase boundaries between D, F and W states are plotted for $A/L = 0.5$ (black circles), $A/L = 1$ (red squares), $A/L = 1.5$ (blue diamonds) and $A/L = 2$ (green crosses). Lines serve only as guides for the eyes. The dashed line shows the wetting transition value from Wenzel law prediction (3.13) for $A/L = 0.5$.

substrate is rougher the wetting and filling transitions are shifted to lower values of h_1, leading to an increase of the stability region of the W phase at the expense of the F phase, and a reduction of the stability region of the D phase with respect to the F phase. In general, the location of the filling transition line depends only on the substrate roughness and is almost independent of the value of L, at a value of h_1 which almost coincides with the macroscopic theory prediction. In particular, from (3.25) and as $\cos\theta \approx 3h_1$ for small θ, the filling transition value is approximately equal to $0.073 \times (L/A)$ for $A/L \geq 1$. On the other hand, as mentioned above, the wetting transition has a strong L-dependence, and the values of h_1 at the wetting transition are always smaller than $h_1^{w,\pi}$.

For the substrate with $A/L = 0.5$ we see that as L decreases, the wetting and filling transition approach each other, until they meet at a $D - F - W$ triple point at $L \approx 6$. For values of L below the this triple point, there is only a first-order wetting transition between a D and a W state at a value of h_1 almost independent of the value of L given by Wenzel law prediction. The explanation of this phenomenon is that the free energy branch of F states, which in general exceeds the limiting value given by (3.33), becomes metastable in all the range of values of h_1 with respect to D or W states. As the D and W free-energy branches are quite insensitive to the value of L, the location of the wetting transition is given approximately by Wenzel's law (3.13). We have checked that, as the substrate becomes shallower, this triple point occurs for larger values of L: $L \approx 25$ for $A/L = 0.2$ and $L > 100$ for $A/L = 0.1$. In all the cases, the value of $A \sim 5 - 10$. On the contrary, for larger values of A/L we do not observe this scenario in the range of values of L studied, but we expect to observe it for smaller values of L, i.e. when A is of order of the correlation length.

3.4.2 Results for $c = +\infty$, $h = 0$

When the *enhancement* parameter tends to infinity, we can drop the surface coupling energy in (3.31), but the magnetization at the surface is fixed to the value m_s. As shown in the Appendix A, the surface magnetization m_s plays the role of the temperature T, as $m_s \sim 1/\sqrt{T_c - T}$, where T_c is the bulk critical temperature. The system in contact with a flat substrate has a critical wetting transition when the surface order parameter $m_s \to 1$. Therefore, we proceed in a similar way to the case $c = 0$, so the reduced free energy (3.31) is minimized subject to Dirichlet boundary conditions at the substrate for values of m_s between 0 and 1 and the bulk ordering field $h \in [-0.5, 0]$.

We start with the bulk coexistence conditions, i.e. $h = 0$. Figure 3.10

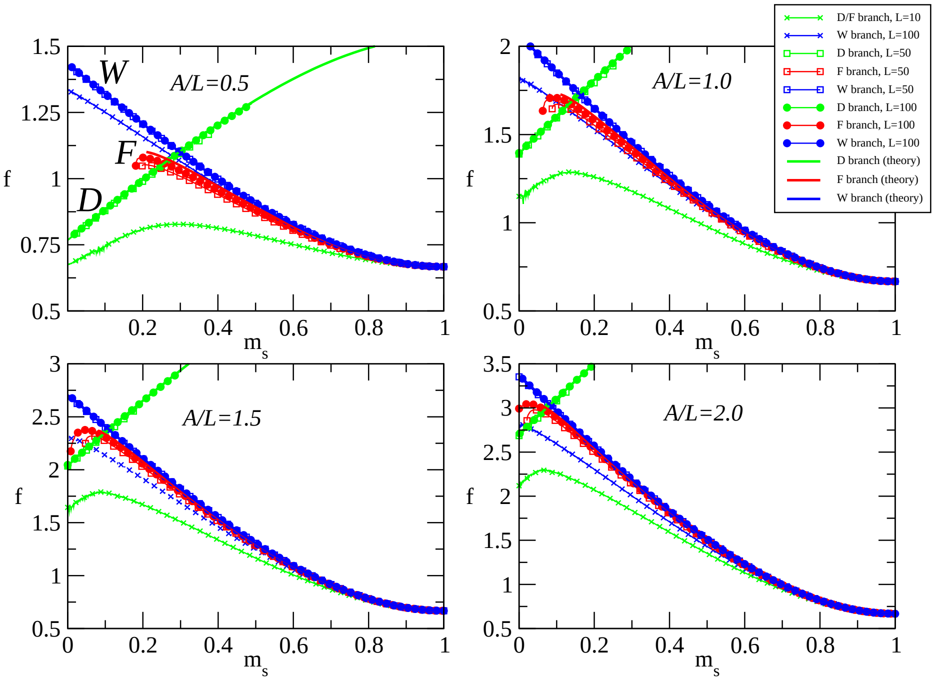

Figure 3.10: Plot of the free energy densities of the different branches of interfacial states for $c = \infty$ at $h = 0$, as a function of the surface magnetization m_s, for a sinusoidal substrate with $A/L = 0.5, 1, 1.5$ and 2, and $L = 10$ (crosses), $L = 50$ (open squares) and $L = 100$ (filled circles). The D states branch corresponds to the green (lighter grey) symbols, the W states branch to the blue (dark grey) symbols and the F states branch to the red (light grey) symbols. For comparison, the theoretical prediction from (3.35), (3.36) and (3.37) are also represented as continuous lines (the colour code is the same as for the numerical results).

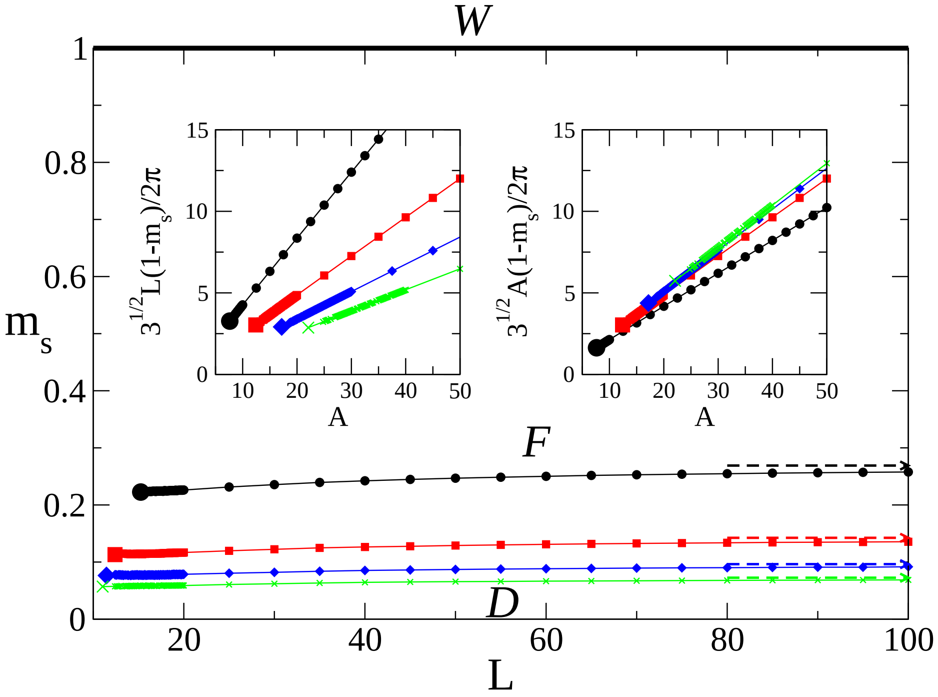

Figure 3.11: Adsorption phase diagram on a sinusoidal substrate with $c = \infty$ and $h = 0$. The phase boundaries between D and F states are plotted for $A/L = 0.5$ (black circles), $A/L = 1$ (red squares), $A/L = 1.5$ (blue diamonds) and $A/L = 2$ (green crosses) (the lines serve only as guides for the eyes). The arrows correspond to the filling transition values of m_s predicted by the macroscopic theory, and the big symbols to the filling transition critical points. Finally the wetting transition is represented by the thick continuous line for $m_s = 1$. Insets: plot of $\Delta\tilde{T} = \sqrt{3}L(1-m_s)/(2\pi)$ (left) and $(A/L)\Delta\tilde{T}$ (right) as functions of the substrate amplitude A along the filling transition line. The meaning of the symbols is the same as in the main plot.

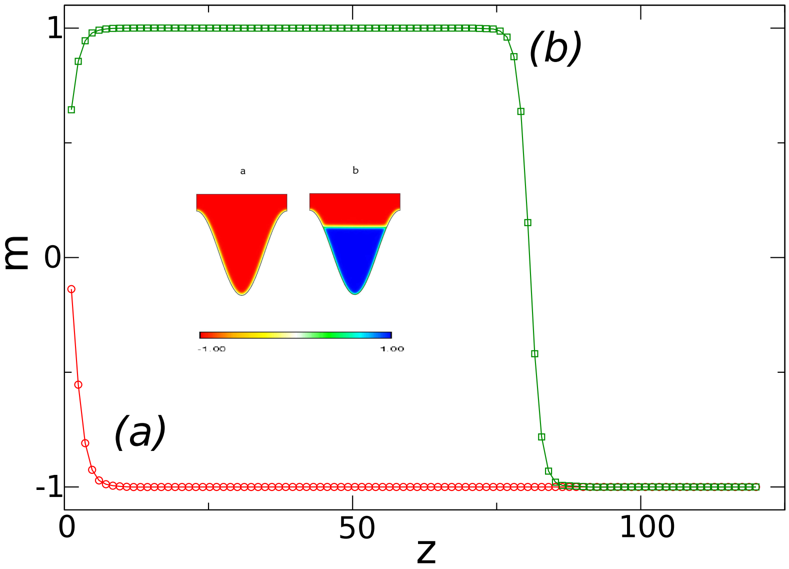

Figure 3.12: Magnetization profile along the vertical axis at $x = 0$ corresponding to: (a) the D state and (b) the F state at coexistence in the filling transition for $c = \infty$, $A/L = 0.5$ and $L = 100$. Inset: plot of the complete magnetization order parameter profiles of the coexisting D and F states.

represents the free energy densities as a function of m_s for the branches D, F and W. As in the case $c = 0$, each figure corresponds to a fixed value of A/L and different values of L. We also plot the theoretical predictions obtained from the macroscopic approach, which would correspond to the $L \to \infty$ limit:

$$f^D = \frac{2}{\pi}\left(\frac{m_s}{2} - \frac{m_s^3}{6} + \frac{1}{3}\right) E(-(qA)^2) \tag{3.35}$$

$$\begin{aligned} f^F &= \frac{2}{3} - \frac{2}{3\pi}\beta \\ &+ \frac{2}{\pi}\left(\frac{m_s}{2} - \frac{m_s^3}{6} + \frac{1}{3}\right) E(-(qA)^2) \\ &- \frac{1}{3\pi}\left(3m_s - m_s^3\right) E\left(\pi - \beta | - (qA)^2\right) \end{aligned} \tag{3.36}$$

$$\text{with} \qquad \beta = \arcsin\left(\frac{1}{qA}\sqrt{\frac{4}{\left(3m_s - m_s^3\right)^2} - 1}\right)$$

$$f^W = \frac{2}{3} + \frac{2}{\pi}\left(-\frac{m_s}{2} + \frac{m_s^3}{6} + \frac{1}{3}\right) E(-(qA)^2) \tag{3.37}$$

These results show several differences compared to the case $c = 0$. First, for every A/L the dependence on L is more pronounced in all branches, specially in the F branch. On the other hand, for small values of L the filling transition disappears as there is a continuous crossover from D to F states. Finally, the W branch is always metastable in the range $m_s \in [0, 1]$, and touches tangentially the F branch at $m_s = 1$. In fact, we observe a continuous unbinding of the interface along the F branch as $m_s \to 1$ from the magnetization profiles. For $m_s > 1$, the F and W branches coincide. From these observations we conclude that the wetting transition at the rough substrate is always continuous, and at the same value $m_s = 1$ as in the flat substrate. This is in agreement with the predictions of interfacial Hamiltonian theories [114, 117, 118]. On the other hand, the filling transition shows a slightly more pronounced dependence on L than in the case $c = 0$. Figure 3.11 shows the adsorption phase diagram at $h = 0$ for different values of A/L. For a fixed value of A/L and large L, the filling transition value of m_s increases with L, although it is bounded from above by the macroscopic theory transition value. Furthermore, the filling transition shifts towards lower values of m_s as the substrate is rougher. As in the $c = 0$ case, by using (3.25) and taking into account that $\cos\theta \approx 3m_s/2$ for small m_s, we find that that the limiting value for m_s at the filling transition scales as $0.146 \times (L/A)$ for $A/L \geq 1$. As L decreases, the filling transition disappears at a critical point, so for smaller values of L we observe the continuous crossover between the D and F states.

The existence of this critical point was also observed in the framework of interfacial Hamiltonian theories [114, 117, 118]. Furthermore, we tested the scaling property that $\Delta\tilde{T} \equiv \Delta T/q\sqrt{2\beta\Sigma}$ depends only on A, regardless the value of L [114, 117]. By using (A.31) and $\beta \equiv 4(c-1)/(1+c)$, in our case $\Delta\tilde{T} = \sqrt{3}L(1-m_s)/(2\pi)$. The inset of the figure 3.11 shows that they deviate from the interfacial Hamiltonian prediction. However, $(A/L)\Delta\tilde{T}$ seem to converge for small A, as well as $\Delta\tilde{T}$ as a function of L for small values of the substrate period.

In order to characterize the filling transition, we choose as the order parameter of the interface position along the vertical $x = 0$, i.e. above the minimum of the substrate. Figure 3.12 plots two typical magnetization profiles at the filling transition. The position of the interface is determined as the height at which the magnetization profile vanishes. If the magnetization profile is always negative (as in the D state in figure 3.12), the interfacial height is undetermined. These results show that the profiles are in agreement with the picture outlined in figure 3.1. So, any L-dependence of the transition value of m_s for large L with respect to the macroscopic prediction must arise from the order parameter profile distortions induced by the regions where the interface touches the substrate. The correction to f^F associated to these distortions scales as B/L, where B is the line tension associated to the liquid-vapor-substrate triple line and which depends on the contact angle θ. So, we expect that the shift of the transition value m_s with respect to the macroscopic prediction m_s^{macro} should scale as $1/A$ for large L and fixed substrate roughness A/L. Our results shown in figure 3.13 are in agreement with this prediction. Furthermore, we observe that the shift becomes almost independent of L for the roughest substrates $A/L \geq 1$. In order to explain this result, we may expand the free-energy density around m_s^{macro} for large A/L, and keeping the leading order terms, we obtain that, at filling transition:

$$f_F - f_D \approx -3.38\frac{A}{L}(m_s - m_s^{macro}) + \frac{B}{L} = 0 \qquad (3.38)$$

from which $m_s^{macro} - m_s \propto 1/A$.

For small L, the filling transition ends up at a critical point. Figure 3.14 plots the behaviour of the mid-point interfacial height of the coexisting D and F states, l_D and l_F, respectively, at the filling transition under bulk coexistence conditions. As a function of A, the mid-point interfacial height of the F states show a weak dependence on L, but its value is below the macroscopic prediction for large A/L, $l \approx 1.69A$. Close to the filling transition critical point our numerical scheme is not very accurate, so we are not able to locate directly the critical point. In order to estimate the location of the filling transition critical point, we followed a procedure very similar to

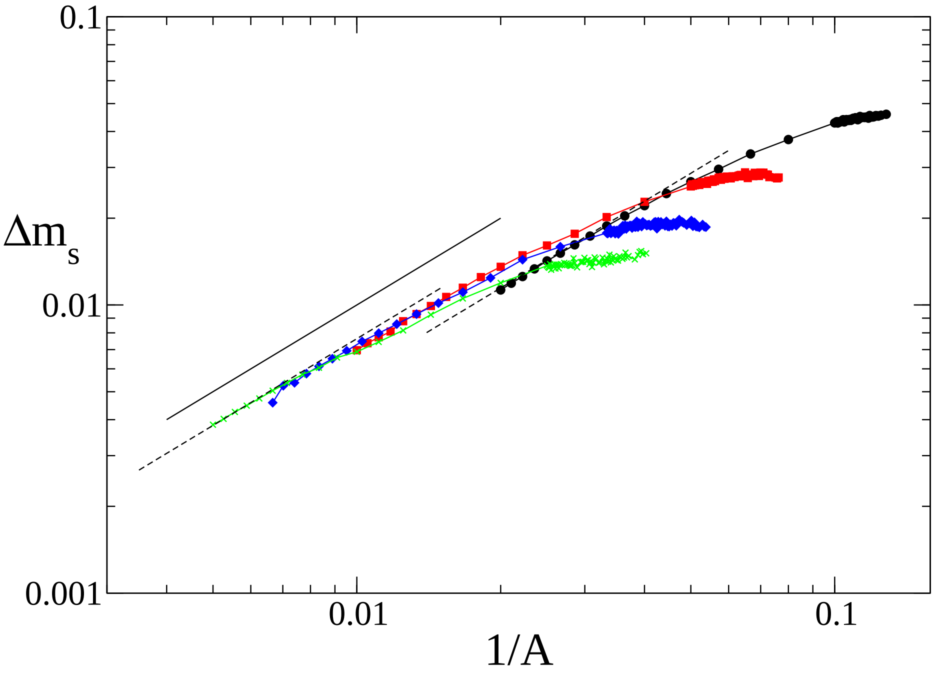

Figure 3.13: Plot of the filling transition shift $m_s^{macro} - m_s$ as a function of $1/A$, for $A/L = 0.5$ (circles), $A/L = 1$ (squares), $A/L = 1.5$ (diamonds) and $A/L = 2.0$ (crosses). Dashed lines correspond to the linear fits for the transition values for large A and $A/L = 0.5$ and $A/L = 2$. For comparison, a continuous line of slope 1 is also shown.

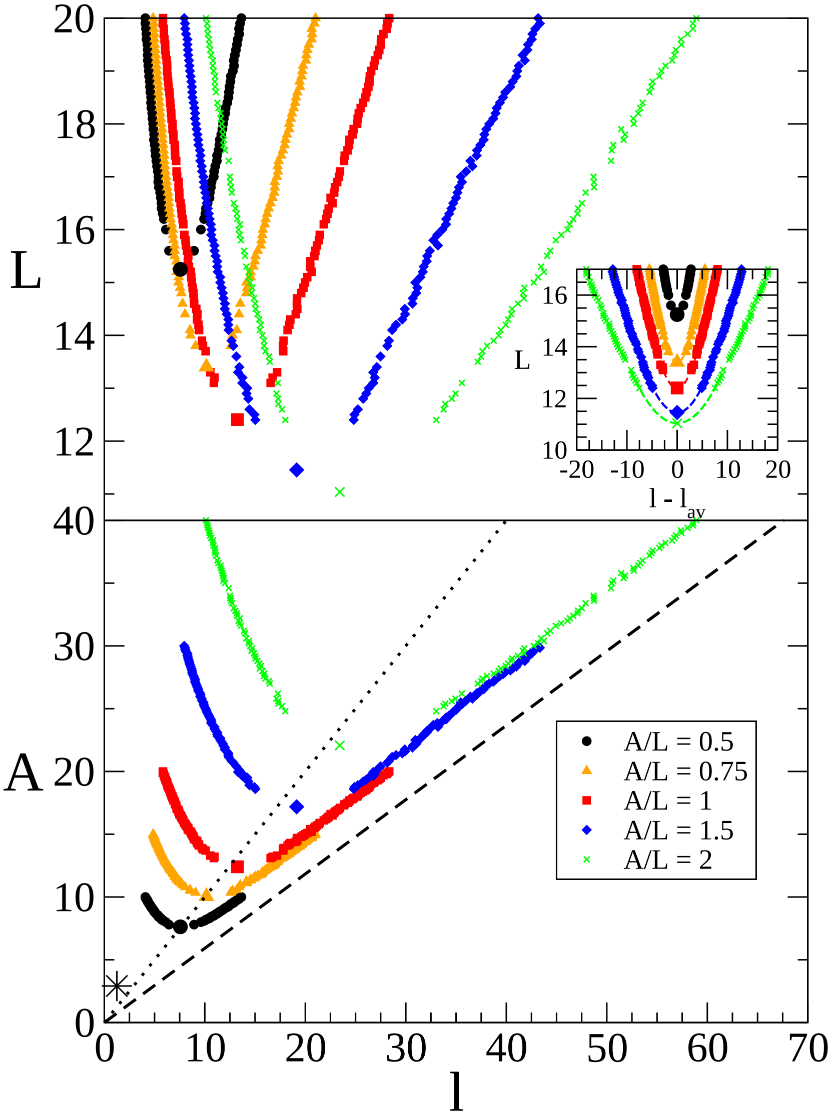

Figure 3.14: Plot of the mid-point interfacial height l of the coexisting D and F states at the filling transition for $h = 0$ as a function of L (top) and A (bottom) close to its critical point, for $A/L = 0.5$ (circles), $A/L = 0.75$ (triangles), $A/L = 1$ (squares), $A/L = 1.5$ (diamonds) and $A/L = 2.0$ (crosses). The star in the bottom panel corresponds to the location of the filling critical point predicted for shallow substrates from the interfacial Hamiltonian approach [117], and the dashed and dotted lines in the bottom panel are the mid-point interfacial height of the F state predicted from the macroscopic theory for large A/L at the filling transition and the spinodal line of the F states, respectively. Inset: plot of the deviations of the mid-point interfacial height of the D and F states at the filling transition for $h = 0$ with respect to their average value (the meaning of the symbols is the same as in the main panel).

the used to locate usual bulk liquid-gas transitions. First, we evaluate the average value $l_{av} = (l_F + l_D)/2$ of the interfacial heights of the coexisting D and F states for each m_s. After that, we substract to the interfacial heights l_D and l_F the average value computed previously (see inset of figure 3.14). This curve is quite symmetric around zero. Finally, we fit to a parabola the values of $l_D - l_{av}$ and $l_F - l_{av}$ for small values of L (i.e. close to the critical point), so the parabola height at its maximum gives an estimate of the critical value of L, and the value of l_{av} at the critical L gives the corresponding midpoint interfacial height. From figures 3.11 and 3.14 we see that, for the rougher substrates the critical value of L slightly decreases as A/L increases. On the other hand, by decreasing A/L the increase of the critical value of L is steeper. Regarding the critical values of A, we see that they increase as the substrate roughness increases, being this dependence nearly linear for the roughest substrates, in agreement with the fact that the critical value of L depends weakly on A/L for rough substrates. The location of the critical filling points is close to the spinodal line of the F states obtained from the macroscopic theory ($qx_c = \pi/2$ and $l = A$). Finally, it is worth to note that, if we extrapolate to the shallow substrate limit, i.e. $A/L \to 0$, our results are compatible with the predictions of interfacial Hamiltonian theories for shallow substrates, where the critical amplitude is $A = 2.914$, independently of the value of L [114, 117]. However, our results show that this prediction is no longer valid for rougher substrates.

3.4.3 Results for $c = 0$, $h < 0$

We turn back to the case $c = 0$, and now we explore the bulk off-coexistence interfacial phenomenology. In order to keep the bulk phase with negative magnetization as the true equilibrium state, we consider that the ordering field $h < 0$. Typically, we observe three different interfacial states with a finite adsorption, which are the continuation inside the off-coexistence region of the D, F and W branches, and that we will denote as D, F and F^* states, respectively. The D states are very similar to their counterparts at $h = 0$, except close to the filling critical point (see below), where a small adsorbed region of liquid develops on the substrate groove. The F states show partially filled grooves, where the liquid-vapour interface is curved, as shown in figure 3.1(iv). Finally, the F^* states correspond to completely filled grooves, with a thicker microscopic layer of liquid on top of the substate, which diverges as $h \to 0$. As in the F state, typically the liquid-vapour interface in the F^* states is curved.

In general, there are two transitions between these interfacial states: the filling transition between D and F states, and a transition between F and F^*

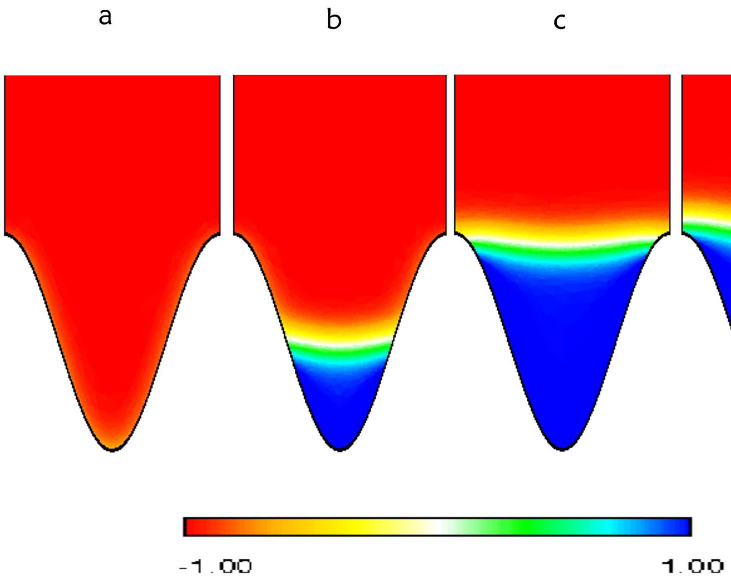

Figure 3.15: Magnetization profiles corresponding to the coexistence states at the filling transition (a and b) for $h = -0.025$ and the wetting transition (c and d) for $h = -0.0105$ for $c = 0$, $A/L = 0.5$ and $L = 20$.

states, which we will denote as prewetting transition, as its characteristics are reminiscent to those of the prewetting transition on the flat substrate, with the thickness of the liquid layer on the top of substrate as the order parameter. These transitions are first-order, and they are located at the crossing of the different free-energy branches for constant h, analogously to the procedure followed for $h = 0$. Both filling and prewetting transition lines end up at critical points, which are located by using the same technique as explained for the filling critical point in the $c = \infty$ case. Figure 3.15 shows the typical magnetization profiles of the coexisting states at filling and prewetting transitions, where a is a D state, b and c are F states and d is a F^* state.

Figure 3.16 shows the off-coexistence phase diagram for $L = 20$ and $L = 50$ corresponding to different values of A/L. Prewetting is restricted to a small range of values of h (as the prewetting line for the flat substrate). On the contrary, the filling transition is observed for a wider range of h. As $h \to 0$, the filling and prewetting lines tend to the states corresponding to the bulk coexistence filling and wetting transitions, respectively. For a given value of L, we observe that both filling and prewetting transitions shift towards lower values of h_1 as A/L increases. However, for $L = 50$ the prewetting lines for different roughnesses seem to collapse in a master curve for values of $|h|$ close to the prewetting critical point. The value of $|h|$ for the filling critical point increases as the substrate becomes rougher. On the contrary, the value of $|h|$ for the prewetting critical point decreases as A/L increases. Regarding the dependence on L for a fixed value of A/L, both filling and prewetting lines shift towards higher values of h_1 as L increases. The range of values of h where we observe the filling transition line is reduced as L increases, whereas for prewetting we observe different situations as L is increased: for $A/L = 0.5$ the value of $|h|$ for the prewetting critical point is larger for $L = 20$ than for $L = 50$, but the opposite occurs for $A/L = 1$, 1.5 and 2. However, the L-dependence of the prewetting line has not been systematically studied in order to confirm this observed trend.

A comparison with the macroscopic theory shows that, along the filling transition line, two different regimes can be observed. As explained in section 3.2, the macroscopic theory predicts that the filling transition also exists for off-coexistence conditions. Within this theory, the contact angle θ at the filling transition and l/A, where l is the midpoint interfacial height of the coexisting F state defined as (3.30), are only functions of qA and qR. We recall that θ is only function of h_1. On the other hand, by the Young-Laplace equation (3.26) adapted to the Ising model, $R = \sigma_{+-}/(2m_0|h|) = 1/(3|h|)$ in our units. So, the macroscopic theory predicts that, for a given value of A/L, both h_1 at the filling transition and l/A are functions of $qR = 2\pi/(3|h|L)$.

However, this scaling is only obeyed for small values of $|h|$. Figure 3.17 shows the midpoint interfacial height of the F states along the filling transition line. We see that, for both $L = 20$ and $L = 50$ and all values of A/L, our numerical results coincide with the macroscopic theory prediction for small h or, equivalently, large l/A. However, as l decreases, we see that the curve deviates from the theoretical prediction until reaches the critical point of the filling transition. This deviation starts in all cases when $l \sim 5 - 10$, i.e. when the midpoint interfacial height is of order of the correlation length, which occurs when $|h| \sim 1/L$. A closer insight on the magnetization profiles show that the midpoint interfacial heights of both D and F states near the filling transition critical point behave similarly to the interfacial heights along the prewetting line of a flat substrate (compare insets of figure 3.17 and figure A.3). In fact, the filling transition line seems to converge to the prewetting line for the flat substrate as L increases or A decreases. So, there is a crossover from a geometrically dominated behaviour at the filling transition for $|h| \lesssim 1/L$, to a prewetting-like behaviour for larger values of $|h|$, with can be regarded as a perturbation of the prewetting line with corrections due to the substrate curvature at the bottom.

Regarding the prewetting line, we observe that there is a strong L-dependence. For large L, we expect that prewetting lines converge to the corresponding to the flat substrate. However, this convergence is very slow, as it occurs for the associated wetting transition. Figure 3.18 shows the midpoint-interfacial height corresponding to the F and F^* states along the prewetting line. These coexistence curves show a high asymmetry associated to the interfacial curvature at $x = 0$, which increases with L for a given substrate roughness. Alternatively, we may use the surface magnetization at $x = L/2$ as the order parameter for the prewetting transition. The prewetting coexistence dome is more symmetric, but the location of the critical points is virtually indistinguishible from the obtained by considering the midpoint interfacial height. This fact indicates that our procedure to locate the critical points is accurate. However, we cannot use the interfacial height above the substrate top at $x = L/2$ as order parameter, since the surface magnetization corresponding to the F state is always negative. This fact is another indication of the slow convergence to the planar case.

If A is of order of the bulk correlation length, both filling and prewetting transitions can exist even when at bulk coexistence there is no filling transition (i.e. in the Wenzel regime). Figure 3.19 shows the interfacial phase diagram for $L = 5$ and $A/L = 0.5$. At bulk coexistence, there is only a wetting transition between a D and a W state at a value of h_1 close to the predicted by Wenzel law. For $h < 0$ but close to bulk coexistence, a prewetting line where D and F^* states coexist emerges tangentially to the

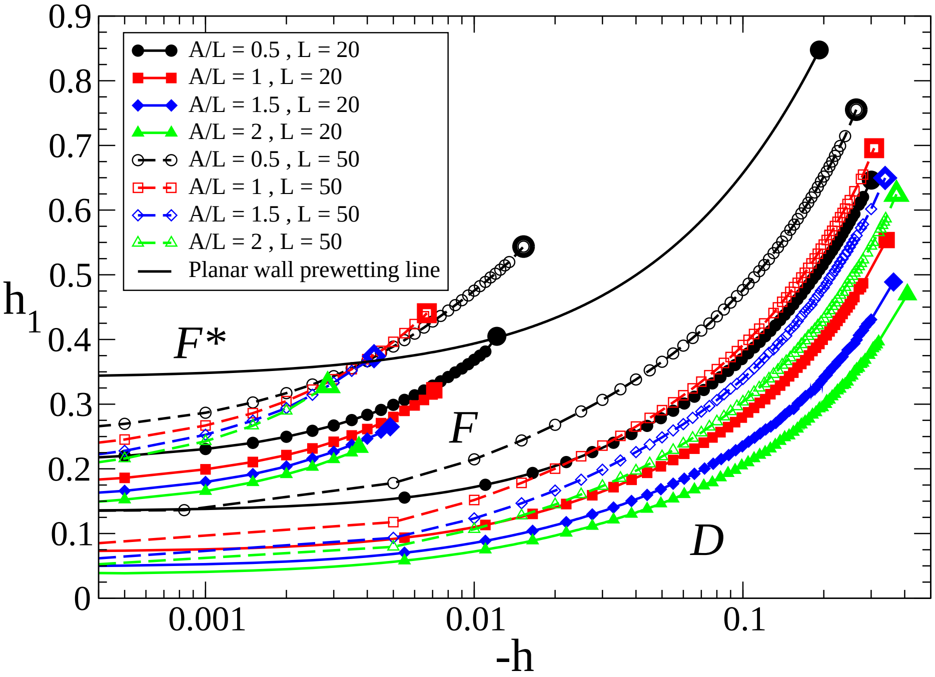

Figure 3.16: Off-coexistence $c = 0$ interfacial phase diagram. The phase boundaries between D and F (filling transition lines) and between F and F^* (prewetting transition lines) are represented by continuous lines/filled symbols for $L = 20$ and dashed lines/open symbols for $L = 50$. Circles correspond to the phase boundaries for $A/L = 0.5$, squares correspond to $A/L = 1.0$, diamonds correspond to $A/L = 1.5$ and triangles correspond to $A/L = 2.0$. The continuous line without symbols represents the prewetting line for the planar wall. Big symbols indicate the position of the critical points.

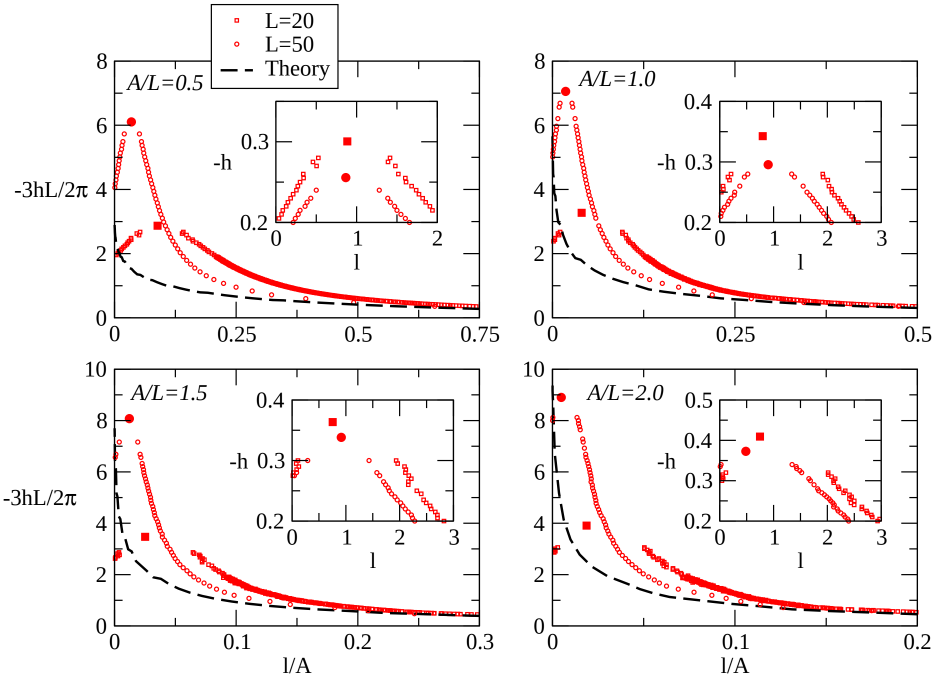

Figure 3.17: Plot of the midpoint interfacial height, in units of A, of the D and F states at the filling transition, as a function of $-3hL/2\pi$, corresponding to $c = 0$ and $A/L = 0.5, 1, 1.5$ and 2, for $L = 20$ (squares) and $L = 50$ (circles). The dashed line corresponds to the macroscopic theory prediction for the midpoint interfacial height of the F state. The insets show a zoom of the D and F states midpoint interfacial heights, in units of the correlation length, as a function of $|h|$, close to the filling critical points (the meaning of the symbols is the same as in the main plots).

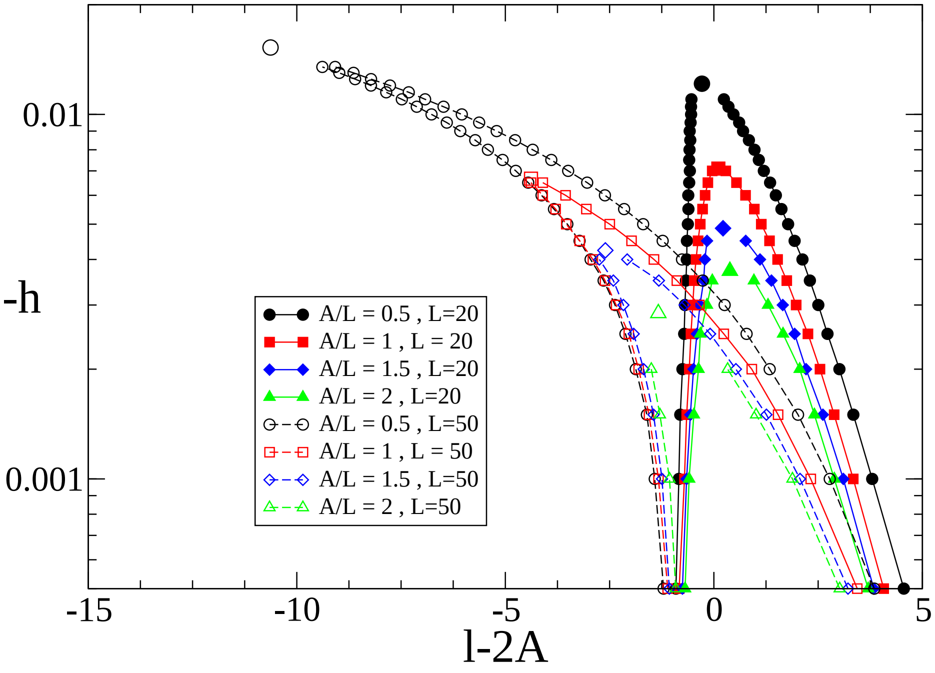

Figure 3.18: Plot of the midpoint interfacial height of the F and F^* states at the prewetting transition, as a function of h, corresponding to $c = 0$ and $A/L = 0.5$ (circles), $A/L = 1.0$ (squares), $A/L = 1.5$ (diamonds) and $A/L = 2$ (triangles), and $L = 20$ (full symbols) and $L = 50$ (open symbols). The largest symbols correspond to the locations of the prewetting critical points.

$h = 0$ axis from Wenzel wetting transition, as expected from the Clausius-Clapeyron relationship. As the magnetization at the surface for the D states is negative, the midpoint interfacial height is taken as zero. By decreasing h, we reach to a triple point at $h_1 \approx 0.153$ and $h \approx -0.0018$, where a D, F and F^* states coexist, and a filling and a prewetting transition lines emerge from this triple point. Note that the midpoint interfacial height of the F^* state in both prewetting lines decreases as $-\log(-h)$, analogously to the thick layer phase along the prewetting of flat substrates. On the other hand, the midpoint interfacial height of the D state along the filling transition remains zero until close to the critical point. If A is further decreased, both filling and $F - F^*$ prewetting transitions will eventually disappear, remaining only the $D - F^*$ prewetting transition. On the contrary, if A is increased, the $D - F - F^*$ triple point will be shifted towards $h = 0$, and beyond this value the filling and prewetting transitions will become independent.

3.4.4 Results for $c = \infty$, $h < 0$

Finally, we turn back to the off-coexistence phase diagram for $c = \infty$. As in this case the wetting transition is always continuous, only D and F states are observed for $h < 0$, with characteristics similar to the corresponding states for $c = 0$. Thus we need only to focus on the filling transition between D and F states. If this transition exists at bulk coexistence, it has an off-coexistence extension which ends at a critical point. Thus, for a given value of L, the filling transition line only exists for values of A/L larger than the value of the roughness for which the critical filling occurs at bulk coexistence. Figure 3.20 shows the off-coexistence phase diagram for $L = 20$ and $L = 50$, corresponding to different values of A/L. For each value of L we observe that the range of values of $|h|$ of the filling transition line, which is given by the value of h for its critical point, is a non-monotonous function of the roughness: the critical value of $|h|$ for small values of A/L increases, but it decreases for rougher substrates. This is in contrast with the interfacial Hamiltonian model prediction which states that the value of $|h|$ at the critical point of the filling transition is an increasing function of A [117]. However, it captures correctly the observed feature that the filling transition is shifted towards lower values of m_s. When comparing distinct values of L we see clear differences. First of all, the filling transition line is almost linear for $L = 20$ but it has some curvature for $L = 50$. For a given value of the roughness parameter A/L, the range of values of m_s and $|h|$ for the filling transition line increases with L. Although the filling transition lines start approximately at the same value (recall that there is some L-dependence on the filling transition at bulk coexistence), the slope of these lines for $h = 0$

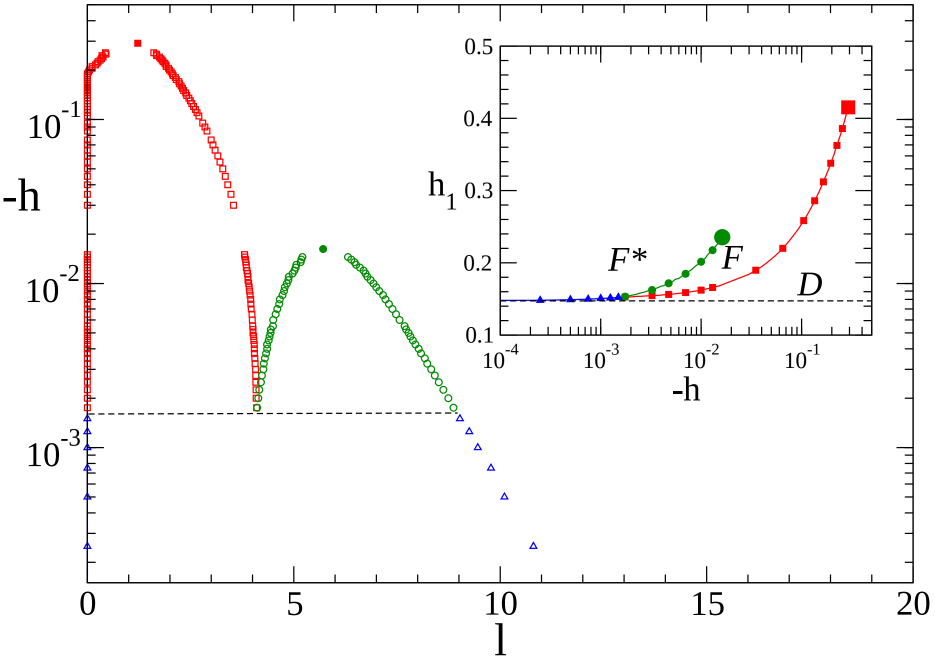

Figure 3.19: Plot of the midpoint interfacial height of the coexisting D and F states at filling transition (red squares), F and F^* states at the prewetting transition (green circles) and D and F^* states at the Wenzel prewetting transition (blue triangles) for $L = 5$ and $A/L = 0.5$. The full symbols correspond to the filling and prewetting critical points, and the dashed line indicates the location of the $D - F - F^*$ triple point. Inset: off-coexistence interfacial phase diagram for $L = 5$ and $A/L = 0.5$. The meaning of the symbols is the same as in the main panel. The dashed line indicates the location of the wetting transition at bulk coexistence.

depends strongly on L. In fact, this dependence can be rationalized by the macroscopic theory, which predicts that m_s along the filling transition is a function of $2\pi/(3|h|L)$, as it was discussed for the $c = 0$ case. As in the latter, we observe a qualitative agreement with the macroscopic theory prediction only for small values of $|h|$. On the other hand, the effective Hamiltonian model scaling behaviour of the off-coexistence filling transition [117], which states folowing the equation 3.4 with $\bar{h} \equiv 2|h|$, that for a given A and regardless the value of L, $\Delta\tilde{T} = \sqrt{2}L(1 - m_s)/(2\pi)$ is a function of $3|h|L^2/(2\pi)^2$. This result is completely broken down for our range of values of A.

Figure 3.21 shows the midpoint interfacial heights of the D and F states along the off-coexistence filling transition. Note that, as m_s is always positive, the D state has a positive midpoint interfacial height for all values of h. We see that the filling transition critical points have a midpoint interfacial height much larger than the bulk correlation length, although it decreases for larger L. This observation indicates that the emergence of the filling transition critical point for $c = \infty$ differs from the $c = 0$ case. Unlike the $c = 0$ situation, our numerical results show large deviations with respect to the macroscopic theory prediction for the midpoint interfacial height of the F states. Note that the macroscopic theory always overestimate the interfacial height, even for small $|h|$. However, as L increases, our numerical values seem to converge to the values obtained from the macroscopic theory. This suggests that for larger values of L the macroscopic theory and the numerical results may agree, at least if the midpoint interfacial height remains much larger than the correlation length. However, the uncertainties introduced by our numerical method for larger values of L prevented us to further explore this possibility.

3.5 Open questions

The study presented above is restricted to two extreme situations: $c = 0$ for first-order wetting substrates and $c = \infty$ for critical wetting substrates. However, we expect similar scenarios for small or large c, respectively. However, the borderline between these scenarios, which is expected to occur around the tricritical wetting conditions for the flat substrate, may present new interesting features. However, this study is beyond the present work.

Our model overcomes many of the problems with previous approaches, such as the neglected role of intermolecular forces in the macroscopic theory, or the appropriate form of the binding potential for the effective interfacial models for rough substrates [91,99]. However, the simplicity of our functional

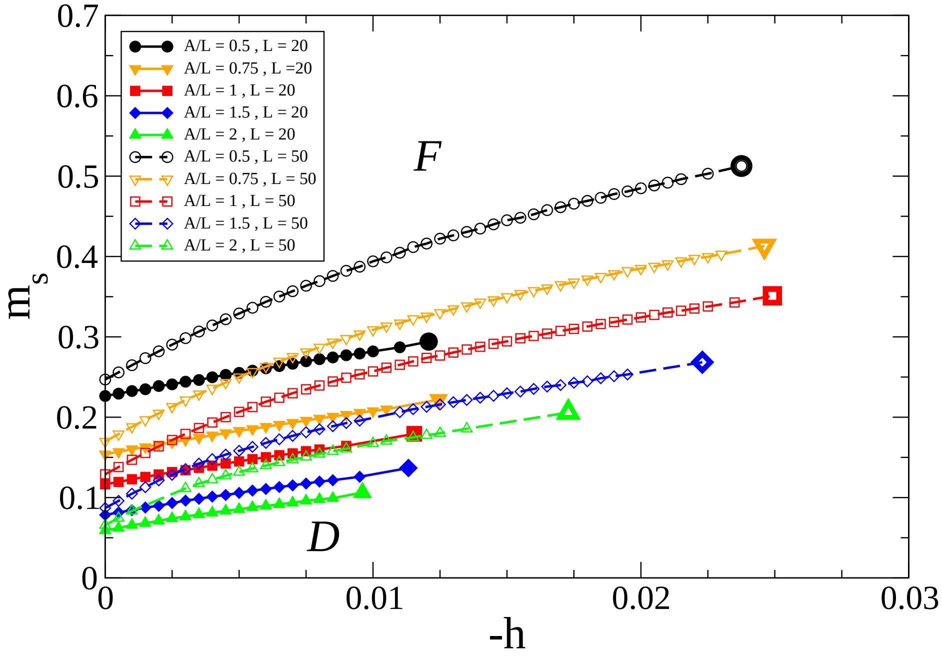

Figure 3.20: Off-coexistence $c = \infty$ interfacial phase diagram for $L = 20$ (continuous lines/filled symbols) and $L = 50$ (dashed lines/open symbols), corresponding to $A/L = 0.5$ (circles), $A/L = 0.75$ (triangles down), $A/L = 1.0$ (squares), $A/L = 1.5$ (diamonds) and $A/L = 2.0$ (triangles up). The big symbols indicate the position of the critical points.

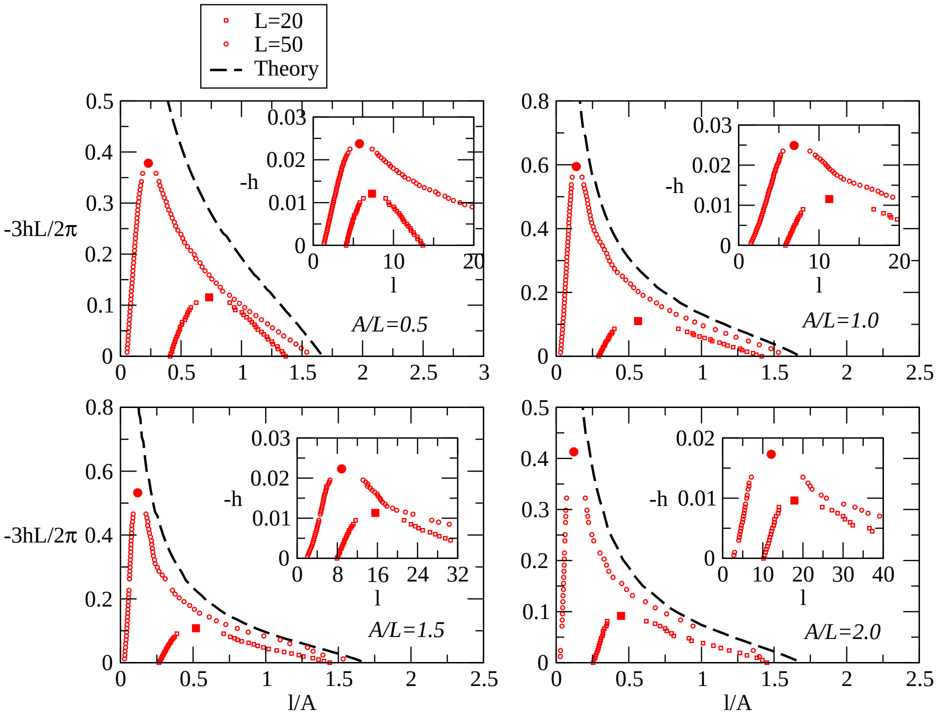

Figure 3.21: Plot of the midpoint interfacial height, in units of A, of the D and F states at the filling transition, as a function of $-3hL/2\pi$, corresponding to $c = \infty$ and $A/L = 0.5, 1, 1.5$ and 2, for $L = 20$ (squares) and $L = 50$ (circles). The dashed line corresponds to the macroscopic theory prediction for the midpoint interfacial height of the F state. The insets show a zoom of the D and F states midpoint interfacial heights, in units of the correlation length, as a function of $|h|$, close to the filling critical points (the meaning of the symbols is the same as in the main plots).

have additional disadvantanges. For example, it does not describe properly the packing effects close to the substrates due to the hard-core part of the intermolecular interactions, which is of order of the bulk correlation length away from the bulk critical point. As a consequence, the phenomenology for small L may be affected by these effects, and even for larger values of L some of the predicted transitions may be preempted by surface or bulk solidification. On the other hand, our functional is appropriate for short-ranged intermolecular forces, although in nature dispersion forces are ubiquous. In order to take into account the packing effects or long-ranged interactions, more accurate functionals should be used, as fundamental-measure density functional theories [69, 70, 73–75].

Our study is restricted to a simple structured substrate, but it is worthy to know how general are our predictions. To this purpose, it is important to distinguish between smooth subtrates (i.e. the substrate section is a smooth function) or cusped substrates, such as sawtoothed, crenellated or capped capillaries. In the latter, the cusps may pin the interface and the interfacial phenomenology is not determined uniquely by the surface wettability properties. But even for smooth substrates, an immense zoo of different behaviours may be observed, so it is difficult to generalize our results to arbitrarily shaped substrates. However, if the grooves are gradually filled by liquid (continuously or through one or a sequence of filling transitions), then the wetting transition is controlled by the wettability properties of the substrate close to the substrate maxima. Under these conditions, our results may be completely general. On the other hand, the macroscopic theory will describe accurately strong first-order interfacial transitions, i.e. those which involve states with very dissimilar liquid adsorptions.

Finally, in this study interfacial fluctuations are completely neglected due to its mean-field character. These may have an effect for the continuous transition. For short-ranged forces, $d = 3$ is the upper critical dimension for critical wetting of a flat substrate. So, we anticipate that capillary wave fluctuations may alter the critical behaviour of the critical wetting on the flat substrate. Furthermore, interfacial fluctuations may have more dramatic effects in transitions such as filling. In fact, although filling is effectively a two-dimensional transition (as it is prewetting), the interfacial fluctuations are highly anisotropic, since the interfacial correlations along the grooves axis are much stronger than across different grooves. This may lead to a rounding of the filling transition due to its quasi-one dimensional character, as it happens for single grooves. Further work is required to elucidate the effect of the interfacial fluctuations in the adsorption of rough substrates.

Chapter 4

Filling and wetting transitions on sinusoidal substrates: a mean-field study of the double parabola model

4.1 Introduction

Wetting and related interfacial phenomena can be studied at different levels. From a microscopic point of view, they can be analysed by using models which account for the molecular structure of the fluid, including simplified versions as the lattice gas isomorphic to the Ising model, or coarse-grained microscopic models such as the Landau-Ginzburg model. An alternative is the use of mesoscopic models where the free-energy cost of an interfacial configuration is modeled by an interfacial Hamiltonian model. However, there is a gap between the microscopic and mesoscopic approaches, since usually the interfacial Hamiltonians are proposed in an *ad hoc* way by generalizing simpler situations such as the interfacial phenomena on planar substrates. So, it is widespread to consider that the interfacial Hamiltonian has the following structure:

$$\mathcal{H}[\ell] = \int d\mathbf{r} \left\{ \Sigma\sqrt{1 + (\boldsymbol{\nabla}\ell)^2} + W(\ell) \right\} \tag{4.1}$$

where the first term accounts for the energy cost of increasing the area of the liquid-vapour interface (with a surface tension Σ in units of $k_B T$) and the second term is a *local* binding potential between the substrate and the liquid-vapour interface. For shallow substrates, $W(\ell)$ is related to the binding potential of a planar substrate W_π as $W(\ell) \approx W_\pi(\ell - \psi)$, where ψ is the local height of the substrate with respect to the horizontal reference plane. However, the extension to rough substrates is not obvious [47].

For short ranged forces, the first attemps to obtain systematically the interfacial Hamiltonians from a coarse-grained microscopic model are traced back to the work by Jin and Fisher [41,42,58,59]. However, their approach is a perturbative one as the solution is expanded around the planar case. More recently, a more general derivation was introduced by Parry and coworkers [7, 91–94, 98, 99]. They obtained that the interfacial Hamiltonian can be written as Eq. (4.1), but where $W \equiv W[\ell;\psi]$ is now a *non-local* functional of the interfacial and substrate shapes. Close to the wetting transition, it can expanded as [91]:

$$W[l,\psi] = 2\kappa m_0 \delta m_s$$

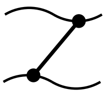

$$+\kappa m_0^2$$

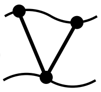

$$+ \kappa(\delta m_s)^2$$

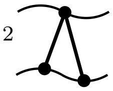

$$+\ldots \qquad (4.2)$$

where m_0 and $\delta m_s = m_s - m_0$ are the order parameter on each surface, the wavy lines represent the liquid-vapour interface and the substrate surface, the straight segment represents a bulk liquid correlation function and the black circles on each surface means that one must integrate over all the positions on that surface. Its derivation uses a simplified version of the Landau-Ginzburg model, the so-called double parabola model. However, it is possible to use a perturbation theory to generalize these results to the full Landau-Ginzburg model [92].

In this Chapter we will consider the wetting and related interfacial phenomenology on a sinusoidal substrate within the double parabola model. This study is interesting because it will allow us to check if the double parabola model is, at least qualitatively, a good representation of the Landau-Ginzburg model for wetting phenomena on rough substrates. On the other hand, this study will be a benchmark to test the interfacial phenomenology of the perturbative non-local models. As in the analysis for the Landau-Ginzburg model which was presented in the previous Chapter, our study will be at a mean-field level, so fluctuations are completely neglected.

4.2 Theoretical background

As in the previous chapter, our starting point is a free-energy functional of $m(\mathbf{r})$ (3.31)

$$\mathcal{F}[m] = \int_V d\mathbf{r}\left(\frac{(\boldsymbol{\nabla} m(\mathbf{r}))^2}{2} + \Delta\phi(m)\right) + \int_S d\mathbf{s}\frac{c}{2}(m-m_s)^2 \qquad (4.3)$$

where $m(\mathbf{r})$ is the order parameter at $\mathbf{r}$, $\Delta\phi(m)$ is a thermodynamic Landau-like potential, and c and m_s are the enhancement parameter and the favoured surface magnetization, respectively. The term $c(m - m_s)^2/2$ can also be written, up to an irrelevant constant, as $-h_1 m(\mathbf{s}) + \frac{c}{2} m(\mathbf{s})^2$, where we define $h_1 = c\, m_s$.

The thermodynamic Landau-like potential that we consider in this Chapter is a double parabola potential, which can be regarded as an approximation to the Landau-Ginzburg m^4 model (see Fig. 4.1)

$$\Delta\phi(m) = \frac{\kappa^2}{2} \left(|m| - m_0\right)^2 \tag{4.4}$$

where m_0 is the bulk magnetization. Eq. (4.4) can be written for each phase we have

$$\begin{aligned} \Delta\phi(m) &= \frac{\kappa^2}{2} \left(m - m_0\right)^2 \qquad \text{Liquid phase } (m > 0) && (4.5) \\ \Delta\phi(m) &= \frac{\kappa^2}{2} \left(m + m_0\right)^2 \qquad \text{Gas phase } (m < 0) && (4.6) \end{aligned}$$

At mean-field level, the equilibrium order parameter profile m_{eq} is obtained by minimizing the free-energy functional Eq. (4.3). The associated Euler-Lagrange equation to this functional is

$$\nabla^2 m_{eq}(\mathbf{r}) - \kappa^2 (m_{eq}(\mathbf{r}) \mp m_0) = 0 \tag{4.7}$$

and in the wall

$$\partial_n m_{eq}(\mathbf{s}) = -c\left(m_{eq}(\mathbf{s}) - m_s(\mathbf{s})\right) \tag{4.8}$$

where $\partial_n \equiv \mathbf{n}\cdot\boldsymbol{\nabla}$ is the normal derivative to the wall, with $\mathbf{n}$ being the outwards normal to the surface.

If the fluid in contact with the surface is in the same bulk phase everywhere, i.e. the order parameter does not change sign in the fluid volume, then the solution of Eq. (4.7) subject to the boundary conditions Eq. (4.8) and that $meq \to \pm m_0$ as $z \to \infty$ completely determines the equilibrium order parameter profile, as in the case for the Landau-Ginzburg functional. However, the situation becomes more complex when regions of different bulk phases can be found in the fluid, as it is the case when wetting layers are nucleated. We will consider that the bulk phase away from the substrate is the gas phase, and that close to the wall there is a layer of liquid phase. Under these circumstances, an additional inner boundary has to be considered, corresponding to the liquid-vapour interface located at the set of points where the order parameter vanishes. The shape of the liquid-vapour interface cannot be obtained by solving the Euler-Lagrange equation (4.7). However, as

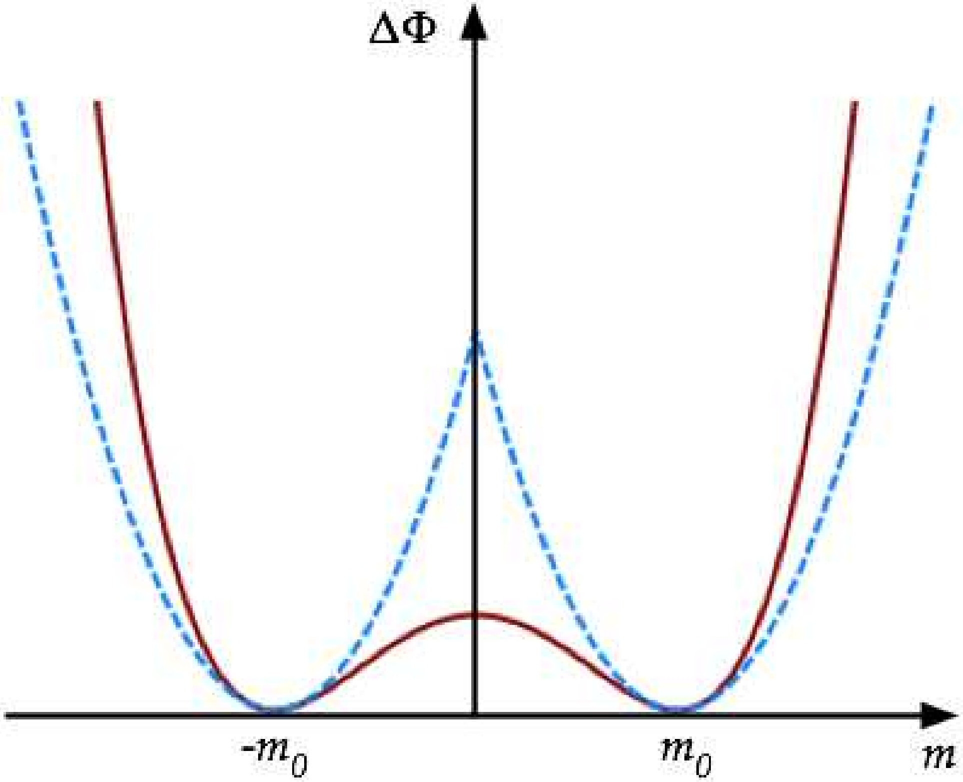

Figure 4.1: The dashed blue line represent the double parabola potential, where m_0 is the bulk magnetization. The Landau-Ginzburg potential is represented by a solid red line to compare.

the equilibrium order parameter profile still is given by the global minimum of the functional Eq. (4.3), we perform the minimization in two steps. First, we consider that the interfacial profile $\ell(\mathbf{x})$ is known. The constrained order parameter profile m_Ξ is obtained by solving the following partial differential equations (PDEs):

$$\nabla^2 m_\Xi = \begin{cases} m_\Xi + m_0 & z > \ell(\mathbf{x}) \\ m_\Xi - m_0 & \psi(\mathbf{x}) < z < \ell(\mathbf{x}) \end{cases} \tag{4.9}$$

subject to the boundary conditions $m_\Xi \to -m_0$ for $z \to \infty$, the condition given by Eq. (4.8) and $m_\Xi = 0$ at $z = \ell(\mathbf{x})$. From the evaluation of the constrained order parameter profile we can get an interfacial Hamiltonian *functional* $\mathcal{H}[\ell]$ by computing the free energy given by Eq. (4.3) associated to m_Ξ:

$$\mathcal{H}[\ell] = \mathcal{F}[m_\Xi] \tag{4.10}$$

As a final stage, the equilibrium order parameter profile is obtained by minimization of $\mathcal{H}$ with respect to the interfacial profile $\ell(\mathbf{x})$. This procedure can be performed exactly for simple geometries, such as when both the substrate and the liquid-vapour interface are planar or spherical [91]. However, in the general case we have to resort to numerical procedures.

Now we will see that, within the double parabola approximation, the functional $\mathcal{H}$ can be reduced to boundary integrals, connecting to the standard interfacial Hamiltonian approaches. First, we note that the PDEs in Eq. (4.9), subject to the corresponding boundary conditions, are independent. Furthermore, by making the change of variables $\delta m_\Xi = m_\Xi \pm m_0$, where the plus sign corresponds to the problem for the vapour phase and the minus sign for the wetting layer, then both PDEs reduce to the Helmholtz equation:

$$\nabla^2 \delta m_\Xi = \kappa^2 \delta m_\Xi \tag{4.11}$$

For the vapour phase region, Eq. (4.11) is solved subject to the boundary conditions that $\delta m_\Xi \to 0$ as $z \to \infty$ and $\delta m_\Xi(\mathbf{s}) = m_0$ for $\mathbf{s} = (\mathbf{x}, \ell(\mathbf{x}))$. On the other hand, in the liquid layer close to the surface, Eq. (4.11) satifies the boundary conditions that $\delta m_\Xi(\mathbf{s}) = -m_0$ for $\mathbf{s} = (\mathbf{x}, \ell(\mathbf{x}))$, and that

$$\partial_{n_\psi} \delta m_\Xi(\mathbf{s}) \;=\; c\,(\delta m_\Xi(\mathbf{s}) - \delta m_s(\mathbf{s})) \tag{4.12}$$

where now $\mathbf{s} = (\mathbf{x}, \psi(\mathbf{x}))$, $\delta m_s = m_s - m_0$ and $\mathbf{n}_\psi$ is the inwards normal. We denote as V_l and V_g the volume occupied by liquid and gas phase, respectively. In each phase region, we can multiply Eq. (4.11) by δm_Ξ and integrate over the corresponding volume V_i (where i is either l or g):

$$\int_{V_i} d\mathbf{r} \frac{\delta m_\Xi \nabla^2 \delta m_\Xi}{2} = \int_{V_i} \frac{\kappa^2}{2} (\delta m_\Xi)^2 \tag{4.13}$$

Now, by using the identity $\delta m_\Xi \nabla^2 \delta m_\Xi + \boldsymbol{\nabla} \delta m_\Xi \cdot \boldsymbol{\nabla} \delta m_\Xi = \boldsymbol{\nabla} \cdot (\delta m_\Xi \boldsymbol{\nabla} \delta m_\Xi)$ and the divergence theorem, we get after some rearrangement that:

$$\int_{V_i} d\mathbf{r} \left\{ \frac{1}{2} \left(\nabla \delta m_\Xi\right)^2 + \frac{\kappa^2}{2} (\delta m_\Xi)^2 \right\} = \oint_{\partial V_i} d\mathbf{s} \frac{(\delta m_\Xi(\mathbf{s}))}{2} (\mathbf{n} \cdot \nabla \delta m_\Xi(\mathbf{s})) \tag{4.14}$$

where ∂V_i is the boundary of the volume V_i. If we add the contributions from the liquid and vapour regions, and taking into account the boundary conditions of each boundary problem, we get that the interfacial Hamiltonian functional can be recast as:

$$\mathcal{H}[\ell] = -\frac{m_0}{2} \int_\ell d\mathbf{s} (q_\ell^+(\mathbf{s}) + q_\ell^-(\mathbf{s})) - \frac{1}{2} \int_\psi d\mathbf{s} \left(\delta m_s(\mathbf{s}) + \frac{1}{c} q_\psi(\mathbf{s}) \right) q_\psi(\mathbf{s}) \tag{4.15}$$

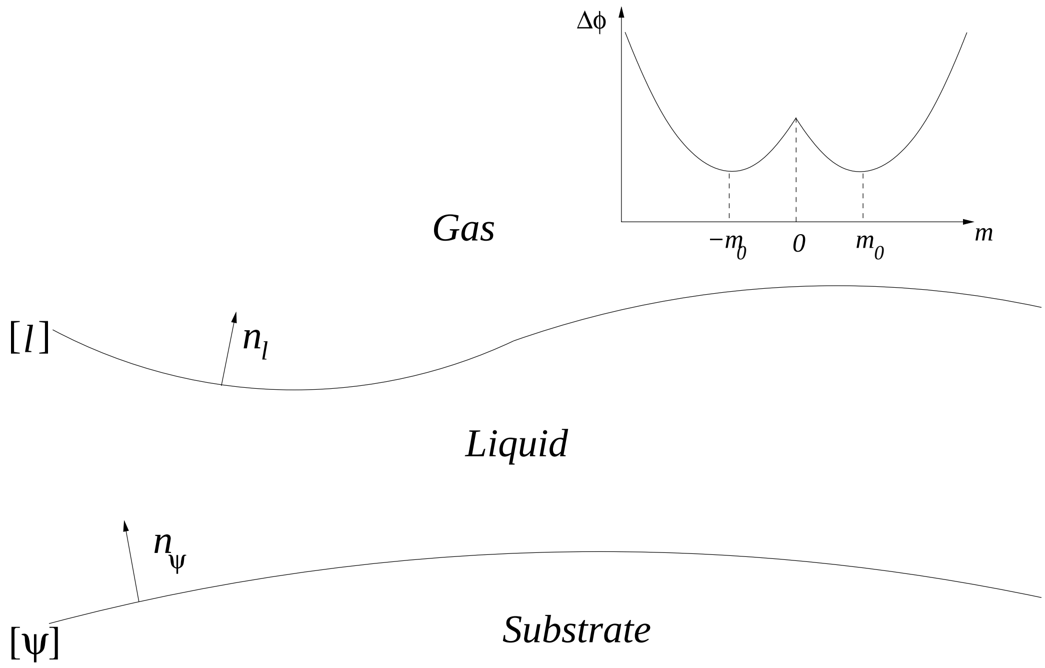

Figure 4.2: Schematic illustration of a typical interfacial configuration. Inset: the double-parabola approximation to $\Delta\phi(m)$.

In this expression, the integrals are performed on the surfaces where $z = \ell(\mathbf{x})$ and $z = \psi(\mathbf{x})$, and $q_i \equiv \mathbf{n}_i \cdot \boldsymbol{\nabla} \delta m_\Xi$, where $\mathbf{n}_\ell$ and $\mathbf{n}_\psi$ are the surfaces normals pointing towards the gas phase (see Fig. 4.2). Finally, the superscript sign corresponds that the normal derivative is evaluated either on the liquid (positive) or gas (negative) side of the gas-liquid interface, respectively. Note that they will be different almost everywhere unless the interfacial profile ℓ corresponds to the equilibrium one.

In order to quantify the interfacial Hamiltonian functional, we need to know the normal derivatives of δm_Ξ on each boundary surface. We will show that their evaluation also reduces to a boundary integral problem. The boundary problems for the order parameter profile in the liquid and gas regions are linear, so formally they can be solved by standard techniques. We use a Green function method. The free space Green function G associated to the Helmholtz equation satisfies

$$\nabla^2_{\mathbf{r}} G(\mathbf{r}, \mathbf{r}_0) - \kappa^2 G(\mathbf{r}, \mathbf{r}_0) = \delta(\mathbf{r} - \mathbf{r}_0) \tag{4.16}$$

where the subscript indicates that the derivatives are performed on the first argument of the Green function. The solution to this problem depends on the dimensionality of the system:

$$G(\mathbf{r},\mathbf{r}_0) \;=\; \begin{cases} \dfrac{e^{-\kappa|\mathbf{r}-\mathbf{r}_0|}}{4\pi|\mathbf{r}-\mathbf{r}_0|} & 3D \\ \\ \dfrac{1}{2\pi}K_0\left(\kappa|\mathbf{r}-\mathbf{r}_0|\right) & 2D \end{cases} \tag{4.17}$$

where K_0 is the modified Bessel function of zero order and second kind [4]. The Green's second identity reads:

$$\begin{aligned} &\delta m_\Xi(\mathbf{r})\nabla^2_{\mathbf{r}}G(\mathbf{r},\mathbf{r}_0) \;-\; G(\mathbf{r},\mathbf{r}_0)\nabla^2 m_\Xi(\mathbf{r}) \\ &= \boldsymbol{\nabla}_{\mathbf{r}}\cdot\left(\delta m_\Xi(\mathbf{r})\boldsymbol{\nabla}_{\mathbf{r}}G(\mathbf{r},\mathbf{r}_0) \;-\; G(\mathbf{r},\mathbf{r}_0)\boldsymbol{\nabla}\delta m_\Xi(\mathbf{r})\right) \end{aligned} \tag{4.18}$$

Substituting Eqs. (4.11) and (4.16) into Eq. (4.18) leads to

$$\delta m_\Xi(\mathbf{r})\,\delta(\mathbf{r}-\mathbf{r}_0) \;=\; \boldsymbol{\nabla}_{\mathbf{r}}\cdot\left(\delta m_\Xi(\mathbf{r})\boldsymbol{\nabla}_{\mathbf{r}}G(\mathbf{r},\mathbf{r}_0) \;-\; G(\mathbf{r},\mathbf{r}_0)\boldsymbol{\nabla}\delta m_\Xi(\mathbf{r})\right) \tag{4.19}$$

If $\mathbf{r_0} \in V_g$, then Eq. (4.19) is integrated over V_g, leading to the following expression for δm_Ξ in the gas region:

$$\delta m_\Xi(\mathbf{r}) \;=\; \int_\ell \big(G(\mathbf{s},\mathbf{r})q_\ell^-(\mathbf{s}) \;-\; m_0\partial_{n_\ell}G(\mathbf{s},\mathbf{r})\big)\,d\mathbf{s} \tag{4.20}$$

where $\partial_{n_\ell} \equiv \mathbf{n}_\ell(\mathbf{s})\cdot\boldsymbol{\nabla}_{\mathbf{s}}$. In a similar way, integration over V_l leads to the expression for $\delta m_\Xi(\mathbf{r})$ if $\mathbf{r} \in V_l$ as:

$$\begin{aligned} \delta m_\Xi(\mathbf{r}) \;=\; &\int_\ell \big(-G(\mathbf{s},\mathbf{r})q_\ell^-(\mathbf{s}) \;-\; m_0\partial_{n_\ell}G(\mathbf{s},\mathbf{r})\big)\,d\mathbf{s} \\ +&\int_\psi \left(G(\mathbf{s},\mathbf{r})q_\psi(\mathbf{s}) \;-\; \left(\delta m_s(\mathbf{s}) + \frac{1}{c}q_\psi(\mathbf{s})\right)\partial_{n_\psi}G(\mathbf{s},\mathbf{r})\right)\,d\mathbf{s} \end{aligned} \tag{4.21}$$

where $\partial_{n_\psi} \equiv \mathbf{n}_\psi(\mathbf{s})\cdot\boldsymbol{\nabla}_{\mathbf{s}}$. Eqs. (4.20) and (4.21) cannot be used to get the boundary values. However, we can use a trick to modify these equations to be valid on the boundary. First, we place $\mathbf{r}$ at a boundary point $\mathbf{s}$ *and* deform this boundary around it by cutting a circular hole of radius ϵ and adding an hemispherical cap Γ_ϵ on top of that, so the point is again inside the corresponding region. For small ϵ, the contribution of Γ_ϵ to the boundary integrals is approximately

$$\int_{\Gamma_\epsilon} \left(G(\mathbf{s}_0,\mathbf{s})q(\mathbf{s}_0) \;-\; \delta m\partial_n G(\mathbf{s}_0,\mathbf{s})\right)\,d\mathbf{s}_0 = \frac{\delta m}{2} + \mathcal{O}(\epsilon) \tag{4.22}$$

So, in the limit $\epsilon \to 0$, we obtain the following set of integral equations:

$$
\begin{aligned}
\frac{m_0}{2} &= \int_\ell \left(G(\mathbf{s}_0,\mathbf{s})q_\ell^-(\mathbf{s}_0) \;-\; m_0\partial_{n_\ell}G(\mathbf{s}_0,\mathbf{s})\right)\, d\mathbf{s}_0 \qquad (4.23)\\
-\frac{m_0}{2} &= \int_\ell \left(-G(\mathbf{s}_0,\mathbf{s})q_\ell^+(\mathbf{s}_0) \;-\; m_0\partial_{n_\ell}G(\mathbf{s}_0,\mathbf{s})\right)\, d\mathbf{s}_0\\
+\int_\psi \Bigg(G(\mathbf{s}_0,\mathbf{s})q_\psi(\mathbf{s}_0) &- \left(\delta m_s(\mathbf{s}_0) + \frac{1}{c}q_\psi(\mathbf{s}_0)\right)\partial_{n_\psi}G(\mathbf{s}_0,\mathbf{s})\Bigg)\, d\mathbf{s}_0 \qquad (4.24)\\
\frac{\delta m_s(\mathbf{s})}{2} + \frac{1}{2c}q_\psi(\mathbf{s}) &= \int_\ell \left(-G(\mathbf{s}_0,\mathbf{s})q_\ell^+(\mathbf{s}_0) \;-\; m_0\partial_{n_\ell}G(\mathbf{s}_0,\mathbf{s})\right)\, d\mathbf{s}_0\\
+\int_\psi \Bigg(G(\mathbf{s}_0,\mathbf{s})q_\psi(\mathbf{s}_0) &- \left(\delta m_s(\mathbf{s}_0) + \frac{1}{c}q_\psi(\mathbf{s}_0)\right)\partial_{n_\psi}G(\mathbf{s}_0,\mathbf{s})\Bigg)\, d\mathbf{s}_0 \qquad (4.25)
\end{aligned}
$$

where the integrals represent their Cauchy principal values. These equations will allow us to obtain the fields q_ℓ^+, q_ℓ^- and q_ψ, and after substitution into Eq. (4.15), the value of $\mathcal{H}$.

To finish this Section, we will discuss how to study the interfacial phenomenology within the double parabola approach under off-coexistence conditions. As in the Landau-Ginzburg case, the effect of the ordering field h on the Landau potential comes through an extra term $-hm$ on $\Delta\phi$. After some algebra, we see that the Landau potential can be written as:

$$
\frac{\kappa^2}{2}(|m| - m_0)^2 - hm = \frac{\kappa^2}{2}\left[m \pm m_0 - \frac{h}{\kappa^2}\right]^2 \pm hm_0 - \frac{h^2}{2\kappa^2} \qquad (4.26)
$$

where the plus sign corresponds to the gas phase, and the minus sign to the liquid. As this potential is also a double parabola, now we can generalise all the results we obtained before for the off-coexistence case. In particular, if we change m_0 by $m_0 - h/\kappa^2$ in the equations for the constrained order parameter profile in the gas region, and in the liquid region m_0 is substituted by $m_0 + h/\kappa^2$ and $\delta m_s = m_s - m_0 - h/\kappa^2$, then Eqs. (4.23), (4.24) and (4.25) are modified to:

$$\frac{1}{2}\left(m_0 - \frac{h}{\kappa^2}\right) = \int_\ell \left(G(\mathbf{s}_0, \mathbf{s}) q_\ell^-(\mathbf{s}_0) \,-\, \left(m_0 - \frac{h}{\kappa^2}\right) \partial_{n_\ell} G(\mathbf{s}_0, \mathbf{s}) \right) d\mathbf{s}_0 \tag{4.27}$$

$$\begin{aligned} -\left(m_0 + \frac{h}{\kappa^2}\right) \;=\; & \int_\ell \left(-G(\mathbf{s}_0, \mathbf{s}) q_\ell^+(\mathbf{s}_0) \,-\, \left(m_0 + \frac{h}{\kappa^2}\right) \partial_{n_\ell} G(\mathbf{s}_0, \mathbf{s}) \right) d\mathbf{s}_0 \\ & + \int_\psi \left(G(\mathbf{s}_0, \mathbf{s}) q_\psi(\mathbf{s}_0) \,-\, \left(\delta m_s(\mathbf{s}_0) + \frac{1}{c} q_\psi(\mathbf{s}_0)\right) \partial_{n_\psi} G(\mathbf{s}_0, \mathbf{s}) \right) d\mathbf{s}_0 \end{aligned} \tag{4.28}$$

$$\begin{aligned} \frac{\delta m_s(\mathbf{s})}{2} + \frac{1}{2c} q_\psi(\mathbf{s}) \;=\; & \int_\ell \left(-G(\mathbf{s}_0, \mathbf{s}) q_\ell^+(\mathbf{s}_0) \,-\, \left(m_0 + \frac{h}{\kappa^2}\right) \partial_{n_\ell} G(\mathbf{s}_0, \mathbf{s}) \right) d\mathbf{s}_0 \\ & + \int_\psi \left(G(\mathbf{s}_0, \mathbf{s}) q_\psi(\mathbf{s}_0) \,-\, \left(\delta m_s(\mathbf{s}_0) + \frac{1}{c} q_\psi(\mathbf{s}_0)\right) \partial_{n_\psi} G(\mathbf{s}_0, \mathbf{s}) \right) d\mathbf{s}_0 \end{aligned} \tag{4.29}$$

Now, the interfacial Hamiltonian functional has two contributions: a boundary integral term similar to Eq. (4.15), and a bulk term associated to the free energy difference between the two local minima of $\Delta\phi$. So, up to an irrelevant overall constant, the interfacial Hamiltonian functional can be written as:

$$\begin{aligned} \mathcal{H}[\ell] = & -\frac{1}{2} \int_\ell d\mathbf{s} \left[\left(m_0 + \frac{h}{\kappa^2}\right) q_\ell^+(\mathbf{s}) + \left(m_0 - \frac{h}{\kappa^2}\right) q_\ell^-(\mathbf{s}) \right] \\ & -\frac{1}{2} \int_\psi d\mathbf{s} \left(\delta m_s(\mathbf{s}) + \frac{1}{c} q_\psi(\mathbf{s}) \right) q_\psi(\mathbf{s}) - 2 h m_0 \int d\mathbf{x} (\ell(\mathbf{x}) - \psi(\mathbf{x})) \end{aligned} \tag{4.30}$$

4.3 Methodology

In order to obtain numerically the equilibrium interfacial profile, we have seen in the previous Section that first we have to evaluate the interfacial Hamiltonian functional from a constrained minimization of the free energy functional Eq. (4.3). This can be done after solving the integral equations set Eqs. (4.23), (4.24) and (4.25). The method used to solve this set of integral equations is the *Boundary Element Method* (BEM) [61, 108] based on the discretization of the boundary. The BEM constitutes a powerful numerical technique for solving elliptic partial differential equations, such as the Laplace equation or the Helmholtz equations. Its application requires the so-called *fundamental solution* (i.e. the associated free space Green function) and its implementation results in a set of linear equations for linear PDEs. The BEM has certain advantages over the finite-element methods, as the discretization is done only over the boundary of the system, which makes the numerical modeling easier. On the other hand, they can be applied easily to infinite domains. However, the coefficient matrix of the set linear of equations is not sparse and in general non-symmetric.

As in the previous Chapter, we will study the adsoption on sinusoidal substrates within the mean-field approach. Thus, we will assume that our solutions are periodic across the x direction, and they are translationally invariant along the groove axis y. Thus, we will reduce our study to a 2D cross section of a period length subject to periodic boundary conditions along the x axis. However, by doing this the Green function we have to use is no longer the 3D Yukawa potential, but the 2D Green function for the Helmholtz equation. This is consistent with the fact that:

$$K_0(x) = \int_0^\infty dy \frac{e^{-\sqrt{x^2+y^2}}}{\sqrt{x^2+y^2}} \tag{4.31}$$

We set $m_0 = 1$ and $\kappa = 1$, and we will restrict ourselves to the case $c > 1$. Under these circumstances, there is a critical wetting transition at $m_s = 1$. Moreover, close enough to the wetting transition, the order parameter value on the surface is always positive, so the liquid-vapour interface does not cross the substrate. The latter situation can also be studied by this method, but requires moving boundaries techniques which go beyond the present application. For simplicity we will focus on the equations under bulk coexistence conditions, i.e. $h = 0$. For off-coexistence we can modify them in a similar way as discussed by the end of the previous Section. We will use the constant boundary element method, where the boundaries are discretized in a set of straight elements called boundary elements. In each element, we define a node placed at the midpoint of the segment. We assume that both δm_Ξ and q are constants along each boundary element. Higher order approaches have been used in the literature [61]. If we define:

$$G_{ij} = \int_{\Gamma_i} d\mathbf{s} G(\mathbf{s}, \mathbf{s}_j) \qquad H_{ij} = \int_{\Gamma_i} d\mathbf{s} \partial_{n_i} G(\mathbf{s}, \mathbf{s}_j) \tag{4.32}$$

where Γ_j is the boundary element i with an associated node $\mathbf{s}_i$, then Eqs.

(4.23), (4.24) and (4.25) can be approximated as:

$$\frac{1}{2} = \sum_{i=1}^{N_\ell} \left(G_{ij} q_i^- \, - \, H_{ij} \right) \qquad j \, = \, 1, \ldots, N_\ell \quad (4.33)$$

$$-\frac{1}{2} = \sum_{i=1}^{N_\ell} \left(-G_{ij} q_i^+ \, - \, H_{ij} \right) \sum_{i=N_\ell+1}^{N_\ell+N_\psi} G_{ij} q_i - \left(\delta m_s + \frac{1}{c} q_i \right) H_{ij} \quad (4.34)$$

$$j = 1, \ldots, N_\ell$$

$$\frac{\delta m_s}{2} + \frac{q_j}{2c} = \sum_{i=1}^{N_\ell} \left(-G_{ij} q_i^+ \, - \, H_{ij} \right) \sum_{i=N_\ell+1}^{N_\ell+N_\psi} G_{ij} q_i - \left(\delta m_s + \frac{1}{c} q_i \right) H_{ij} \quad (4.35)$$

$$j = N_\ell + 1, \ldots, N_\ell + N_\psi$$

where N_ℓ and N_ψ are the number of boundary elements on the gas-liquid interface and the substrate surface, respectively. So, these equations are a set of linear equations where the unknowns are the $2N_\ell + N_\psi$ values of q on each boundary element.

The coefficients in Eq. (4.32) can be evaluated by using the Gauss-Legendre quadrature formula:

$$\int_{-1}^{1} f(\xi) \, d\xi \, = \, \sum_{k=1}^{m} \omega_k \, f(\xi_k) \qquad (4.36)$$

where f is an arbitrary function defined on the interval $[-1, 1]$. The values of ξ_k are the roots of the Legendre polynomial $P_m(x)$, and their associated weights are $\omega_k = 2/[(1 - \xi_k^2)(P'_m(\xi_k))^2]$ [109]. In this work, the typical value of m was $m = 8$, although to check accuracy $m = 16$ was also considered in some cases. In order to use this formula in Eq. (4.32), we parametrize the boundary element by a variable ξ:

$$x \, = \, \frac{x_i^2 + x_i^1}{2} \, + \, \frac{x_i^2 - x_i^1}{2} \xi \qquad z \, = \, \frac{z_i^2 + z_i^1}{2} \, + \, \frac{z_i^2 - z_i^1}{2} \xi \qquad (4.37)$$

where (x_i^1, z_i^1) and (x_i^2, z_i^2) are the left and right extreme points, respectively, of the boundary element i, with a length l_i. Then

$$G_{ij} \, = \, \frac{l_i}{2} \int_{-1}^{1} d\xi \frac{K_0(\kappa r(\xi))}{2\pi} \approx \sum_{k=1}^{m} \frac{l_i}{2} \frac{1}{2\pi} K_0 \left(\kappa \, r \left(\xi_k \right) \right) \omega_k \qquad (4.38)$$

where $r\left(\xi\right) \, = \, \sqrt{\left(x(\xi) - x_j\right)^2 + \left(z(\xi) - z_j\right)^2}$. In a similar way, and taking into account that:

$$\partial_n G(\mathbf{s}_i, \mathbf{s}_j) = -\kappa \frac{\mathbf{n} \cdot (\mathbf{s}_i - \mathbf{s}_j)}{|\mathbf{s}_i - \mathbf{s}_j|} K_1(\kappa |\mathbf{s}_i - \mathbf{s}_j|) \qquad (4.39)$$

where $K_1(x)$ is the modified Bessel function of order 1 and second kind [4], the matrix element H_{ij} reads:

$$H_{ij} = \frac{-\kappa}{4\pi} \sum_{k=1}^{m} \omega_k \left[-(z_i^2 - z_i^1)(x(\xi_k) - x_j) + (x_i^2 - x_i^1)(z(\xi_k) - z_j) \right] \frac{K_1\left(\kappa\, r\left(\xi_k\right)\right)}{r\left(\xi_k\right)} \tag{4.40}$$

The discretized version of the interfacial Hamiltonian is given by the following expression:

$$\mathcal{H}(z_1^1, \ldots, z_{N_\ell}^1) = -\frac{1}{2} \sum_{i=1}^{N_\ell} l_i (q_i^+ + q_i^-) - \frac{1}{2} \sum_{i=N_\ell+1}^{N_\ell+N_\psi} \left(\delta m_s + \frac{q_i}{c} \right) l_i q_i \tag{4.41}$$

where the shape of the liquid-vapour interface is completely determined by the heights z_i^1, with $i = 1, \ldots, N_\ell$. For latter purporses, we also need the gradient of $\mathcal{H}$. Note that the energy depends on the values of z_i^1 through the normal derivatives q, as well as the lengths of the boundary elements. In order to obtain the derivatives of q with respect to z_i^1, we rewrite Eqs. (4.33), (4.34) and (4.35) in a matrix form:

$$\mathbf{A} \cdot \mathbf{q} = \mathbf{b} \tag{4.42}$$

where both $\mathbf{A}$ and $\mathbf{b}$ are functions of the set $\{z_i\}$, and $\mathbf{q}$ is a vector with the $2N_\ell + N_\psi$ values q_i as components. If we displace z_i^1 by a small amount δz, then $\mathbf{A}$ and $\mathbf{b}$ change to $\mathbf{A} + \delta\mathbf{A}$ and $\mathbf{b} + \delta\mathbf{b}$, respectively. So, the solution to the new set of linear equations can be written as $\mathbf{q} + \delta\mathbf{q}$, which satisfy:

$$(\mathbf{A} + \delta\mathbf{A}) \cdot (\mathbf{q} + \delta\mathbf{q}) = \mathbf{b} + \delta\mathbf{b} \tag{4.43}$$

Up to first order in $\delta\mathbf{q}$, this equation can be recast as:

$$\mathbf{A} \cdot (\delta\mathbf{q}) = \delta\mathbf{b} - (\delta\mathbf{A}) \cdot \mathbf{q} \tag{4.44}$$

If we divide this equation by δz, and make the limit $\delta z \to 0$, we arrive to the following equation:

$$\mathbf{A} \cdot \left(\frac{\partial \mathbf{q}}{\partial z_i^1} \right) = \frac{\partial \mathbf{b}}{\partial z_i^1} - \left(\frac{\partial \mathbf{A}}{\partial z_i^1} \right) \cdot \mathbf{q} \tag{4.45}$$

This provides a new set of linear differential equations for the gradient of $\mathbf{q}$, as the value of $\mathbf{q}$ is known. Although there are analytical expressions for the right-hand side of this equation, we evaluate numerically the corresponding derivatives. On the other hand, as the coefficient matrix for the evaluation of the values of q and their derivatives is the same, the solution of the corresponding sets of linear equations is done by using the LU decomposition method [109], reducing considerably the computational time.

Once we have a procedure to get the interfacial Hamiltonian, we find the equilibrium interfacial profile by minimizing numerically the Eq. (4.41) with respect to the set $\{z_i\}$. We use a modification of the Conjugate Gradient Method shown in the Appendix. This is motivated by the fact that, for certain configurations where the liquid-vapour interface locates close to the substrate, the standard Conjugate Gradient Method becomes unstable as the coefficient matrix $\mathbf{A}$ is singular for these particular configurations. This problem can be solved by refining the boundary mesh, but this solution becomes impractical above certain number of boundary elements. Alternatively, in most of the cases this problem has been avoided by a modification of the Conjugated Gradient algorithm: in each step i, instead of moving to the minimum along the line in the direction of $\mathbf{g}_i$, the modified algorithm stays closer to the original point (usually at a distance which is about $50-80\%$ of the distance to the line minimum). In this way, the interfacial updates are smoother and, although it takes longer to reach the global minimum, this is found within a good accuracy (usually with gradient norms less than 10^{-7}). Nevertheless, problems are still observed for low values of m_s. As a consequence, the interfacial phenomenology for large roughness in the substrate is difficult to obtain numerically. This is still an issue in our approach that needs to be solved.

4.4 Numerical results

Our numerical calculations where performed for $c=\infty$. In this way, we can compare our results for the double-parabola problem with those obtained within the Landau-Ginzburg (LG) framework. Due to the numerical difficulties we mentioned in the previous Section, we have considered only three different values of the substrate roughness: $A/L=0.5$, 1 and 1.5, with values of L spanning from $L \approx 10$ to $L=50$. We apply the boundary element method with $N_\ell = N_\psi = 100$ for $A/L=0.5$, 250 for $A/L=1$ and 350 for $A/L=1.5$, although under some circumstances a larger number of elements was needed for $A/L \geq 1$. For each substrate geometry, we obtain the different branches of interfacial states D, F, and W on a wide range of values of the surface coupling for the bulk ordering field $h=0$, and the off-coexistence filling transition $h<0$. In order to improve convergence, in each branch we use as initial condition for each value of m_s the output of the previous minimization. The true equilibrium state will be the state that

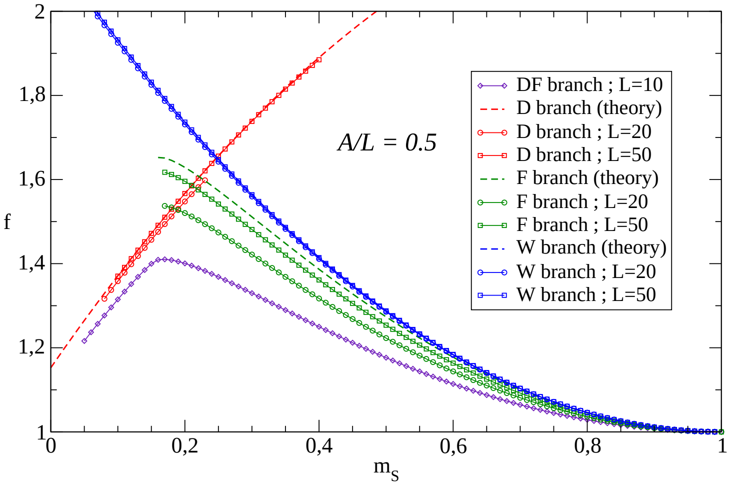

Figure 4.3: Plot of the free energy densities of the different branches of interfacial states for $c = \infty$ at $h = 0$, as a function of the surface magnetization m_s, for a sinusoidal substrate with $A/L = 0.5$, and $L = 10$ (diamonds), $L = 20$ (open circles) and $L = 50$ (open squares). The D states branch corresponds to the green (lighter grey) symbols, the W states branch to the blue (dark grey) symbols and the F states branch to the red (light grey) symbols. For comparison, the theoretical prediction from (4.49), (4.50) and (4.51) are also represented as dashed lines (the colour code is the same as for the numerical results).

gives the least free energy at the same thermodynamic conditions, and the crossing between the different free-energy branches will correspond to the phase transitions.

4.4.1 Results for $h = 0$

In order to compare the minimization results with the macroscopic theory, we have obtained the analytical expression for the free-energy densities, using the relevant surface tensions of the double parabola (DP) model. For a flat substrate in contact with a bulk liquid phase, Eq. (4.11) can be written as:

$$\frac{d^2\delta m}{dz^2} = \kappa^2 \delta m \tag{4.46}$$

with the boundary conditions that $\delta m(z \to \infty) = 0$ and $\delta m(0) = m_s - m_0$. The solution is $m(z) = m_0 + (m_s - m_0)e^{-\kappa z}$. Substitution of this solution into Eq. (4.3) leads to a free energy per unit area equal to $\kappa(m_s - m_0)^2/2$. So, taking into account that in our units $\kappa = 1$ and $m_0 = 1$, then $\sigma_{lw} =$

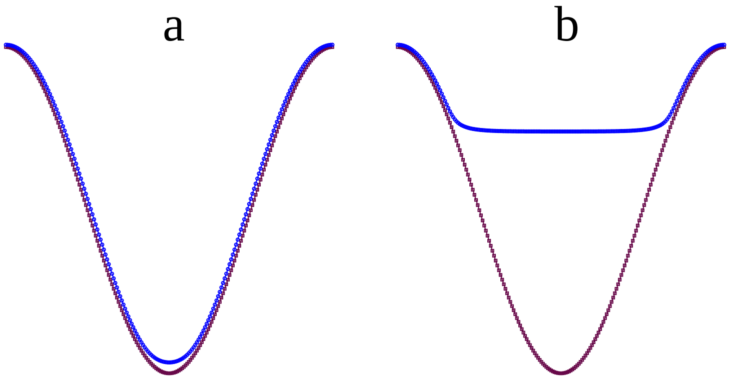

Figure 4.4: Liquid-vapour interfacial profile for: (a) the D state and (b) the F state at coexistence ($h = 0$) in the filling transition for $c = \infty$, $A/L = 0.5$ and $L = 20$, with $N_\ell = N_\psi = 200$.

$(m_s - 1)^2/2$. For the liquid-vapour interface, we have to solve two uncoupled Helmholtz equations Eq. (4.46). For $z > 0$ (gas phase), we have the boundary conditions $\delta m(z \to \infty) = 0$ and $\delta m(0) = m_0$. For the liquid phase, i.e. $z < 0$, $\delta m(0) = -m_0$ and $\delta m(z \to -\infty) = 0$. So, the solution is $m(z) = m_0(1 - e^{-\kappa|z|})(z/|z|)$, which when substituted into Eq. (4.3) leads to $\sigma_{lv} = \kappa m_0^2 = 1$ in our units.

Finally, for the gas-substrate surface tension, we recall that a liquid layer of width ℓ intrudes between the bulk gas and the substrate. As a consequence, we have to solve again two uncoupled Helmholtz equations Eq. (4.46). In the gas phase $z > \ell$, we have similar boundary conditions as for the free interface situation. So, $m(z > \ell) = m_0(1 - e^{-\kappa(z-\ell)})$. On the other hand, for $0 < z < \ell$ (liquid layer) we have the boundary conditions that $m(0) = m_s$ and $m(\ell) = 0$. The solution to this problem is:

$$m(z) = m_0 - m_0 \frac{\sinh \kappa z}{\sinh \kappa \ell} + (m_s - m_0)\frac{\sinh \kappa(\ell - z)}{\sinh \kappa \ell} \tag{4.47}$$

By using Eq. (4.15), we find that the free energy per unit area associated to the constrained interfacial configuration is:

$$\frac{\mathcal{H}}{\mathcal{A}}(\ell) = \frac{\kappa}{2\sinh \kappa\ell}\left[\left(m_0^2 + (m_s - m_0)^2\right)\cosh \kappa\ell + 2m_0(m_s - m_0)\right] + \frac{\kappa m_0^2}{2} \tag{4.48}$$

We find ℓ by minimizing $\mathcal{H}$ as a function of ℓ, which leads to $\kappa\ell = -\log[(m_0 - m_s)/m_0]$. Note that this result is also recovered if continuity is imposed on the derivative of the order parameter profile at $z = \ell$ on both sides of the liquid-vapour interface. Substitution of the equilibrium value of ℓ on Eq.

(4.48) allows as to identify the gas-substrate surface tension as $\kappa^2(m_0^2/2 + m_0 m_s - m_s^2/2) = (1/2 + m_s - m_s^2/2)$ in our units. Thus the contact angle θ, defined through Young equation, satisfies $\cos\theta = 2m_s - m_s^2$. Substitution of the expressions of the surface tensions in Eqs. (3.5), (3.6) and (3.11) yield to:

$$\begin{aligned}
f^D &= \frac{2}{\pi}\left(\frac{1}{2} + m_s - \frac{m_s^2}{2}\right) E(-(qA)^2) && (4.49)\\
f^F &= 1 - \frac{\beta}{\pi} \\
&+ \frac{2}{\pi}\left(\frac{1}{2} + m_s - \frac{m_s^2}{2}\right) E(-(qA)^2) && (4.50)\\
&- \frac{1}{\pi}\left(2m_s - m_s^2\right) E\left(\pi - \beta| - (qA)^2\right) \\
\text{with} \quad & \beta = \pi - qx_c = \arcsin\left(\frac{1}{qA}\sqrt{\frac{1}{(2m_s - m_s^2)^2} - 1}\right) \\
f^W &= 1 + \frac{2}{\pi}\left(\frac{1}{2} - m_s + \frac{m_s^2}{2}\right) E(-(qA)^2) && (4.51)
\end{aligned}$$

Figure 4.3 shows the comparison between the theoretical predictions for the free energy density associated to each branch and the numerical values obtained by minimizing the DP functional for $A/L = 0.5$. Typical interfacial profiles for D and F states are shown in Fig. 4.4. For small values of L the filling transition disappears as a continuous crossover between D and F states, in a similar way as in the LG model. As L increases the filling transition emerges as the D and F branches split, and they approach to the macroscopic predictions for L large enough. On the other hand, the W branch is always metastable in the range $m_s \in [0, 1]$, and touches tangentially the F branch at $m_s = 1$. This implies that the wetting transition at the rough substrates is always second order, in agreement with the predictions of interfacial Hamiltonian theories [114, 117, 118]. A similar behaviour was observed for rougher substrates, so we will focus on the filling transition and its dependence on L.

Figure 4.5 shows the adsoption phase diagram at $h = 0$ with different values of A/L. As in the LG model, the wetting transition is unshifted respect to the planar substrate transition value $m_s = 1$. On the other hand, the values of m_s at the filling transition have qualitatively a similar L dependence to the LG model, but they show quantitative differences. In order to make a closer comparison of the numerical results obtained from the DP and LG model, we plotted the value of the contact angle θ at the filling transition for both models. For a given roughness and large values of L the DP models

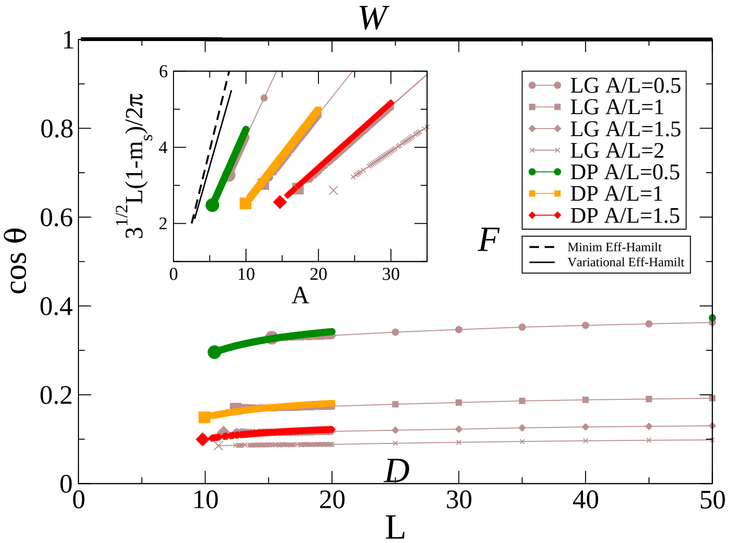

Figure 4.5: Adsorption phase diagram on a sinusoidal substrate with $c = \infty$ and $h = 0$. The phase boundaries between D and F states (DP model) are plotted for $A/L = 0.5$ (green circles), $A/L = 1$ (orange squares), $A/L = 1.5$ (red diamonds), LG model (grey lines and symbols) (the lines serve only as guides for the eyes), and the big symbols to the filling transition critical points. Finally the wetting transition is represented by the thick continuous line for $m_s = 1$. Inset: plot of $\Delta\tilde{T} = \sqrt{3}L(1 - m_s)/(2\pi)$ as a function of the substrate amplitude A along the filling transition line. The meaning of the symbols is the same as in the main plot. The black lines correspond to the predictions from interfacial Hamiltonian theories [114, 117, 118].

shows identical behaviour to the LG case, with a $\cos\theta$ value of the filling transition slightly higher, and closer to the value of the transition in the macroscopic theory. Furthermore, by increasing the values of the roughness, the filling transition equally shifts towards lower values of $\cos\theta$. When L decreases, the filling transition for the DP disappears at a critical point which, for a given roughness, appears at lower values of L and $\cos\theta$ than in the LG model. Finally, the L-dependence of the filling transition value of $\cos\theta$ close to the critical point is sharper in the DP model than in the LG model.

When comparing our numerical calculations with the interfacial Hamiltonian predictions, we have observed similar discrepancies as for the LG model on the dependence of the rescaled temperature with L. However, we cannot rule out the possibility that they converge to the interfacial Hamiltonian prediction for low roughness substrates. If this is the case, the DP predictions are closer to this asymptotics than those obtained within the LG model.

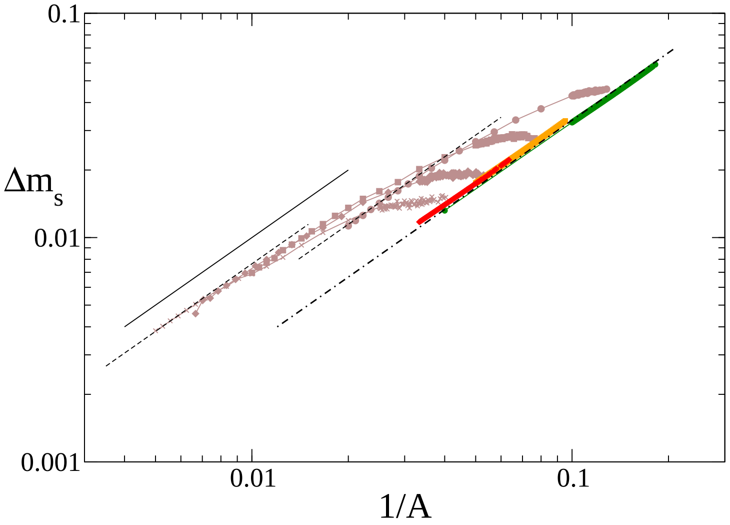

Figure 4.6: Plot of the filling transition shift $m_s^{macro} - m_s$ as a function of $1/A$, for $A/L = 0.5$ (circles), $A/L = 1$ (squares), $A/L = 1.5$ (diamonds) and LG model curves (grey). The dotted-dashed line correspond a linear fit for the transition values with slope 3.

In order to characterize the dependence on L of the filling transition, we plot in Fig. 4.6 the deviation of m_s at the filling transition with respect to the macroscopic prediction m_s^{macro} as a function of A. As we argued for the LG model, the deviation Δm_s for large L is driven by the line tensions B associated to the contact lines where the liquid-vapour interface touches the substrate. Proceeding in a similar way as we did for the LG model, the free-energy difference between the F and D states can be approximated as

$$f_F - f_D \approx -\frac{4l_F}{L}(m_s - m_s^{macro}) + \frac{B}{L} = 0 \tag{4.52}$$

where the first contribution stems from a linear approximation in Δm_s of Eq. (3.9). Since $l_F \approx 1.68\,A$, then $m_s^{macro} - m_s \propto 1/A$, independent of A/L. However, Fig. 4.6 shows that this relationship remains valid for relatively small values of A, unlike in the LG model, where this expression breaks down for intermediate values of A.

Finally, figure 4.7 shows the mid-point interfacial height of the D and F (l_D and l_F, respectively) at the filling transition as functions of L and A. Comparing the DP and LG models, we confirm some of discrepancies observed above in the phase diagram. Away from the filling critical points, l_F for the DP model is slightly closer to the macroscopic prediction than the corresponding values for the LG model. In order to obtain the critical values we have followed the same procedure as in the LG model. By increasing A/L, the critical value of L is quickly stabilized, so that the range of critical values for L and l, for the DP model, are smaller than the corresponding ones for the LG model. Regarding the critical values of A, we see that in both models that they increase almost linearly with the substrate roughness.

4.4.2 Results for $h < 0$

Now, we focus on the off-coexistence interfacial phase diagram. More specifically, we will only consider $h < 0$ extension of the filling transition, as the wetting transition is always continuous at $h = 0$ and consequently there is no prewetting line. Fig. 4.8 shows the typical interfacial profiles for the coexisting D and F states at filling. Note that the liquid-vapour interface shows some curvature above the filled region for the F state. From a qualitative point of view, the picture is similar to the observed within the LG model: for a given L, the filling transition line only exists when the roughness is larger than the corresponding one for critical filling at $h = 0$. The transition line starts at the filling transition obtained at bulk coexistence, and extends beyond coexistence for higher values of m_s up to a critical point. However, there are quantitative differences. In order to compare in a better way the prediction from the DP and LG model, we represent the filling transition value of the contact angle (which is a measure of m_s) as a function of the macroscopic interfacial curvature for the F state, which from Young-Laplace equation is $R^{-1} = 2|h|$ in our units. Figure 4.9 shows the phase diagram for the cases $L = 20$ and $L = 50$ with $A/L = 0.5$ and 1. This small range the roughness is a consequence of the numerical issues we face for larger values of A/L. For the same values of A and L, in this representation the filling transition lines are very similar for both models. However, we observe that the critical parameters for the DP model are larger than for the LG model. Further work is needed to check if this is general feature and it is not restricted to the considered cases.

Figure 4.10 shows the midpoint interfacial heights l_D and l_F, corresponding to the D and F states, respectively, along the off-coexistence filling transition. In order to compare with the macroscopic prediction, we plot l/A as functions of $L/(2\pi R)$. Focusing on the roughness value $A/L = 0.5$, we can see that the critical points of the filling transition still have a midpoint interfacial height larger than the bulk correlation length, and shows a better convergence with the macroscopic theory than the LG model values when L is increased. However, if we look the curves for $A/L = 1$, we observe no significant deviations for l_F for small values of $|h|$ between the DP and LG models. Nevertheless, the critical values of $|h|$ for the DP model are higher and the values of l_D are totally different from the LG model, converging rapidly to the macroscopic values when L is increased.

4.4.3 Summary

In this Chapter we have studied the fluid adsorption phenomenology on sinusoidal substrates within the mean-field approximation by using the DP model, and we have compared it with the predicted within the LG model. We have developed a numerical method to minimize the free-energy functional associated to the DP model, which is based on the Boundary Element Method used for engineering applications. As a benchmark, we have considered the infinite enhancement parameter case, so the substrate promotes second-order wetting transitions, and the values of the roughness parameter are in the range $0.5 \leq A/L \leq 1.5$. From a qualitative point of view, the results obtained from the DP model are consistent with those already reported for the LG model. As for the latter, the wetting transition is always of second order independently of the L and A/L values, so we have centered our study in the filling transition for $h \leq 0$. At $h = 0$ and large L the value of m_s at the transition is slightly below the macroscopic prediction, while for small L the filling transition ends at critical point, for a value of m_s which decreases with increasing A/L. The scaling predicted from interfacial Hamiltoniani theories [114, 117, 118] also breaks down as for the LG model. The filling transition extends off-coexistence ending up at a critical point. Although there are quantitative differences, we find that when the phase diagram is represented in the appropriate variables (contact angle and off-coexistence interfacial curvature) they are much more similar. However, we still have noted some discrepancies with the LG model. At $h = 0$, we have seen a better convergence away from the critical point with the predictions of the macroscopic theory for all values of A/L. On the other hand, the critical values of the midpoint interfacial height, L and $\cos\theta$ are smaller for the DP model than for the LG model. For $h < 0$, the phase diagram shows the filling transition line extends to larger values of interfacial curvature and contact angle for the DP than for the LG model. The midpoint interfacial heights are also closer to the macroscopic values.

Finally, this comparison between the two models of potential has allowed us to check that the DP model can be regarded as a fairly good approximation for the LG model for the mean-field interfacial phase diagram, if the latter is represented in the appropriate thermodynamic variables. So, it would be an excellent test for the performance of perturbative non-local models to predict the adsorption phase diagram of liquids on rough substrates.

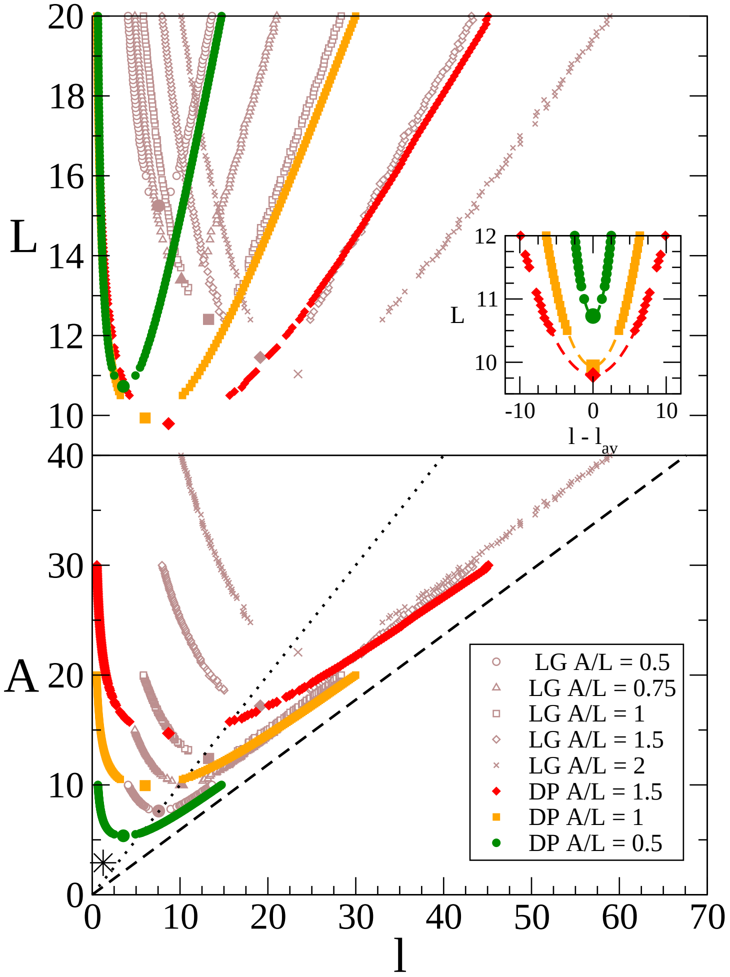

Figure 4.7: Plot of the mid-point interfacial height l of the coexisting D and F states at the filling transition for $h = 0$ as a function of L (top) and A (bottom) close to its critical point, for $A/L = 0.5$ (circles), $A/L = 1$ (squares), $A/L = 1.5$ (diamonds) and curves of the LG model (grey). The star in the bottom panel corresponds to the location of the filling critical point predicted for shallow substrates from the interfacial Hamiltonian approach [117], and the dashed and dotted lines in the bottom panel are the mid-point interfacial height of the F state predicted from the macroscopic theory for large A/L at the filling transition and the spinodal line of the F states, respectively. Inset: plot of the deviations of the mid-point interfacial height of the D and F states at the filling transition for $h = 0$ with respect to their average value (the meaning of the symbols is the same as in the main panel).

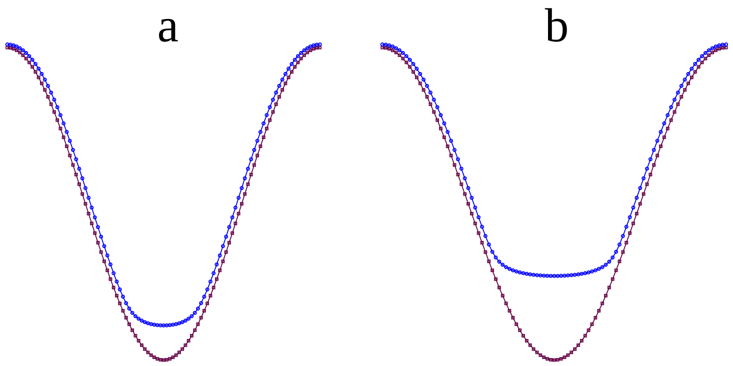

Figure 4.8: Liquid-vapour interfacial profiles corresponding to the coexisting D and F states at the filling transition ((a) and (b), respectively) for $h = -0.03$ for $c = 0$, $A/L = 0.5$ and $L = 20$, with $N_\ell = N_\psi = 100$.

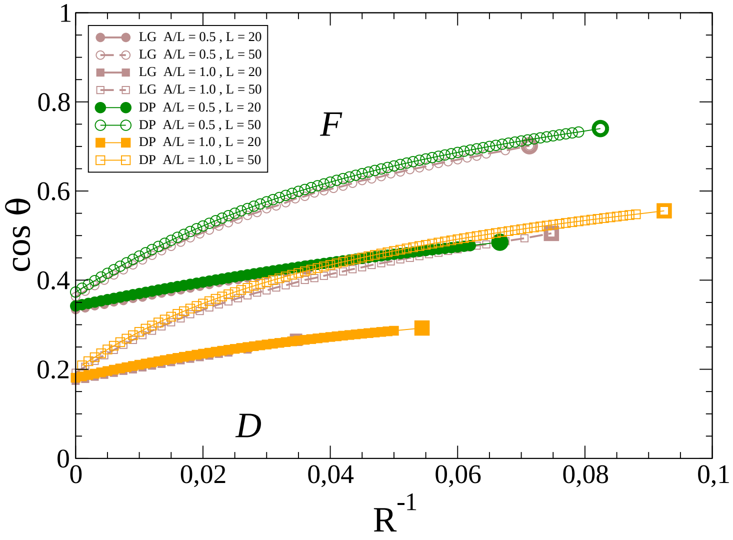

Figure 4.9: Off-coexistence $c = \infty$ interfacial phase diagram for $L = 20$ (dashed lines/filled symbols) and $L = 50$ (continuous lines/open symbols), corresponding to $A/L = 0.5$ (circles), $A/L = 1.0$ (squares), curves of the LG model (grey). The big symbols indicate the position of the critical points.

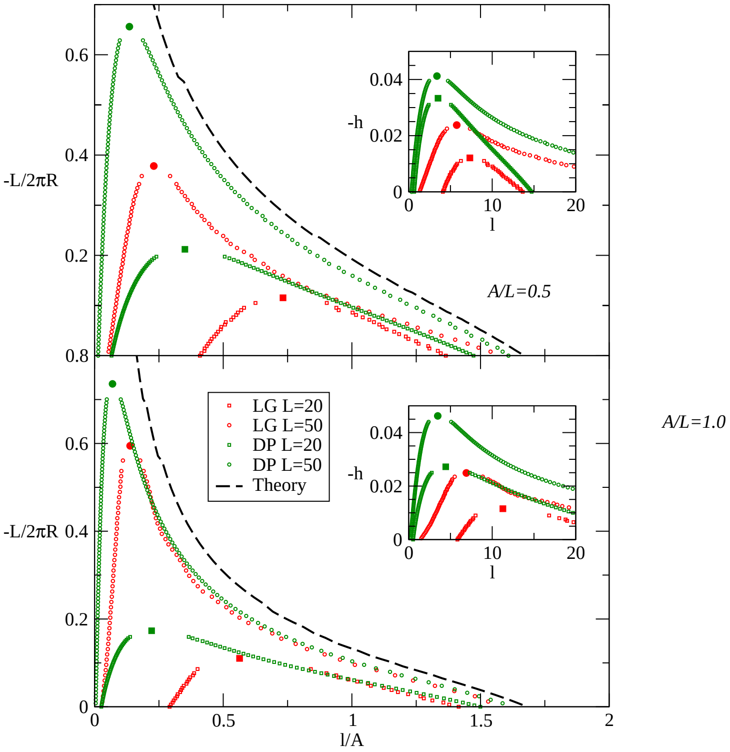

Figure 4.10: Plot of the midpoint interfacial height, in units of A, of the D and F states at the filling transition, as a function of $-L/(\pi R)$, corresponding to $c = \infty$, $A/L = 0.5, 1$, for $L = 20$ (squares) and $L = 50$ (circles), and DP model (green) and LG model (red). The dashed line corresponds to the macroscopic theory prediction for the midpoint interfacial height of the F state. The insets show a zoom of the D and F states midpoint interfacial heights, in units of the correlation length, as a function of $|h|$, close to the filling critical points (the meaning of the symbols is the same as in the main plots).

Chapter 5

Conclusions

In this Thesis we have studied the interfacial phenomenology of a fluid in contact with microstructured susbtrates. We have considered two different substrate geometries, the wedge and sinusoidal grating, and their study was carried out with three different models from analytical, numerical and computer simulation perspectives. Our results highlight the relevant role played by the substrate geometry on the adsorption phase diagram and the interfacial fluctuations. The milestones of our research are enumerated below.

First, we have studied the 3D wedge filling transition for the Ising model. We have performed Monte Carlo simulations in the double a double wedge geometry with applied antisymmetric surface fields on each wedge, with an additional field acting along the wedges. In addition, we have solved exactly a phenomenological theory which accounts for the breather mode fluctuations for the double wedge geometry which will be essential to understand the simulation results. Our main findings are the following:

1. For critical wedge filling, we found that there is a very good agreement between the computer simulation results and the theoretical predictions. This implies that the breather mode fluctuations indeed control the critical behaviour at the filling transition. On the other hand, this fact allows us to locate accurately the filling transition by matching the theoretical and simulation magnetization probability distribution functions for different simulation box sizes but keeping the ratio L_y/L^3 constant.

2. By tuning the field strength which acts along the wedges, we found strong evidences that the filling transition can be driven first-order. Furthermore, we found that, for certain values of this field, the critical wedge filling changes its character. This can be observed by monitoring

the magnetization probability distribution functions, which converge to the theoretical prediction for tricritical filling as the simulation box sizes increase. These observations confirm earlier predictions on the wedge filling phase diagram within the breather-mode picture reported in the literature.

The second problem we considered was the mean-field interfacial phase diagram of a fluid in contact a sinusoidal grating of intermediate to large roughness, paying special attention to filling and wetting transitions. This study was done by using coarse-grained microscopic models which allow us to go beyond the limitations of previous approaches such as the macroscopic theory or interfacial Hamiltonians. We first considered the phenomenology observed for the Landau-Ginzburg model. Our main findings are the following:

3. For substrates which undergo first-order wetting, the phase diagram at bulk coexistence shows the existence of two interfacial transitions: a filling transition, which is almost insensitive to the grating period L but depends on the substrate roughness as predicted by the macroscopic theory, and a wetting transition which shows a strong dependence on L even for a given ratio A/L. For large L, the shift of the wetting temperature with respect to the planar substrate value is controlled by the interface binding by the maxima of the grating. On the other hand, for very small L filling transition becomes metastable with respect to a Wenzel-like wetting transition between an empty and a completely wet interfacial states. The borderline between the small-L and large-L scenarios is a triple point where the empty, filled and completely wet interfacial states coexist.

4. The off-coexistence phase diagram corresponding to substrates which undergo first-order wetting show two transition lines which start at the bulk coexistence filling and wetting transitions, and which end up at critical points. The off-coexistence filling transition shows a crossover from the behaviour predicted by macroscopic theory close to bulk coexistence to a prewetting-like behaviour when approaching the filling critical point. This result implies that the filling transition far from bulk coexistence is controlled by the interface binding by the grating grooves. On the other hand, the prewetting lines show a similar dependence on L, so as in the wetting case, this transition is controlled by the interface binding by the maxima of the grating.

5. For substrates which undergo critical wetting, the wetting transition remains unaltered by the substrate roughness, as predicted by interfacial

Hamitonian theories. On the other hand, the filling transition shows, for a given interfacial roughness, a stronger dependence on L, converging to the macroscopic transition value for large L but disappearing for small L at a critical point. This scenario is qualitatively similar to the predicted by interfacial Hamiltonians. However, our results do not obey the scaling predicted by interfacial Hamiltonians, at least for the range of values of the roughness we considered. Finally, for off-coexistence conditions the phase diagram shows a filling transition line that ends up a critical point. The dependence on L is again stronger than when the substrate presents first-order wetting, and similar to the observed under bulk coexistence conditions.

Finally, we revisited the mean-field study of the adsorption phase diagram on sinusoidal gratings within the double parabola model. This model is interesting because can be regarded as an approximation to the Landau-Ginzburg model, but on the other hand it can be formally reduced to an interfacial Hamiltonian theory which reduces to the perturbative non-local models in some limit. In this sense, our study may help to bridge the gap between the microscopic and mesoscopic descriptions of fluid adsorption on microstructured substrates. We restricted our study to a substrate which undergoes critical wetting. Our main findings are the following:

6. We have developed a method to minimize the free-energy functional for the double parabola model, related to the Boundary Element Method used for engineering applications. However, there are still some numerical issues in its implementation which need further work. Despite these problems, we obtained the interfacial phase diagram, and from a qualitatively point of view is quite similar to that obtained from the Landau-Ginzburg model, both for bulk coexistence and in the single-phase region. However, there are quantitative discrepancies in terms of the natural variables of the model (surface magnetization m_s and ordering field h).

7. When the results of the double parabola and the Landau-Ginzburg models are compared in terms of the fields $\cos\theta$ and the interfacial curvature R^{-1}, which are different functions of m_s and h for each model, respectively, we observe a much better agreement between them. Thus, we conclude that the double parabola model is a good approximation to the Landau-Ginzburg model for renormalized values of m_s and h. In the future the comparison with perturbative non-local models may help to assess their validity.

Appendix A

The Landau-Ginzburg theory of wetting of flat substrates

In this Appendix we review the Landau-Ginzburg theory, focusing on its application to interfacial transitions such as wetting transition. Because of its simplicity, this model has been extensively studied in this context in the literature [15, 21, 40, 41, 58, 59, 82–85, 137]. For convenience we use the magnetic language, where the order parameter has the same symmetry as the magnetization per unit volume in the Ising model. However, the results obtained for this system are completely valid for the interfacial phenomenology of simple fluids, identifying the order parameter with the deviation of the density with respect to its critical value. We will also restrict ourselves to the three-dimensional situation, although the formalism can be applied to other dimensionalities.

The free energy functional of the system in contact with a substrate can be expressed in terms of the order parameter field $m(\mathbf{r})$ as:

$$\begin{aligned} \mathcal{F} &= \mathcal{F}_0 + \int_V d\mathbf{r} \left[\frac{g}{2}(\boldsymbol{\nabla} m)^2 + a_2 t m^2 + a_4 m^4 - hm \right] \\ &+ \int_{\mathcal{S}} d\mathbf{s} \frac{c}{2}(m(\mathbf{s}) - m_s(\mathbf{s}))^2 \end{aligned} \tag{A.1}$$

where the first term corresponds to Landau-Ginzburg functional on total volume V while the second term takes into account the interaction with the substrate. Thus, $\mathcal{F}_0$ is a reference free energy, g, a_2 and a_4 are positive constants, h is the ordering field (magnetic field magnetic systems, deviation of chemical potential with respect to the value at coexistence in fluid systems) and $t = (T - T_c)/T_c$ characterizes the temperature deviation with respect to the critical value T_c. Regarding the interaction with the substrate, the integration is restricted to the surface of the substrate S. Finally c is the *enhancement* parameter and $m_s(\mathbf{s})$ is the favoured order parameter value by the substrate, and that will be assumed to be positive, so it favors the phase with volume order parameter $+m_0$ when $t < 0$ and $h = 0$. For later purposes, it will be useful to define the applied surface field $h_1(\mathbf{s}) = cm_s(\mathbf{s})$. For theoretical analysis and its computational implementation it is convenient to use a description in terms of reduced units. To do this, we must first determine the natural scales of each variables. The natural scale for the order parameter field is given by the equilibrium value of this magnitude m_{eq} for $h = 0$ in the Landau theory. Although for $t > 0$ $m_{eq} = 0$, for temperatures below the critical and $h = 0$ the states characterized by $m_{eq} = \sqrt{a_2(-t)/(2a_4)}$ and $-\sqrt{a_2(-t)/(2a_4)}$ are at coexistence. Thus, as we are interested in situations where there is coexistence of phases (which implies that $t < 0$), we define m_0 as:

$$m_0 = \sqrt{\frac{a_2|t|}{2a_4}} \tag{A.2}$$

On the other hand, the natural length scale is given by the correlation length ξ defined from the Ornstein-Zernike theory correlation applied to the Landau-Ginzburg functional:

$$\xi = \sqrt{\frac{g}{2a_2t + 12a_4m_{eq}^2}} = \begin{cases} \sqrt{\frac{g}{2a_2t}} & t > 0 \\ \sqrt{\frac{g}{4a_2(-t)}} & t < 0 \end{cases} \tag{A.3}$$

By analogy with the definition of the scale of the order parameter, define the length scale ξ_0 as

$$\xi_0 = \sqrt{\frac{g}{4a_2|t|}} \tag{A.4}$$

Therefore, if we define $\tilde{m} = m/m_0$ and $\tilde{\mathbf{r}} = \mathbf{r}/\xi_0$ Then we can define a reduced free energy as:

$$\begin{aligned} \tilde{\mathcal{F}} &= \frac{\mathcal{F}}{8a_4m_0^4\xi_0^3} = \tilde{\mathcal{F}}_0 \\ &+ \int_{\tilde{V}} d\tilde{\mathbf{r}} \left[\frac{1}{2}(\tilde{\boldsymbol{\nabla}}\tilde{m})^2 - \tilde{h}\tilde{m} \pm \frac{1}{4}\tilde{m}^2 + \frac{1}{8}\tilde{m}^4\right] \\ &+ \int_{\tilde{S}} d\tilde{\mathbf{s}} \frac{\tilde{c}}{2}(\tilde{m} - \tilde{m}_s)^2 \end{aligned} \tag{A.5}$$

where $\tilde{\mathcal{F}}_0 = \mathcal{F}_0/(8am_0^4\xi_0^3)$, $\tilde{\boldsymbol{\nabla}} = \xi_0\boldsymbol{\nabla}$, and positive or negative corresponds to $t > 0$ or $t < 0$, respectively. The reduced ordering field $\tilde{h}$ is defined as:

$$\tilde{h} = \frac{h}{8a_4m_0^3} \tag{A.6}$$

Finally, the reduced parameters of the interaction with the surface are defined as $\tilde{m}_s = m_s/m_0$ and $\tilde{c} = c/(8a_4 m_0^2 \xi_0)$. Consequently, the reduced surface field $\tilde{h}_1(\tilde{\mathbf{s}}) = h_1(\mathbf{s})/(8a_4 m_0^3 \xi_0)$. Since there is some freedom to choose the source of energy, choose $\tilde{F}_0 = \tilde{V}/8$. Thus, we can rewrite (A.5) as:

$$\begin{aligned}\tilde{F} &= \int_{\tilde{V}} d\tilde{\mathbf{r}} \left[\frac{1}{2}(\tilde{\boldsymbol{\nabla}}\tilde{m})^2 - \tilde{h}\tilde{m} + \frac{1}{8}(\tilde{m}^2 \pm 1)^2\right] \\ &+ \int_{\tilde{S}} d\tilde{\mathbf{s}} \frac{\tilde{c}}{2}(\tilde{m} - \tilde{m}_s)^2 \end{aligned} \qquad \text{(A.7)}$$

Hereafter we will only consider reduced units, so we will drop the tildes in the expressions above. In the mean field approximation, the equilibrium profile parameter order is obtained by minimization of the functional (A.7) [15]. Using the functional derivative of F with respect to $m(\mathbf{r}_0)$ (assuming $\mathbf{r}_0$ is not on the substrate) and making it equal to zero, we obtain the following Euler-Lagrange equation:

$$\nabla^2 m = -h + \frac{m(m^2 \pm 1)}{2} \qquad \text{(A.8)}$$

On the other hand, the variation of the order parameter field in a surface point $\mathbf{s}_0$ leads to the following boundary condition:

$$\mathbf{n}\cdot\boldsymbol{\nabla} m(\mathbf{s}_0) = c(m(\mathbf{s}_0) - m_s(\mathbf{s}_0)) = cm(\mathbf{s}_0) - h_1(\mathbf{s}_0) \qquad \text{(A.9)}$$

where $\mathbf{n}$ is the inward normal to the substrate in $\mathbf{s}_0$ (i.e. directed towards the system). Finally, we impose that the order parameter far from the surface takes the equilibrium value given by the Landau theory m_b:

$$m(\mathbf{r}) \to m_b \qquad \text{far from the substrate} \qquad \text{(A.10)}$$

If we restrict ourselves to the situation of coexistence ($h = 0$ and $t < 0$), the order parameter far from the substrate has the boundary condition $m \to -1$.

In general, the differential equation (A.8) with boundary conditions (A.9) and (A.10) cannot be solved analytically and we must resort to numerical methods. However, in the case of a flat substrate with c and h_1 constants the problem can be solved analytically. Consider that the substrate is on the plane xy. Then, by symmetry, the order parameter field depends only of the coordinate z. At bulk coexistence ($h = 0$ and $t < 0$), (A.8) reduces to:

$$\frac{d^2 m}{dz^2} = \frac{m(m^2 - 1)}{2} \qquad \text{(A.11)}$$

Multiplying this equation by (dm/dz) and integrating in the range $z \in [z_0, +\infty]$, we obtain the following expression:

$$\frac{1}{2}\left(\frac{dm}{dz}\right)^2\bigg|_{z=z_0} = \frac{1}{8}(m(z_0)^2 - 1)^2 \tag{A.12}$$

where we have used the boundary condition (A.10) $(m(z \to \infty) \to -1)$ and that $dm/dz \to 0$ when $z \to \infty$. The order parameter profile thus will be a monotonous increasing function if $m(0) < -1$, and a decreasing function otherwise. We can obtain from (A.12) the derivative of order parameter to an arbitrary height z as:

$$\frac{dm}{dz} = -\frac{1}{2}(m+1)|m-1| \tag{A.13}$$

This condition is valid for all $z \geq 0$. In fact, we can integrate (A.13) for $m(z)$. So, for $m(0) < 1$ the equilibrium profile satisfies order parameter

$$m(z) = -\tanh\left(\frac{z - z_0}{2}\right) \tag{A.14}$$

where $z_0 = 2 \text{ atanh } m(0) = \ln[(1 + m(0))/(1 - m(0))]$. If $z_0 > 0$, these profiles describe interfacial states where you can identify a layer of bulk order parameter $+1$ for $z < z_0$ in contact with the bulk phase characterized by the order parameter -1 for $z > z_0$. Therefore, the interfacial position is given by z_0 as $m(z_0) = 0$.

If $m(0) > 1$, the solution has the expression:

$$m(z) = \begin{cases} \coth\left(\frac{z-z_0}{2}\right) & \text{if } m(z) > 1 \\ -\tanh\left(\frac{z-l}{2}\right) & \text{if } m(z) < 1 \end{cases} \tag{A.15}$$

where $z_0 = -2 \text{ acoth } m(0) = -\ln[(m(0) + 1)/(m(0) - 1)]$. However, it is easy to see from the first equation that $m(z) > 1$ for all z. This implies that the only allowable value of l is infinite. As at $z = l$, $m(l) = 0$, this condition implies that a layer of infinite thickness of order parameter $+1$ has nucleated between the substrate and the bulk phase. Therefore, profiles with $m(0) < 1$ will correspond to *partial wetting*, while if $m(0) > 1$ we have *complete* wetting. Figure A.1 shows some typical order parameter profiles. The equilibrium free energy F_{eq} can be obtained by replacing the order parameter profiles in the functional (A.7). However, their evaluation can be simplified taking into account (A.12). If we define the surface tension between the substrate and the bulk phase with order parameter -1, σ_{W-}, as F_{eq}/A (note

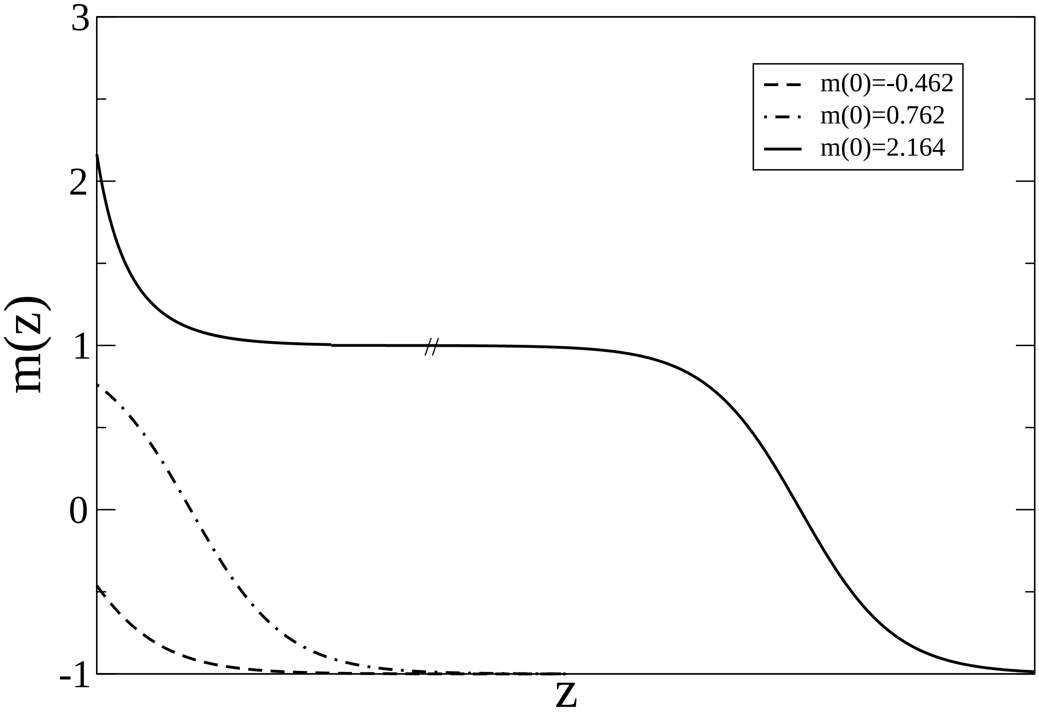

Figure A.1: Typical profiles of order parameter theory Landau-Ginzburg for the phenomenon of wetting on a flat substrate. The profiles corresponding to $m(0) = -0.462$ (dashed curve), $m(0) = 0.762$ (curve of dots and dashes) and $m(0) = 2.164$. The latter case corresponds to complete wetting, so the width of the layer of $+1$ phase becomes infinite.

that the bulk contribution is zero in our case), then we can evaluate it as:

$$\sigma_{W-} = \int_0^\infty \left(\frac{dm}{dz}\right)^2 dz + \frac{c}{2}(m(0) - m_s)^2 \tag{A.16}$$

Given that the order parameter profiles are monotonous, and using (A.13), we can express the surface tension as:

$$\begin{aligned} \sigma_{W-} &= -\int_{-1}^{m(0)} \left(\frac{dm}{dz}\right) dm + \frac{c}{2}(m(0) - m_s)^2 \\ &= \int_{-1}^{m(0)} \frac{1}{2}(m+1)|m-1| dm + \frac{c}{2}(m(0) - m_s)^2 \end{aligned} \tag{A.17}$$

Therefore, the surface tension σ_{W-} has the expression:

$$\sigma_{W-} = \begin{cases} \frac{m(0)}{2} - \frac{m(0)^3}{6} + \frac{1}{3} + \frac{c}{2}(m(0) - m_s)^2 & m(0) < 1 \\ \sigma_{W+} + \sigma_{+-} & m(0) > 1 \end{cases} \tag{A.18}$$

where σ_{+-} is the surface tension associated to the interface between the two bulk phases at coexistence:

$$\sigma_{+-} = \int_{-1}^{1} \frac{1}{2}(1 - m^2)dm = \frac{2}{3} \tag{A.19}$$

and σ_{W+} is the surface tension between the substrate and a bulk phase with order parameter $+1$. Under these conditions, (A.13) changes to $dm/dz = -|m+1|(m-1)/2$, and then

$$\begin{aligned}\sigma_{W+} &= -\int_{1}^{m(0)} \left(\frac{dm}{dz}\right) dm + \frac{c}{2}(m(0) - m_s)^2 \\ &= \int_{1}^{m(0)} \frac{1}{2}|m+1|(m-1)dm + \frac{c}{2}(m(0) - m_s)^2 \\ &= -\frac{m(0)}{2} + \frac{m(0)^3}{6} + \frac{1}{3} + \frac{c}{2}(m(0) - m_s)^2 \end{aligned} \tag{A.20}$$

Note that the expression for σ_{W-} and $m(0) > 1$ given by (A.18) is predicted by Young's law under conditions of complete wetting.

The values of $m(0)$ can be obtained by using the boundary condition (A.9). Therefore, the derivatives of the order parameter profile at must satisfy simultaneously that:

$$\left.\frac{dm}{dz}\right|_{z=0} = -\frac{1}{2}(m(0) + 1)|m(0) - 1| = cm(0) - h_1 \tag{A.21}$$

Therefore, we get $m(0)$ by using a graphical construction (see figure A.2). Three different situations can be observed depending on the value of c:

1. **Critical wetting transition ($c > 1$).** Under these conditions, there is only one intersection of (A.21) at a value of $m(0)$ given by the expression:

   $$m(0) = \begin{cases} c - \sqrt{c^2 + (1 - 2cm_s)} & m_s < 1 \\ -c + \sqrt{c^2 + (1 + 2cm_s)} & m_s > 1 \end{cases} \tag{A.22}$$

   Therefore, the system goes continuously from a partial wetting situation for $m_s < 1$ to a situation complete wet for $m_s > 1$, so the wetting transition is continuous and occurs at $m_s = 1$.

2. **Tricritical wetting transition ($c = 1$).** This situation corresponds to the borderline between continuous and first-order wetting transitions. However, the description of the transition is similar to the case of critical wetting.

3. **First-order wetting transition ($c < 1$).** Under these conditions, there may be up to three intersections of (A.21), which will be denoted by m^-, m^0 and m^+:

$$m^- = c - \sqrt{c^2 + (1 - 2h_1)} \tag{A.23}$$

$$m^0 = c + \sqrt{c^2 + (1 - 2h_1)} \tag{A.24}$$

$$m^+ = -c + \sqrt{c^2 + (1 + 2h_1)} \tag{A.25}$$

Therefore, there may be up to three possible order parameter profiles. To identify the true equilibrium profile, we evaluate the surface free energy. It can be shown that the profile for the solution term m^0 always has a free energy higher than other states. As for h_1 small or negative the only possible solution corresponds to that with $m(0) = m^-$, and for large h_1 the only solution corresponds to the complete wetting profile where $m(0) = m^+$, there must be an intermediate value of h_1, where both states coexist. Thus, the wetting transition is given by the value of h_1 for which $\sigma_{W-}(m^-) = \sigma_{W+}(m^+)$. This condition has a graphical interpretation: the wetting transition occurs for the value of h_1 for which the areas enclosed by curves given by (A.21) between m^- and m^0, on one hand, and m^0 and m^+, on the other hand, are equal (Maxwell construction). Starting from the wetting transition, and out of coexistence (i.e. $h < 0$), the prewetting transition emerges [84], where two distinct interfacial structures characterized by different but finite adsorbed phase film thicknesses (see figure A.3). This transition line starts tangentially to the bulk coexistence curve $h = 0$, as predicted by the Clausius-Clapeyron relationship [49], and finishes at the prewetting critical point. The location of this transition is obtained by a similar construction to the outlined above for the wetting transition: the two interfacial phases are determined by the surface magnetization, obtained by the intersection of the following curves:

$$\begin{aligned} \left.\frac{dm}{dz}\right|_{z=0} &= -\sqrt{-2h(m+1) + \frac{1}{4}(m^2(0) - 1)^2} \\ \left.\frac{dm}{dz}\right|_{z=0} &= cm(0) - h_1 \end{aligned} \tag{A.26}$$

Up to three solutions may be obtained. The true equilibrium profile corresponds to the solution with minimum surface free energy. Coexistence is obtained when the areas enclosed by the curves given by

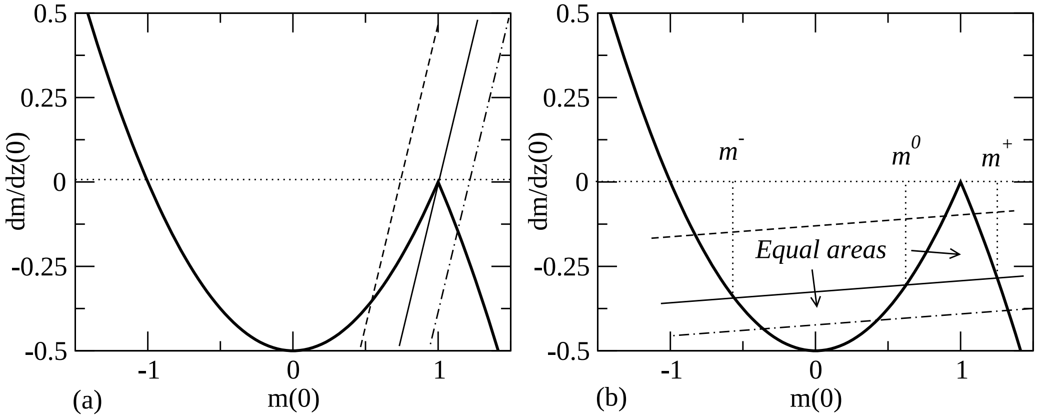

Figure A.2: Graphical construction to obtain $m(0)$ for: (a) $c > 1$, (b) $c < 1$. The dashed lines correspond to partial wetting situations, the dot-dashed lines to complete wetting situations, and the continuous lines to the wetting transition.

(A.26) are equal, and the prewetting critical point corresponds to the situation where the three solutions merge into the same value.

Finally, we can obtain analytically the contact angle θ via Young's law:

$$\cos\theta = \frac{\sigma_{W-}(m(0)) - \sigma_{W+}(m^*(0))}{\sigma_{+-}} \tag{A.27}$$

where σ_{W-}, σ_{W+} and σ_{+-} are given by the expressions (A.18) (A.20) and (A.19), respectively, $m(0)$ is the value of the equilibrium order parameter at $z = 0$ (obtained through the construction explained above), and $m^*(0)$ is the value of the equilibrium order parameter at $z = 0$ which decays to $m = 1$ when $z \to +\infty$. This value can be obtained via a graphical construction similar to that already explained, where we look for solutions of the equation:

$$-\frac{1}{2}|m^*(0) + 1|(m^*(0) - 1) = cm^*(0) - h_1 \tag{A.28}$$

For $h_1 > 0$, this solution is given by:

$$m^*(0) = -c + \sqrt{c^2 + (1 + 2h_1)} \tag{A.29}$$

In order to finish this introduction to the Landau-Ginzburg model of wetting of flat substrates, it is common in the literature to study the wetting phenomena by using interfacial Hamiltonians, where the surface free energy associated to an interfacial configuration (i.e. by fixing the surface at which the magnetization is zero, for example), is given by:

$$\mathcal{F} = \int_{\mathcal{A}} d\mathbf{s} \left[\frac{\sigma_{+-}}{2} (\boldsymbol{\nabla} \ell(\mathbf{s}))^2 + W(\ell(\mathbf{s})) \right] \tag{A.30}$$

where $\ell(\mathbf{s})$ is the interfacial height above the position $\mathbf{s}$ of the substrate and $W(\ell)$ is the interfacial binding potential. A considerable work has been reported in the literature to justify (A.30) from first principles [15,40,41,58,59]. More recently, a new derivation of (A.30) has been proposed, where in general the binding potential is not a local function but a non-local functional of $\{\ell(\mathbf{s})\}$ [7,91–94,98,99]. For parallel and flat substrate and interface, this functional reduces again to a function, which has a long-distance expansion [7,15,40,58,91]:

$$\begin{aligned} W(\ell) &\approx -2h\ell - \frac{4c}{1+c}(1-m_s)\exp(-\ell) \\ &+ \frac{4(c-1)}{1+c}\exp(-2\ell) + \ldots \end{aligned} \tag{A.31}$$

For critical wetting, this expansion is enough to characterize the divergence of the interfacial height. The equilibrium height is given by the absolute minimum of (A.31). So, at $h = 0$, $\ell_{eq} = \ln(2(c-1)/(c(1-m_s))) \approx \ln(2/(1-m(0))) \approx \ln((1+m(0))/(1-m(0)))$ when $m_s \to 1$, in agreement with the full Landau-Ginzburg model results.

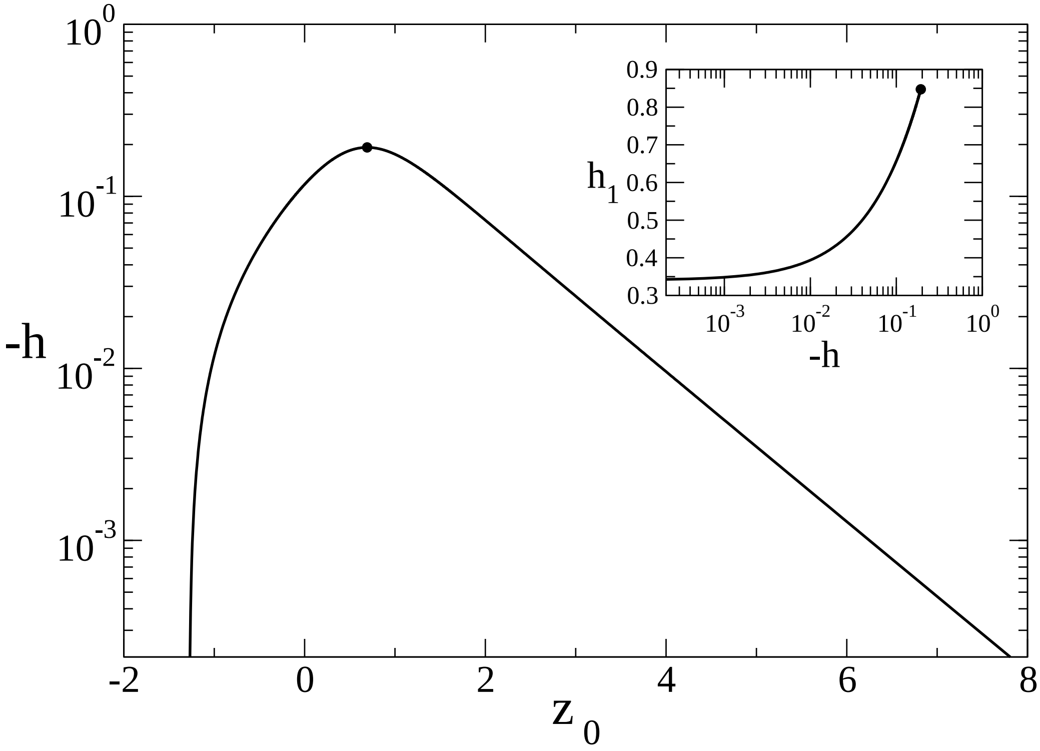

Figure A.3: Plot of the interfacial height z_0 of the coexisting interfacial states along the prewetting line for $c = 0$ as a function of $|h|$. The dot corresponds to the location of the prewetting critical point, and negative values of z_0 means that the magnetization at the wall is negative. Inset: Plot of the prewetting line for $c = 0$ on the $|h| - h_1$ plane.

Appendix B

The Conjugate Gradient Method.

In this Thesis we have to minimize different free-energy functionals which reduce to sets of non-linear equations in their arguments. The minimization technique used in all the cases is the conjugate gradient method, or variations of it. Consider a function $f(\mathbf{x})$ that can be approximated roughly to a quadratic form close to the minimum

$$f(\mathbf{x}) = c - \mathbf{b} \cdot \mathbf{x} + \frac{1}{2} \mathbf{x} \cdot \mathbf{A} \cdot \mathbf{x} \tag{B.1}$$

where $\mathbf{A}$ is the Hessian matrix at the minimum. The Conjugate Gradient Method is a technique for solving linear algebraic equations by minimizing a quadratic form like (B.1) [109]. The minimization is carried out by generating a succession of conjugates search directions $\mathbf{h}_i$, i.e. orthogonal with respect to the inner product $\langle \mathbf{u}, \mathbf{v} \rangle \equiv \mathbf{u} \cdot \mathbf{A} \cdot \mathbf{v}$, and improved minimizers $\mathbf{x}_i$. These sequences of vectors are built up in such a way that $\mathbf{x}_{i+1} = \mathbf{x}_i + \lambda_i \mathbf{h}_i$ is not only the minimizer of f along the line defined by $\mathbf{x}_i$ and $\mathbf{h}_i$, but also over the vector subspace of directions already taken $\{\mathbf{h}_1, \ldots, \mathbf{h}_k\}$. This can be done by imposing the condition that the residual $\mathbf{g}_{i+1} = \mathbf{b} - \mathbf{A} \cdot \mathbf{x}_{i+1}$ at $\mathbf{x}_{i+1}$ is orthogonal to $\mathbf{h}_k$ for $k = 1, \ldots, i$. After N iterations you arrive to the minimizer of the quadratic form over the entire vector space, since the set $\{\mathbf{h}_i, i = 1, \ldots, N\}$ is a base. For an arbitrary initial vector $\mathbf{g}_1$ and $\mathbf{h}_1 = \mathbf{g}_1$, this method constructs the two sequences of vectors from recurrence

$$\mathbf{g}_{i+1} = \mathbf{g}_i - \lambda_i \mathbf{A} \cdot \mathbf{h}_i \qquad \mathbf{h}_{i+1} = \mathbf{g}_{i+1} + \gamma_i \mathbf{h}_i \qquad i = 1, 2, \ldots \tag{B.2}$$

Imposing that these vectors satisfy the orthogonality and conjugacy conditions

$$\mathbf{g}_i \cdot \mathbf{g}_j = 0 \qquad \mathbf{h}_i \cdot \mathbf{A} \cdot \mathbf{h}_j = 0 \qquad \mathbf{g}_i \cdot \mathbf{h}_j = 0 \qquad i \neq j \tag{B.3}$$

we get that the scalars λ_i and γ_i are given by

$$\lambda_i = \frac{\mathbf{g}_i \cdot \mathbf{g}_i}{\mathbf{h}_i \cdot \mathbf{A} \cdot \mathbf{h}_i} = \frac{\mathbf{g}_i \cdot \mathbf{h}_i}{\mathbf{h}_i \cdot \mathbf{A} \cdot \mathbf{h}_i} \tag{B.4}$$

$$\gamma_i = \frac{\mathbf{g}_{i+1} \cdot \mathbf{g}_{i+1}}{\mathbf{g}_i \cdot \mathbf{g}_i} \tag{B.5}$$

However, in order to proceed, we need to know the matrix $\mathbf{A}$. This can be avoid with the following procedure. We set $\mathbf{g}_i = -\nabla f(\mathbf{x}_i)$ for some point $\mathbf{x}_i$. Now, we proceed from $\mathbf{x}_i$ along the direction $\mathbf{h}_i$ to the local minimum of f located at some point $\mathbf{x}_{i+1}$ and set $\mathbf{g}_{i+1} = -\nabla f(\mathbf{x}_{i+1})$. As from Eq. (B.1), $\mathbf{g}_i = \mathbf{b} - \mathbf{A} \cdot \mathbf{x}_i$, then $\mathbf{g}_{i+1} = \mathbf{b} - \mathbf{A} \cdot (\mathbf{x}_i + \lambda \mathbf{h}_i) = \mathbf{g}_i - \lambda \mathbf{A} \cdot \mathbf{h}_i$, with λ chosen to take us to the line minimum. But at the line minimum $\mathbf{h}_i \nabla f = -\mathbf{h}_i \cdot \mathbf{g}_{i+1} = 0$, leading to the value of λ_i from Eq. (B.4). Thus, we can *define* $\mathbf{g}_i$ as $-\nabla f(\mathbf{x}_i)$ at each step, instead of using the expression in (B.2).

As our function is f not really quadratic, Polak and Ribiere introduced the following modification:

$$\gamma_i = \frac{(\mathbf{g}_{i+1} - \mathbf{g}_i) \cdot \mathbf{g}_{i+1}}{\mathbf{g}_i \cdot \mathbf{g}_i} \tag{B.6}$$

where again $\mathbf{g}_i = -\nabla f(\mathbf{x}_i)$, being $\mathbf{x}_i$ the line minimizer at each step.

Bibliography

[1] D.B. Abraham and A. Maciolek. *Phys. Rev. Lett.*, **89**, 286101 (2002).

[2] D.B. Abraham, V. Mustonen and A.J. Wood. *Europhys. Lett.*, **63**, 408 (2003).

[3] D.B. Abraham, A.O. Parry and A.J. Wood. *Europhys. Lett.*, **60**, 106 (2002).

[4] M. Abramowitz and I.A. Stegun *Handbook of mathematical functions with formulas, graphs and mathematical tables* (Dover Publications, Inc., New York, 1972).

[5] E.V. Albano, A.D. Virgiliis, M. Müller and K. Binder. *J. Phys.: Condens. Matter*, **15**, 333 (2003).

[6] A. Bednorz, and M. Napiorkowski. *J. Phys. A: Math. Gen.*, **33**, L353 (2000).

[7] N.R. Bernardino, A.O. Parry, C. Rascón and J.M. Romero-Enrique. *J. Phys.: Condens. Matter*, **21**, 465105 (2009).

[8] N.R. Bernardino, A.O. Parry, and J.M. Romero-Enrique. *J. Phys.: Condens. Matter*, **24**, 182202 (2012).

[9] K. Binder, R. Evans, D.P. Landau, and A.M. Ferrenberg. *Phys. Rev. E*, **53**, 5023 (1996).

[10] K. Binder, D.P. Landau, and D.M. Kroll. *Phys. Rev. Lett.*, **56**, 2272 (1986).

[11] K. Binder, D.P. Landau, and S. Wansleben. *Phys. Rev. B*, **40**, 6971 (1989).

[12] K. Binder, M. Müller, A. Milchev and D.P. Landau. *Comput. Phys. Commun.*, **169**, 226 (2005).

[13] F. Bresme *et al. Chem. Phys. Phys. Chem.*, **10**, 4704 (2008).

[14] F. Bresme, E. Chacon and P. Tarazona. *Phys. Rev. Lett.*, **101**, 056102 (2008).

[15] E. Brézin, B.I. Halperin and S. Leibler. *J. Phys. (France)*, **44**, 775 (1983).

[16] L. Bruschi, A. Carlin and G. Mistura. *J. Chem. Phys.*, **115**, 6200 (2001).

[17] L. Bruschi, A. Carlin and G. Mistura. *Phys. Rev. Lett.*, **89**, 166101 (2002).

[18] L. Bruschi, A. Carlin and G. Mistura. *J. Phys.: Condens. Matter*, **15**, S315 (2003).

[19] L. Bruschi, A. Carlin, A.O. Parry and G. Mistura. *Phys. Rev. E*, **68**, 021606 (2003).

[20] T.W. Burkhardt. *Phys. Rev. B*, **40**, 6987 (1989).

[21] J.W. Cahn. *J. Chem. Phys.*, **66**, 3667 (1977).

[22] A.B.D. Cassie and S. Baxter. *Trans. Faraday Soc.*, **40**, 546 (1944).

[23] E. Chacon and P. Tarazona. *Phys. Rev. Lett.*, **91**, 166103 (2003).

[24] E. Chacon and P. Tarazona. *Phys. Rev. B*, **70**, 235407 (2004).

[25] E. Chacon and P. Tarazona. *J. Phys.: Condens. Matter*, **17**, S3493 (2005).

[26] N.T. Chamakos, M.E. Kavousanakis and A.G. Papathanasiou. *Soft Matter*, **9**, 9624 (2013).

[27] A. Checco A, B.M. Ocko, M. Tasinkevych and S. Dietrich. *Phys. Rev. Lett.*, **109**, 166101 (2012).

[28] J.C. Cheng, and A.P. Pisano. *J. Microelectromech. Syst.*, **17**, 402 (2008).

[29] L. Chetouani, L. Dekar, and T.F. Hammann. *Phys. Rev. A*, **52**, 82 (1995).

[30] P. Concus and R. Finn. *Proc. Natl. Acad. Sci. USA*, **63**, 292 (1969).

[31] G.A. Darbellay and J.M. Yeomans. *J. Phys. A: Math. Gen.*, **25**, 4275 (1992).

[32] R. Delgado-Buscalioni, E. Chacon and P. Tarazona. *Phys. Rev. Lett.*, **101**, 106102 (2008).

[33] S. Dietrich. *Phase Transitions and Critical Phenomena*, vol 12, ed C Domb y J L Lebowitz (Academic Press, New York, 1988).

[34] A.L. Dubov, A. Mourran, M. Möller and O.I. Vinogradova. *Appl. Phys. Lett.*, **106**, 241601 (2015).

[35] C. Ebner and W.F. Saam. *Phys. Rev. Lett.*, **38**, 1486 (1977).

[36] A.M. Ferrenberg, D.P. Landau, and K. Binder. *Phys. Rev. E*, **58**, 3353 (1998).

[37] A.M. Ferrenberg and R.H. Swendsen. *Phys. Rev. Lett.*, **61**, 2635 (1988).

[38] A.M. Ferrenberg and R.H. Swendsen. *Phys. Rev. Lett.*, **63**, 1195 (1989).

[39] R.P. Feynman and A.R. Hibbs. *Quantum Mechanics and Path Integrals* (McGraw-Hill, New York, 1965).

[40] M.E. Fisher. *J. Chem. Soc. Faraday Trans.*, **82**, 1589 (1986).

[41] M.E. Fisher and A.J. Jin. *Phys. Rev. B*, **44**, 1430 (1991).

[42] M.E. Fisher and A.J. Jin. *Phys. Rev. Lett.*, **69**, 792 (1992).

[43] G. Forgacs, R. Lipowsky and Th.M. Nieuwenhuizen. *Phase Transitions and Critical Phenomena*, vol 14, ed C Domb y J L Lebowitz (Academic Press, New York, 1991).

[44] R. Frenkel, B. Kin and D. Yao. *Machines.*, **2**, 299 (2014).

[45] O. Gang, K.J. Alvine, M. Fukuto, P.S. Pershan, C.T. Black and B.M. Ocko. *Phys. Rev. Lett.*, **95**, 217801 (2005).

[46] H. Gau, S. Herminghaus, P. Lenz and R. Lipowsky. *Science*, **283**, 46 (1999).

[47] M.J. Greenall, A.O. Parry, and J.M. Romero-Enrique. *J. Phys.: Condens. Matter*, **16**, 2515 (2004).

[48] E.H. Hauge, *Phys. Rev. A*, **46**, 4994 (1992).

[49] E.H. Hauge and M. Schick. *Phys. Rev. B*, **27**, 4288 (1983).

[50] J.R. Henderson, *J. Chem. Phys.*, **120**, 1535 (2004).

[51] J.R. Henderson, *Phys. Rev. E*, **69**, 061613 (2004).

[52] J.R. Henderson, *Mol. Simul.*, **31**, 435 (2005).

[53] S. Herminghaus, H. Gau and W. Mönch. *Advanced materials*, **11**, 1393 (1999).

[54] T. Hofmann, M. Tasinkevych, A. Checco, E. Dobisz, S. Dietrich and B.M. Ocko. *Phys. Rev. Lett.*, **104**, 106102 (2010).

[55] F.J. Hol and C. Dekker. *Science*, **346**, 1251821 (2014).

[56] D.A. Huse, C.L. Henley and D.S. Fisher. *Phys. Rev. Lett.*, **55**, 2924 (1985).

[57] A. Javadi, M. Habibi, F.S. Taheri, S. Moulinet and D. Bonn. *Sci. Rep.*, **3**, 1412 (2013).

[58] A.J. Jin and M.E. Fisher. *Phys. Rev. B*, **47**, 7365 (1993).

[59] A.J. Jin and M.E. Fisher. *Phys. Rev. B*, **48**, 2642 (1993).

[60] Y. Katasho *et al. Sci. Rep.*, **5**, 13790 (2015).

[61] J.T. Katsikadelis. *Boundary elements: theory and applications* (Elsevier, Oxford, 2002).

[62] G.P. Kubalski, M. Napiórkowski and K. Rejmer. *J. Phys.: Condens. Matter*, **13**, 4727 (2001).

[63] A. Lafuma and D. Quéré. *Nature Mater.*, **2**, 457 (2003).

[64] P.S. Laplace. *Tramité de Mécanique Céleste; Supplement au Dixiéme Livre, Sur l'Action Capillaire* (Courcier, Paris, 1806).

[65] M.S. Lavine. *Science*, **310**, 199 (2005).

[66] B.M. Law. *Prog. Surf. Sci.*, **66**, 159 (2001).

[67] C-C. Lee *et al. Science*, **310**, 1793 (2005).

[68] R. Lipowski and M.E. Fisher. *Phys. Rev. B*, **36**, 2126 (1987).

[69] A. Malijevsky. *J. Chem. Phys.*, **137**, 214704 (2012).

[70] A. Malijevsky. *J. Phys.: Condens. Matter*, **25**, 445006 (2013).

[71] A. Malijevsky. *J. Chem. Phys.*, **141**, 184703 (2014).

[72] A. Malijevsky. *J. Phys.: Condens. Matter*, **26**, 315002 (2014).

[73] A. Malijevsky and A.O. Parry. *Phys. Rev. Lett.*, **110**, 166101 (2013).

[74] A. Malijevsky and A.O. Parry. *J. Phys.: Condens. Matter*, **25**, 305005 (2013).

[75] A. Malijevsky and A.O. Parry. *Phys. Rev. E*, **91**, 052401 (2015).

[76] U.M.B. Marconi and F. Van Swol. *Phys. Rev. A*, **39**, 4109 (1989).

[77] P. Marmottant and S. Hilgenfeldt. *Proc. Natl. Acad. Sci. USA*, **101**, 19523 (2004).

[78] D.R. Meldrum and M.R. Hall. *Science*, **297**, 1197 (2002).

[79] N. Metropolis, A.W. Rosenbluth, M.N. Rosenbluth, A.N. Teller, and E. Teller. *J. Chem. Phys.*, **21**, 1087 (1953).

[80] A. Milchev, M Müller, K. Binder, and D.P. Landau. *Phys. Rev. Lett.*, **90**, 136101 (2003).

[81] A. Milchev, M Müller, K. Binder, and D.P. Landau. *Phys. Rev. E*, **68**, 031601 (2003).

[82] H. Nakanishi and M.E. Fisher. *Phys. Rev. Lett.*, **49**, 1565 (1982).

[83] H. Nakanishi and M.E. Fisher. *J. Chem. Phys.*, **78**, 3279 (1983).

[84] R. Pandit and M. Wortis. *Phys. Rev. B*, **25**, 3226 (1982).

[85] R. Pandit, M. Schick and M. Wortis. *Phys. Rev. B*, **26**, 5112 (1982).

[86] A.O. Parry, R. Evans, and K. Binder. *Phys. Rev. B*, **43**, 11535 (1991).

[87] A.O. Parry, M.J. Greenall and J.M. Romero-Enrique. *Phys. Rev. Lett.* **90** 046101 (2003).

[88] A.O. Parry, M.J. Greenall, and A.J. Wood. *J. Phys.: Condens. Matter*, **14**, 1169 (2002).

[89] A.O. Parry, A. Malijevsky and C. Rascon. *Phys. Rev. Lett.*, **113**, 146101 (2014).

[90] A.O. Parry, and C. Rascón. *J. Phys.: Condens. Matter*, **23**, 015004 (2011).

[91] A.O. Parry, C. Rascón, N.R. Bernardino and J.M. Romero-Enrique. *J. Phys.: Condens. Matter*, **18**, 6433 (2006).

[92] A.O. Parry, C. Rascón, N.R. Bernardino and J.M. Romero-Enrique. *J. Phys.: Condens. Matter*, **19**, 416105 (2007).

[93] A.O. Parry, C. Rascón, N.R. Bernardino and J.M. Romero-Enrique. *Phys. Rev. Lett.*, **100**, 136105 (2008).

[94] A.O. Parry, C. Rascón, N.R. Bernardino and J.M. Romero-Enrique. *J. Phys.: Condens. Matter*, **20**, 494234 (2008).

[95] A.O. Parry, C. Rascón, N.B. Wilding and R. Evans. *Phys. Rev. Lett.*, **98**, 226101 (2007).

[96] A.O. Parry, C. Rascón and A.J. Wood. *Phys. Rev. Lett.*, **83**, 5535 (1999).

[97] A.O. Parry, C. Rascón and A.J. Wood. *Phys. Rev. Lett.*, **85**, 345 (2000).

[98] A.O. Parry, J.M. Romero-Enrique, N.R. Bernardino and C. Rascón. *J. Phys.: Condens. Matter*, **20**, 505102 (2008).

[99] A.O. Parry, J.M. Romero-Enrique and A. Lazarides. *Phys. Rev. Lett.*, **93**, 086104 (2004).

[100] A.O. Parry, A.J. Wood, and C. Rascón. *J. Phys.: Condens. Matter*, **12**, 7671 (2000).

[101] A.O. Parry, A.J. Wood, and C. Rascón. *J. Phys.: Condens. Matter*, **13**, 4591 (2001).

[102] P. Patrício, C.T. Pham and J.M. Romero-Enrique. *Eur. Phys. J. E*, **26**, 97 (2008).

[103] P. Patrício, J.M. Romero-Enrique, N.M. Silvestre, N.R. Bernardino and M.M. Telo da Gama. *Mol. Phys.*, **109**, 1067 (2011).

[104] P. Patrício, N.M. Silvestre, C.T. Pham and J.M. Romero-Enrique. *Phys. Rev. E*, **84**, 021701 (2011).

[105] P. Patrício, M. Tasinkevych and M.M. Telo da Gama. *Eur. Phys. J. E*, **7**, 117 (2002).

[106] J.M. Perkel. *Science*, **322**, 975 (2008).

[107] Y. Pomeau. *J. Colloid Interface Sci.*, **113**, 5 (1985).

[108] C. Pozrikidis, *A practical guide to boundary element methods with the software library BEMLIB*, (Chapman & Hall, Boca Raton, 2002)

[109] W.H. Press, S.A. Teukolsky, W.T. Vetterling and B.P. Flannery. *Numerical Recipes: The Art of Scientific Computing, in Fortran*, Second Ed. (Cambridge University Press, Cambridge, 1992).

[110] *Finite Size Scaling and Numerical Simulation of Statistical Systems*, ed. V. Privman (World Scientific, Singapore, 1990).

[111] D. Quéré. *Annu. Rev. Mater. Sci.*, **38**, 71 (2008).

[112] C. Rascón and A.O. Parry. *Nature*, **407** 986 (2000).

[113] C. Rascón and A.O. Parry. *J. Chem. Phys.*, **112**, 5175 (2000).

[114] C. Rascón and A.O. Parry. *J. Phys: Condens. Matter*, **12**, A369 (2000).

[115] C. Rascón and A.O. Parry. *Phys. Rev. Lett.*, **94**, 096103 (2005).

[116] C. Rascón, A.O. Parry , R. Nürnberg, A. Pozzato, M. Tormen, L. Bruschi and G. Mistura. *J. Phys: Condens. Matter*, **25**, 192101 (2013).

[117] C. Rascón, A.O. Parry and A. Sartori. *Phys. Rev. E*, **59**, 5697 (1999).

[118] K. Rejmer. *Physica A*, **373**, 58 (2007).

[119] K. Rejmer, S. Dietrich, and M. Napiorkowski, *Phys. Rev. E*, **60**, 4027 (1999).

[120] K. Rejmer and M. Napiorkowski, *Phys. Rev. E*, **62**, 588 (2000).

[121] A. Rodríguez-Rivas, J. Galván, and J.M. Romero-Enrique, *J. Phys.: Condens. Matter*, **27**, 035101 (2015).

[122] A. Rodriguez-Rivas, J.M. Romero-Enrique, and L.F. Rull, *unpublished.*

[123] A. Rodriguez-Rivas, J.M. Romero-Enrique, L.F. Rull and A. Milchev, *Europhys. Lett.*, **108**, 26003 (2014).

[124] C.M. Rogers. *Biofabrication.*, **6**, 035003 (2014).

[125] J.M. Romero-Enrique, and A.O. Parry. *Europhys. Lett.*, **72**, 1004 (2005).

[126] J.M. Romero-Enrique, and A.O. Parry. *J. Phys.: Condens. Matter*, **17**, S3487 (2005).

[127] J.M. Romero-Enrique, and A.O. Parry. *New J. Phys.*, **9**, 167 (2007).

[128] J.M. Romero-Enrique, A.O. Parry and M.J. Greenall. *Physical Review E*, **69**, 061604 (2004).

[129] J.M. Romero-Enrique, C.T. Pham and P Patrício. *Phys. Rev. E*, **82**, 011707 (2010).

[130] J.M. Romero-Enrique, A. Rodriguez-Rivas, L.F. Rull and A.O. Parry. *Soft Matter*, **9**, 7069 (2013).

[131] R. Roth and A.O. Parry. *Mol. Phys.*, **109**, 1159 (2011).

[132] L.F. Rull, and J.M. Romero-Enrique. *unpublished* (2012).

[133] E.K. sackmann, A.L. Fulton and D.J. Beebe. *Nature*, **507**, 181 (2014).

[134] M. Schick. *Liquids and Interfaces* ed J Chorvolin, J F Joanny and J Zinn-Justin (New York: Elsevier) (1990).

[135] R.F. Service. *Science*, **282**, 400 (1998).

[136] N.M. Silvestre, Z. Eskandari, P. Patrício, J.M. Romero-Enrique and M.M. Telo da Gama. *Phys. Rev. E*, **86**, 011703 (2012).

[137] D.E. Sullivan and M.M. Telo da Gama. *Fluid Interfacial Phenomena*, ed C A Croxton (New York: Wiley) (1986).

[138] Z. Suo and W. Hong. *Proc. Natl. Acad. Sci. USA*, **101**, 7874 (2004).

[139] M. Svodoba, A. Malijevsky and M. Lisal. *J. Chem. Phys.*, **143**, 104701 (2015).

[140] P.S. Swain and A.O.Parry, *Eur. Phys. J. B*, **4**, 459 (1998).

[141] M. Tasinkevych and S. Dietrich. *Phys. Rev. Lett.*, **97**, 106102 (2006).

[142] M. Tasinkevych and S. Dietrich.*Eur. Phys. J. E*, **23**, 117 (2007).

[143] A. Terry *et al.* *Science*, **296**, 1841 (2002).

[144] J. Thomsen, G.T. Einevoll, and P.C. hemmer. *Phys. Rev. B*, **39**, 12788 (1989).

[145] M. Utz and J. Landers. *Science*, **330**, 1056 (2010).

[146] R.N. Wenzel. *Ind. Eng. Chem.*, **28**, 988 (1936).

[147] R.N. Wenzel. *J. Phys. Chem.*, **53**, 1466 (1949).

[148] G.M. Whitesides. *Nature*, **442**, 368 (2006).

[149] G.M. Whitesides and A.D. Stroock. *Phys. Today*, **54**, 42 (2001).

[150] L.J. Xue and Y.C. Han. *Prog. Polym. Sci*, **36**, 269 (2011).

[151] P. Yatsyshin, N. Savva and S. Kalliadasis. *Phys. Rev. E*, **87**, 020402(R) (2013).

[152] T. Young. *Philos. Trans. R. Soc. London*, **95**, 65 (1805).

[153] O. C. Zienkiewicz and T. L. Taylor, *El método de los elementos finitos*, 4th ed. (McGraw-Hill. Madrid, 1994).